Beryllium mono-hydride: electron collision and spectroscopic modelling for fusion plasmas

Daniel Malcolm Darby-Lewis

A dissertation submitted in partial fulfillment

of the requirements for the degree of

Doctor of Philosophy

of

University College London.

Department of Physics and Astronomy

University College London

August 20, 2019

I, Daniel Malcolm Darby-Lewis, confirm that the work presented in this thesis is my own. Where information has been derived from other sources, I confirm that this has been indicated in the work.

List of Publications

R-Matrix Calculations of electron-impact electronic excitation of BeH.

D Darby-Lewis, Z. Masin, and J. Tennyson. *J. Phys. B: At. Mol. Opt. Phys.*, 50:175201, 2017.

Results presented in section 3.1.1.

Synthetic spectra of BeH, BeD and BeT for emission modelling in JET plasmas.

D Darby-Lewis, J. Tennyson, K. D. Lawson, S. N. Yurchenko, M. F. Stamp, A. Shaw, S. Brezinsek, and JET Contributor. *J. Phys. B: At. Mol. Opt. Phys.*, 51:185701, 2018.

Results presented in section 3.3.

Electron-He_2^+ scattering calculation using the R-matrix method: resonant and bound states of He_2.

M. D. Epée Epée, O. Motapon, **D Darby-Lewis**, and J. Tennyson. *J. Phys. B: At. Mol. Opt. Phys.*, 50:115203, 2017.

MARVEL analysis of the measured high-resolution spectra of ^{14}NH.

Daniel Darby-Lewis, Het Shah, Dhyeya Joshi, Fahd Khan, Miles Kauwo, Nikhil Sethi, Peter F. Bernath, Tibor Furtenbacher, Roland Tóbiásd, Attila G. Császárd, Jonathan Tennyson. *Journal of Molecular Spectroscopy* 10.1016/j.jms.2019.06.002, 2019.

Abstract

This thesis presents high level theoretical data for beryllium mono-hydride, including electron collisional data and a theoretical spectral model for the isotopologues BeH, BeD and BeT in the visible and infrared. The R-matrix method is used to perform high-level calculations of electron collisions with beryllium mono-hydride at its equilibrium geometry with a particular emphasis on electron impact electronic excitation. The calculations were performed using (1) the UKRMol suite which relies on the use of Gaussian type orbitals (GTOs) to represent the continuum and (2) using the new UKRMol+ suite which allows the inclusion of B-spline type orbitals in the basis for the continuum. The final close-coupling scattering models used the UKRMol+ code and a frozen core, valence full configuration interaction, method based on a diffuse GTO atomic basis set. These calculation are also reproduced over a range of internuclear separation to produce geometry dependent scattering quantities. A theoretical model for the isotopologues of beryllium monohydride, BeH, BeD and BeT, A $^2\Pi$ to X $^2\Sigma^+$ visible and X $^2\Sigma^+$ to X $^2\Sigma^+$ infrared rovibronic spectra is also produced. From transition energies and Einstein coefficients, accurate assigned synthetic spectra for BeH and its isotopologues are obtained at given rotational and vibrational temperatures. The BeH spectrum is compared with a high resolution hollow-cathode lamp spectrum and the BeD spectrum with high resolution spectra from JET giving effective vibrational and rotational temperatures. Both the R-matrix and spectral modelling results are combined to produce vibrationally averaged electron scattering results.

Impact Statement

This work has produced data relevant in both fusion plasma and astrophysical areas of research and especially for the JET and ITER projects. JET, the Joint European Torus, part funded this project as they have recently undergone an upgrade in which the reactor inner wall was converted from carbon to beryllium. This inner wall can interact with the plasma edge and molecules can be formed. With the beryllium wall and a hydrogen (deuterium and tritium) plasma some of the most abundant such molecules are beryllium hydrides. This work is there for investigating BeH, specifically the interaction between electrons and BeH and the emission spectrum of BeH. Within the field of astrophysics BeH has been observed in the interstellar medium and the spectral model produced by this work can be used by researchers in astronomy.

Acknowledgements

I am immensely grateful to both of my supervisors, Prof. Jonathan Tennyson and Dr. Kerry Lawson without whom I would never have had this opportunity. As supervisors they have been foundations of support through out this entire experience. I have a deep respect for the effort they have put into me and my work and the guidance they have provided.

I was welcomed by Jonathan's group at UCL and aided by virtually every member at some point. Special thanks go to Laura McKemmish without whom my early experience would have been unrecognisable. Kerry's spectroscopy group welcomed me while I was at JET and I truly appreciate the perspective I gained working so closely with an experimentally focused group.

I would like to thank every co-author I have had, especially Zdenek Mašín for his help in setting up BeH UKRMol+ calculations, Sergey Yurchenko for his repeated aid in many things, and Sebastijan Brezinsek for providing an original experimental BeH spectrum. Thanks also to those at ADAS who provided me with the first presentation opportunity I had to talk externally about this work, especially Martin O'Mullane.

Thanks to the Engineering and Physical Sciences Research Council (EPSRC) for studentship (EP/M507970/1) and the Culham Centre for Fusion Energy (CCFE) for funding. This work was carried out within the framework of the EUROfusion Consortium and has received funding from the Euratom research and training programme 2014-2018 under grant agreement No. 633053 and from the RCUK Energy Programme [Grant number EP/P012450/1]. The views and opinions expressed herein do not necessarily reflect those of the European Commission.

Thanks to my family, my parents who always supported my interest in science, my siblings who will, from now on, always call me Dr, and most of all my wife who started this journey with me and has been totally irreplaceable through eight years of university. Without her support and encouragement in everything over the past eight years I would never have made it to where I am now. Finally, thanks to God for the opportunity and ability to achieve this work, all honour and glory to Him.

Contents

List of Figures

List of Tables

Acronyms

ADAS Atomic Data and Analysis Structure. 31

BOB Born-Oppenheimer breakdown. 30, 45, 68, 69, 101, 102, 117

BTO B-spline type orbital. 28, 53–55, 78, 79

CAS complete active space. 40, 41, 52

CAS-CI complete active space configuration interaction. 40, 41, 51, 73, 75, 77, 78, 81, 82

CC close coupling. 51, 52

CI configuration interaction. 43, 56–58

CSF configuration state function. 40, 41, 56, 57

EMO extended Morse oscillator. 43

FC-FCI frozen core full configuration interaction. 41, 51, 52, 73–76, 78, 81, 82, 85

FCF Franck-Condon factor. 27, 29, 59–61, 90–94, 117, 119

FCI full configuration interaction. 41, 52, 73–75

GS ground state. 39, 40, 43, 73, 86, 88, 92, 100, 119

GTO Gaussian type orbital. 28, 35, 36, 53–55, 76–78

HF Hartree-Fock. 39–41, 51, 77

ILW ITER-like wall. 23

LOS line of sight. 32, 106

LTE local thermal equilibrium. 31, 70, 103, 107–109

MLR Morse long-range. 43, 44

MO molecular orbital. 36, 37, 40, 41

PEC potential energy curve. 27, 30, 43–45, 63, 67–69, 87, 88, 92, 100–102, 117

PFC plasma facing components. 23–25

SCF self consistent field. 39

SE static exchange. 51

SOL scrape-off layer. 24, 25

Glossary

DEMO DEMOnstration Power Station, intended to be built upon completion of ITER. 23

Duo A nuclear motion code for diatomic molecules, capable of producing empirically refined potential energy curves with various couplings. 18, 30, 33, 59, 62, 67, 68, 70, 95, 101, 103, 105

ExoCross A code for producing molecular spectra in various conditions from transition and state information provided by Duo. 67–70, 107

ITER International thermonuclear experimental reactor, nuclear fusion research and engineering megaproject, founded 2007, expected completion date 2025. 23, 24, 72

JET Joint European torus, currently the worlds largest nuclear fusion reactor and research vessel. 23–25, 31, 32, 67, 72, 106, 108, 109, 118–120

MARVEL Measured active vibrational rotational energy levels, a code which takes assigned molecular transitions with uncertainties and calculated spectroscopic networks of energy levels. 17, 18, 67–69, 98, 99, 101, 103, 114, 115

MolPro A quantum chemistry code, used in this project to perform Hartree Fock calculations and produce molden input files. 33, 56, 87

UKRMol An suite of codes for performing R-matrix calculation of electron collision and scattering off of molecular targets, uses a Gaussian type orbital

representation of the continuum. 12, 27, 28, 32, 33, 53, 55–57, 61, 72, 76, 78, 86, 114, 119

UKRMol+ A new suite of codes, to replace UKRMol, for performing R-matrix calculation of electron collision and scattering off of molecular targets using a mixed Gaussian type orbital and b-spline type orbital representation of the continuum. 13, 17, 28, 29, 32, 33, 53, 55, 57, 72, 78, 80–83, 85, 86, 116, 117, 119

Chapter 1

Introduction

1.1 Data For Nuclear Fusion

Achieving controlled and sustained nuclear fusion on Earth has been a key goal of multi-disciplinary physics for almost half a century (Winter 1975, Lister 2006, Keilhacker et al. 2001). One of the most promising routes towards its practical implementation is using a tokamak, a low density torus-shape plasma reactor, such as joint European torus (JET) (Schumacher 1983, Gibson 1979). JET is conducting vital research for the next generation of tokamaks, the international thermonuclear experimental reactor (ITER) and DEMOnstration Power Station (DEMO). Specifically the structure of JET is currently supporting an internal reactor wall called the ITER-like wall (ILW) (Brezinsek et al. 2015). This is a wall with beryllium on various plasma facing components (PFC) as proposed for use in ITER (Kupriyanov et al. 2015). A proto-type of the wall that is proposed for use on ITER is currently in use on JET as a test to ensure its viability at a larger scale and to bring to attention any issues with a beryllium wall. This work is producing data specifically aimed at testing the viability and to aid in flagging some such issues. A diagram of the interior of the JET reactor vessel is show in figure 1.1. From this image it can be seen that a substantial surface of the plasma facing components (PFC) are either beryllium or beryllium coated.

In order to predict the erosion, migration and re–deposition of the Be first wall in fusion devices such as JET, and in the future ITER, and in view of impurity pro-

duction and lifetime of components, an understanding of the release and transport of Be is an essential requirement. BeT is also important for modelling tritium retention in beryllium containing fusion devices. The transport of BeH, BeD (and eventually BeT) in the JET scrape-off layer (SOL) is important for tracking what happens to the tritium in the reactor, both for the future of JET and for ITER (Doerner et al. 2007). BeD_X release was shown to contribute more than 50% to the total erosion in certain cases in JET D plasmas in a limiter configuration deduced from BeD emission spectra (Brezinsek et al. 2014).

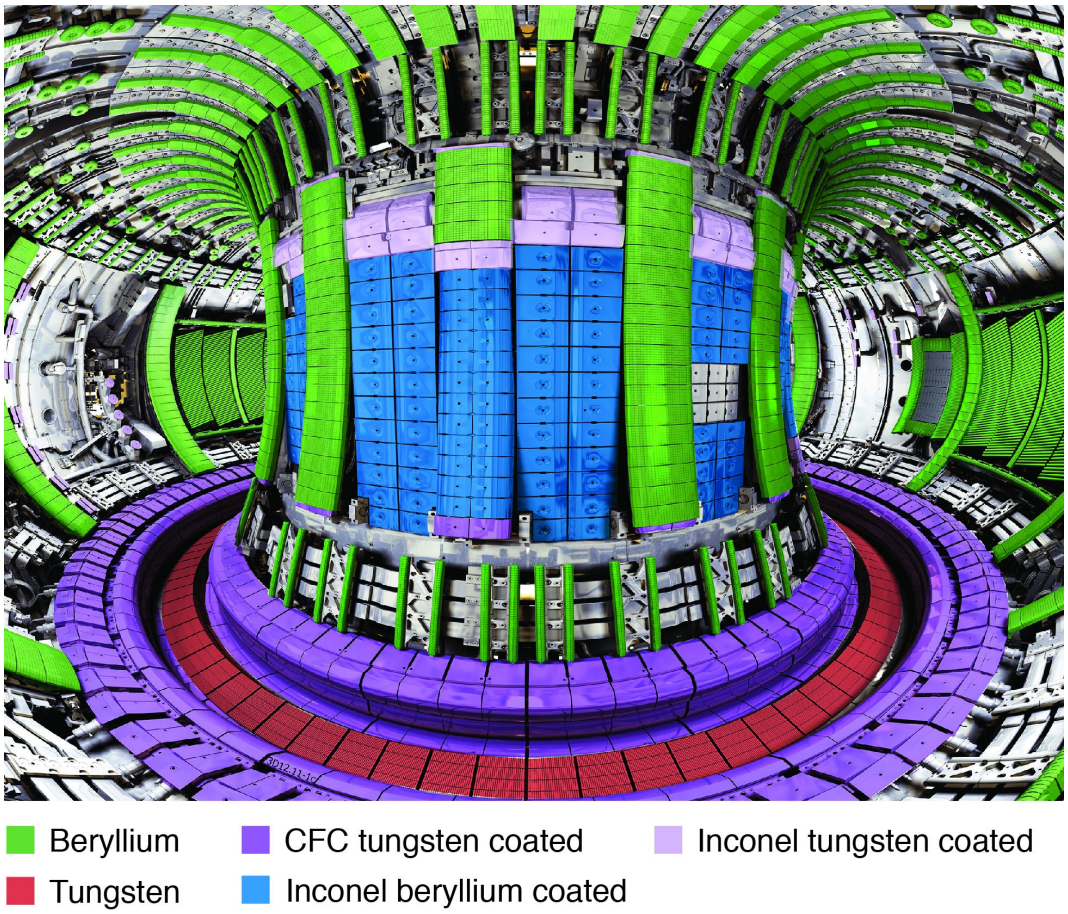

Figure 1.1: Image of the interior of JET showing the various compositions of plasma facing components. The large portion of beryllium and beryllium coated plasma facing components can be seen in green and blue. Image taken from https://www.iter.org/newsline/-/3172.

The scrape-off layer (SOL) is the plasma layer closest to the PFCs. The plasma here can interact with the reactor wall and therefore contains molecules which are formed at the wall (Federici 2006). With the addition of beryllium to the PFCs

one molecule known to be formed is BeH as well as the isotopologues containing hydrogen isotope variations of deuterium (D) and tritium (T). BeH_2 is suspected to also be formed.

Figure 1.2 shows a temperature scale plot of a slice through one segment of the JET vessel with magnetic field lines. The core temperature of the JET plasma can reach in excess of 5 KeV (58,000,000 K), which for reference is almost four times the temperature of the core of the sun which is at about 1.2 KeV (15,000,000 K). Within the $\approx$ 1 m interior radius of the vessel the temperature drops below 1 eV (<12,000 K) at the PFCs to around 700 eV (8,000,000 K) at the scrape-off layer (SOL) with the bulk of the plasma retaining a temperature of about 4 KeV (46,000,000 K). As can be seen in the diagram the temperature trends to remain constant with the magnetic field lines. There is a very steep drop off in temperature near the edge of the plasma called the pedestal region, only a few cm across, which helps maintain a very hot plasma bulk and cool edge region. It is only within the SOL that the plasma is cool enough to allow for the formation of molecules.

In a plasma, with its large density of free electrons, processes involving electron collisions with BeH play an important role in detecting and tracking the movement and deposition of BeH around the reactor (Bessenrodt-Weberpals et al. 1987). In particular a useful diagnostic is the radiative emission coming from the A $^2\Pi \rightarrow$ X $^2\Sigma^+$ transition in BeD (Duxbury et al. 1998, Doerner et al. 2009, Nishijima et al. 2008), where the initial excitation of BeD to the A-state is largely thought to originate in inelastic collisions of electrons with the molecule. There is therefore a need for accurate data on electron impact electronic excitation for applications to fusion (Samm 2005). Detailed studies of molecular spectra (Duxbury et al. 1998), such as those for BeH, BeD, and BeT A – X bands can provide valuable input to codes used for erosion modelling such as ERO (Borodin et al. 2011, Lasa et al. 2017). These applications at present generally require data for BeD and will need BeT data in future.

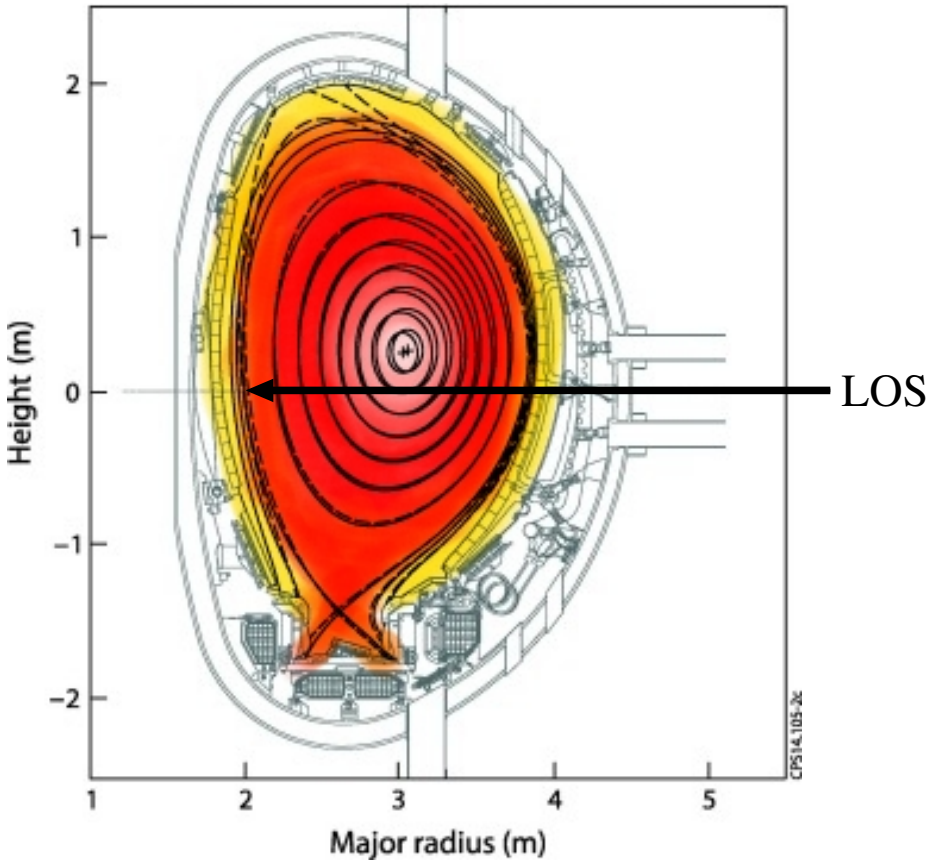

Figure 1.2: Diagram representing temperature ranges and magnetic field lines in the JET reactor during the peak of a pulse. White at the core ≈ 5 KeV, red for plasma bulk ≈ 4 KeV, orange pedestal ≈ 700 eV, to scrape of layer in yellow ≈ 300 eV.

1.2 R-Matrix

One large portion of this work is electron scattering calculations and the data is generated using the R-matrix method. This method divides the problem into an inner region and an outer region, as show in figure 1.3. The inner region is contained by a sphere of radius a_0, the R-matrix radius, centred on the centre of mass of the molecule. This region contains the target wavefunctions and in this portion of the calculation all the complex quantum chemistry is calculated. The outer region is where the R-matrix is formed at the boundary between the two regions and extrapolated to a distance at which the scattering wavefunctions are asymptotic.

There have been a number of recent studies on electron collisions with BeH^+ (Roos et al. 2009, Chakrabarti and Tennyson 2012, Celiberto et al. 2012b,

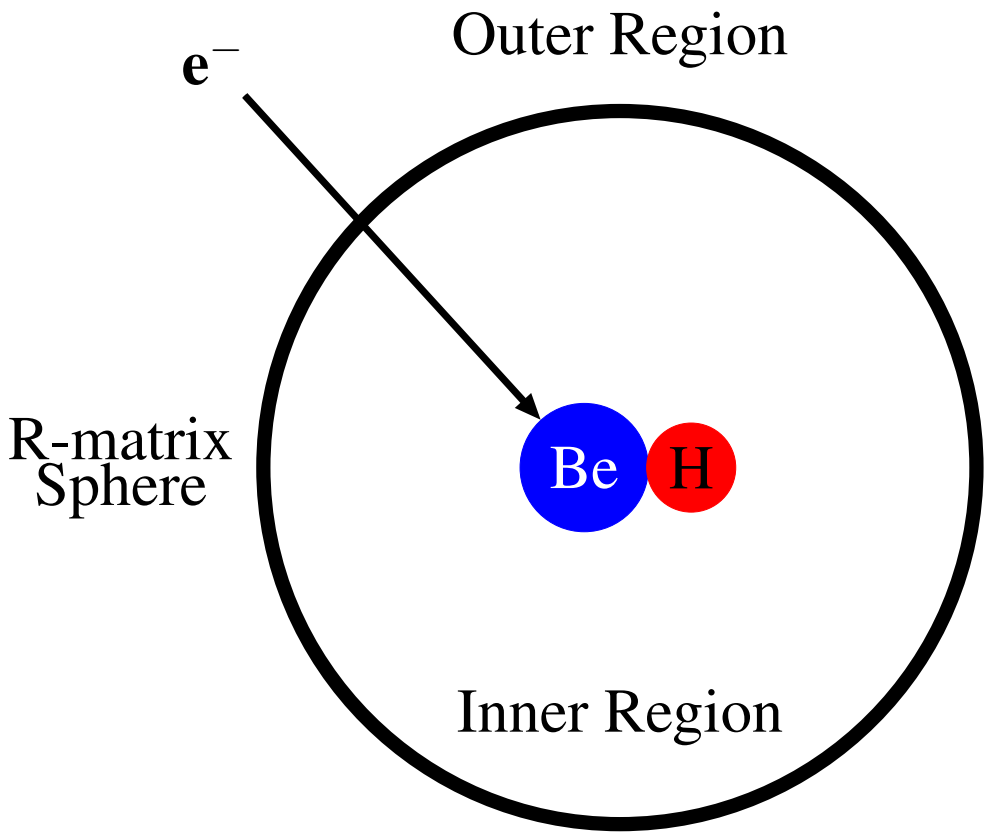

Figure 1.3: Diagram showing the division of the inner and outer regions in an R-matrix calculation, a sphere of radius a_0 dividing the inner region with its complex quantum chemistry from the outer region in which a simpler analysis is possible.

Chakrabarti and Tennyson 2015, Niyonzima et al. 2017, Laporta et al. 2017), but we are only aware of a single other study of electron collisional excitation of neutral BeH. This was a recent R-matrix calculation by Celiberto et al. (2012a). In their calculations Celiberto et al. (2012a) computed vibrationally-resolved results for electron impact electronic excitation of the molecule by combining cross sections computed using the UKRMol codes (Carr et al. 2012) with a Franck-Condon factor (FCF) method. These results considered only the lowest-lying electronically-excited state of BeH, the A $^2\Pi$ state, used a frozen core configuration interaction (FC-CI) model for the target wavefunction, a small, double zeta plus polarisation (DZP) basis set and *ab initio* potential energy curve (PEC)s from Pitarch-Ruiz et al. (2008).

The work presented in this thesis aims to improve upon the work of Celiberto

et al. (2012a) by considering many excited states, modelled using a larger basis set with diffuse orbitals, and critically by including the Born correction for the dipole at high partial waves. The inclusion of the diffuse basis functions is important for an accurate description of the electronic spectrum of the molecule and of the scattering observables.

The inclusion of diffuse electronic states presents a number of technical difficulties for R-matrix scattering calculations using the UKRMol suite which we aim to overcome here. The UKRMol suite (Carr et al. 2012) is a well-established set of programs for calculations of electron – molecule scattering and other processes using the R-matrix method (Tennyson 2010). The codes use Gaussian Type Orbitals (GTOs) to represent both the target and the continuum wavefunction in the region of the molecular target (Faure et al. 2002) and employ a methodology applicable to the treatment of electronically inelastic processes (Tennyson 1996).

In practice diffuse atomic functions cannot be included in most calculations using the UKRMol suite due to numerical problems which arise when a large Gaussian type orbital (GTO)-only continuum basis is combined with a large R-matrix sphere that must be used to contain the spatially extended electronic states of the target molecule (Mašín and Gorfinkiel 2011). However, this limitation has been recently overcome thanks to the newly-developed UKRMol+ suite (Zdenek Mašín 2017), which allows the inclusion of B-spline type orbital (BTO) basis functions to represent the continuum. As we demonstrate below UKRMol+ can be used with much larger R-matrix spheres than UKRMol while maintaining numerical stability and quality of the continuum description.

Finally, BeH is an important molecule for testing *ab initio* methods, being the smallest, neutral open shell molecule. Having only five electrons makes the use of highly sophisticated methods with large basis sets computationally possible. Therefore much work has been done on BeH using different quantum chemical methodologies over more than 86 years (reviewed by Dattani (2015)). There is also a recent study on morphing BeH potentials (Špirko 2016) which came out after that review.

Before now similar levels of consideration have not been applied to electron collision calculations with BeH. That is something addressed in this work, where we find that BeH provides a good benchmark system for such studies too. This is born out by its use in the first intensive testing of the new UKRMol+ suite of codes. There is a study by Celiberto et al. (2012b) which also includes a treatment of BeH vibronically resolved electron collision cross-sections; this particular work is further discussed below. There have been several electron collision studies with BeH^+ (Chakrabarti and Tennyson 2012, 2015, Niyonzima et al. 2017, Laporta et al. 2017, Niyonzima et al. 2018) some of which include a study of the resonant states of that cation. There has even been a recent paper on the study of BeH_2 electron collisions using the R-matrix method (Gupta et al. 2019), also for application to fusion plasma data. This work takes a step to achieving the same high quality of treatment of the neutral that has been applied to the cation so far.

1.2.1 Vibrational Resolution

In order to produce useful rate equations we need to be able to resolve the vibrational transition rates not just the electronic transition rates which come from the R-matrix calculations. There are two methods for consideration here, firstly the application of FCFs to the equilibrium geometry results and secondly a vibrational averaging of multi-geometry R-matrix calculations. The first approach, using FCFs, has the advantage of being usable with only a single geometry R-matrix calculation and is easy to program as a simple weighted separation of the electronic cross-section into vibrational parts. The drawbacks to this method are that it produces vibrational resolution only between different electronic states as within a given state the functions are orthogonal and only $v'' = v'$ is non-zero, is a more approximate approach and it makes additional, further restrictive, assumptions. This approach will not allow a full radiative collisional model to be constructed as there are no rates for relaxation within a state. The second approach uses multi-geometry R-matrix calculations to provide T-matrices (scattering results) as functions of internuclear separation which are convoluted with vibrational functions to give vibrational resolution. This approach has the advantage of being able to provide transition data for

every vibrational transition including those from within the same electronic state as the orthogonality of the vibrational wavefunctions is relaxed by their convolution with the geometry dependent scattering quantities. Another advantage to this method is that it includes the changes in scattering features that occur with geometry. The drawback to this method is that it requires many computationally expensive R-matrix calculations for many geometries.

1.3 Spectral Modelling

As a major part of this project we develop a full spectroscopic model for BeH, BeD and BeT X $^2\Sigma^+$ and A $^2\Pi$ states based on explicit PEC, spin-orbit (*LS*) and Λ doubling (L^+) couplings, Born-Oppenheimer breakdown (BOB) terms, and *ab initio* dipole curves. The PECs, couplings, and BOB terms are derived using accurate experimentally recorded transition frequencies. Previous PEC fittings for the X state by Le Roy et al. (2006) and Koput (2011) have been improved upon by Dattani (2015), and further refined in this work by fitting procedures involving the X-A state transitions. The A state PEC was previously studied by Le Roy et al. (2006) and is also improved upon here. The fitting in Duo (Yurchenko et al. 2018) results in a full set of accurate transitions for BeH, BeD, and BeT from a single set of PECs, couplings, and BOB terms (Le Roy 2017). These data are used to determine temperatures in the experimental spectra. This method of using variational nuclear motion calculations with BOB terms to link isotopologue data differs from the methods based on perturbation theory generally employed up until now, see Duxbury et al. (1998) and Hornkohl et al. (1991). These older methods use spectroscopic constants to calculate energies but cannot join isotopologue data and thus do not provide predictions for yet–to–be observed isotopologues. They also extrapolate to high J (rotational quantum number) or high v (vibrational quantum number) inaccurately. Our approach is similar in spirit to that adopted by Parigger et al. (2015) to model laser ablation and by McGuire et al. (2016) to model plasma ablation.

Our linelists for BeH, BeD and BeT improve on those of Yadin et al. (2012)

produced as part of the ExoMol project (Tennyson and Yurchenko 2012) both in having greater range and improved accuracy in the transition frequencies. This thesis aims to give a more accurate fit to the spectrum of the BeD A – X transition than was achieved by Duxbury et al. (1998) and Björkas et al. (2013) by using more accurate transition data and allowing separate treatment of vibrational and rotational temperatures. The use of different rotational and vibrational temperatures, which implies there is no local thermodynamic equilibrium (non– local thermal equilibrium (LTE)), is expected to lead to a more accurate description of the experimental spectrum.

We compare theoretically produced synthesised spectra to new experimental BeD spectra recorded on JET and BeH spectra recorded in Be hollow cathode discharges in Forschungszentrum Jülich. Both of these spectra were recorded employing spectrometers with high spectral resolution in the visible range, sufficient to resolve the rotational lines.

1.4 Data and Code Storage and Availability

In this project we have the preservation of both intensive data from calculations and original developed code to consider.

The first of these concerns has been partially addressed by supplementary information in the second of the major publications from this work (Darby-Lewis et al. 2018). This contains all the data for the spectroscopic model and is freely available online. The more difficult aspect is the storage and sharing of the BeH electron scattering R-matrix data, especially the large quantity of data from the multi–geometry and vibronic resolution calculations. One consideration for the storage of these electron–molecule scattering data was the Atomic Data and Analysis Structure (ADAS) database (Summers and O'Mullane 2011). We engaged in discussions on how to include molecular data in the ADAS format. For the meantime data will be stored on UCLsystems where it is available on request and it is also being incorporated on a new IAEA database.

The second of these two concerns is more easily addressed as the majority of

the code is written to be run as an extension to the calculations from the UKRMol /UKRMol+ suites and as such the major portion of original code development will be in the existing repositories for these codes, available on GitLab, https://gitlab.com/Uk-amor.

1.5 Experimental Work at JET

During this project frequent visits were made to Culham Science Centre where JET is located, and I was in placement there for several months. Some of this time overlapped with the period of a deuterium campaign at JET and the group I was placed in, the spectroscopy group, applied for experimental time for pulses allowing us to take spectra we were interested in. Initially an overview spectra was taken to find the position of the BeD A – X state emission, see section 3.4.2. Then I set up the stepping of the whole spectral range with a high resolution spectrometer in consecutive pulses with similar conditions. The stepping was necessary as the range of the high resolution spectrometer was approximately one quarter the range of the whole emission region of interest. This stepping was carried out with spectrometers line of sight (LOS) looking at both limiter and divertor tiles. We found the limiter LOS gave much clearer molecular spectra.

In addition to the collection of BeD A – X emission spectra, see section 3.4.2, I also considered the possibility of BeD_2 observation. We concluded that observations in the infrared would not be possible due interference and overwhelming noise. Thus we considered observations in the near UV as emission from the first electronic excited state. We found a suitable port that views a Be poloidal limiter on the JET inner wall along a horizontal midplane line-of-sight. The port window is quartz and spectra are recorded using a UV optimised optical fibre connected to a small survey spectrometer. This spectrometer has now been installed on the JET machine in time for the next experimental campaign.

Chapter 2

Theory

This chapter discusses the theory and methods used in the various parts of this project. It is broken down into sections by the portion of the work.

The three major branches of theory involved in this work are quantum chemistry, nuclear motion and electron scattering. The quantum chemistry is all carried out to a high-level of sophistication using *ab initio* methods and full treatment of the electronic wavefunction. It is carried out mainly by the programs MolPro (Werner et al. 2012) and scatci_integrals, congen, scatci/mpi-scatci (Gillan et al. 1995, Morgan et al. 1998, Al-Refaie and Tennyson 2017, Carr et al. 2012) in combination. The nuclear motion is used in calculating the vibronic spectral model and for obtaining vibrational wavefunctions for use in vibrationally averaging scattering results. These calculations are carried out by the program Duo (Yurchenko et al. 2016) and also with LEVEL (Le Roy 2017). The electron collision data is calculated using the R-matrix method, a theory which divides space into two regions, and has the advantage of producing high scattering energy resolution relatively cheaply. This is calculated using the UKRMol and UKRMol+ suites of codes.

2.1 Molecular Structure

Before calculating scattering quantities we must develop an appropriate target model of the BeH molecule's electronic structure (vibrational and rotational models require nuclear motion). This chapter is taken largely from the book by Szabo and Ostlund (2012). These target models can be computed at several different levels of sophistication, and are all performed under the Born-Oppenheimer approximation (Born and Oppenheimer 1927). The Born-Oppenheimer approximation is that the electron and nuclear motion can be separated (Atkins and Friedman 2011, Hui 1998, Szabo and Ostlund 2012), i.e.

$$\Psi_{\text{total}}(\mathbf{r},\mathbf{R}) = \Psi_{\text{elec}}(\mathbf{r},\mathbf{R}) \times \Psi_{\text{nucl}}(\mathbf{R}), \tag{2.1.1}$$

where Ψ_{total} is the total molecular wavefunction, $\mathbf{r}$ are the combined electron position coordinates, $\mathbf{R}$ are the combined nuclear position coordinates,Ψ_{elec} is the wavefunction of the electrons, Ψ_{nucl} is the wavefunction of the nuclei. Within our framework the validity of this is dependent upon the underlying assumption that electrons move significantly faster than the nuclei such that on the relevant time-scales either the nuclei can be considered stationary (for calculating electronic motion) or the electrons can be positioned averaged to being a cloud of electrical density (for calculating nuclear motion). This validates our adiabatic treatment of the electronic calculation.

The total Hamiltonian for the molecular system is given as

$$\hat{\mathbf{H}}_{\text{total}}(\mathbf{r},\mathbf{R}) = \hat{\mathbf{K}}_{\text{e}}(\mathbf{r}) + \hat{\mathbf{K}}_{\text{n}}(\mathbf{R}) + \hat{\mathbf{V}}_{\text{ee}}(\mathbf{r}) + \hat{\mathbf{V}}_{\text{en}}(\mathbf{r},\mathbf{R}) + \hat{\mathbf{V}}_{\text{nn}}(\mathbf{R}), \tag{2.1.2}$$

where $\hat{\mathbf{H}}_{\text{total}}$ is the total molecular Hamiltonian, $\mathbf{R}$, and $\mathbf{r}$ are as above, $\hat{\mathbf{K}}_{\text{e}}$ is the electron kinetic energy operator, $\hat{\mathbf{K}}_{\text{n}}$ is the nuclear kinetic energy operator, $\hat{\mathbf{V}}_{\text{ee}}$ is the potential due to the electron-electron interaction, $\hat{\mathbf{V}}_{\text{en}}$ is the potential due to the electron-nuclear interaction, $\hat{\mathbf{V}}_{\text{nn}}$ is the potential due to the nuclear-nuclear interaction. The electronic structure calculations are solutions to the time-independent

electronic Schrödinger equation at a given nuclear geometry

$$\begin{aligned} \hat{\mathbf{H}}_{\text{elec}}(\mathbf{r},\mathbf{R}_j)\Psi_{\text{elec}}(\mathbf{r},\mathbf{R}_j) &= E_{\text{elec}}(\mathbf{R}_j)\Psi_{\text{elec}}(\mathbf{r},\mathbf{R}_j) \\ \text{where} \quad \hat{\mathbf{H}}_{\text{elec}}(\mathbf{r},\mathbf{R}_j) &= \hat{\mathbf{K}}_{\text{e}}(\mathbf{r}) + \hat{\mathbf{V}}_{\text{ee}}(\mathbf{r}) + \hat{\mathbf{V}}_{\text{en}}(\mathbf{r},\mathbf{R}_j) + \hat{\mathbf{V}}_{\text{nn}}(\mathbf{R}_j), \end{aligned} \tag{2.1.3}$$

where Ψ_{elec} and $\mathbf{r}$ are as above, $\mathbf{R}_j$ is a specific arrangement of nuclear geometry, $\hat{\mathbf{H}}_{\text{elec}}$ is the electronic Hamiltonian and E_{elec} is the electronic energy. $\hat{\mathbf{K}}_{\text{e}}$, $\hat{\mathbf{V}}_{\text{ee}}$, $\hat{\mathbf{V}}_{\text{en}}$, and $\hat{\mathbf{V}}_{\text{nn}}$ are as defined above in equation 2.1.2. Most quantum chemistry packages also include a potential term $\hat{\mathbf{V}}_{\text{nn}}(\mathbf{R}_j)$ which is the nuclear-nuclear repulsion and is constant at given $\mathbf{R}_j$, i.e. it is not an operator of Ψ_{elec}. The fixing of the nuclear coordinates leads to the common name for this as the clamped nuclei Schrödinger equation. Function variables may be omitted where they have already been defined.

2.1.1 Molecular basis sets: atomic one-electron wavefunctions

All the quantum chemistry models start with a basis set of atomic orbitals for the molecules constituent atoms, in this case hydrogen and beryllium, the atomic orbitals having s,p,d,f symmetries. These atomic orbitals are used to produce molecular orbitals (one electron wavefunctions) which in turn are in certain configurations to generate molecular states. The quality of all the models scale with the quality of the basis set. Gaussian type orbital (GTO) basis sets have a form

$$\chi_j = e^{-\alpha_j r^2}. \tag{2.1.4}$$

Here the atomic orbitals χ_j are represented as Gaussian functions with exponents α_j set by the definition of your basis set. Using such a basis set is an approximation because there are possible forms of the wavefunction which cannot be expressed with a (finite) sum of primitive Gaussian functions. Contracted basis sets may also be used, which are optimised per atom, and are of the form

$$\chi_j = \sum_{\kappa} d_{j\kappa} e^{-\alpha_\kappa r^2}. \tag{2.1.5}$$

Here the atomic orbitals χ_j are are represented as a sum of Gaussian functions (non contracted atomic orbitals) with exponents α_j set by the definition of your basis set as before and coefficients $d_{j\kappa}$ determining the weighting of the summation. As stated above you wish to keep a similar level of accuracy for all atoms you wish to treat with the basis set of choice. The basis sets used in this work are cc-pVXZ and aug-cc-pVXZ sets where X=D,T or Q (representing double, triple or quadruple), these are GTO basis sets which are known to scale very well as you go from D to T to Q which represent increases in the number of basis functions. The 'aug' in the above stands for augmented and it shows that the basis set contains additional basis functions which are more diffuse, i.e. have a smaller α coefficient.

2.1.2 Molecular orbitals: one-electron wavefunctions

Atomic orbitals can form a molecular orbital (MO) via a theory called the linear combination of atomic orbitals, which is given as

$$\phi_i(\mathbf{r}) = \sum_j a_{ij}\chi_j. \tag{2.1.6}$$

Here an electron at position $\mathbf{r}$ is in the molecular orbital $\phi_i(\mathbf{r})$ and the components of the atomic basis set χ_j contribute to this orbital as set by the coefficients a_{ij}. χ_j are some set of basis functions (or pre-optimised basis functions) and the coefficients a_{ij} are varied to produce the desired MO. Molecular orbitals have symmetries dependent on the spherical harmonic which they are combined with, labelled σ, π, or δ. σ orbitals are non degenerate whereas π and δ orbitals are both doubly degenerate i.e. they contain two orbitals each. The maximum number of MOs you can construct is one to one with the number of basis functions whilst retaining linear independence due to the MOs being linear combinations of the basis functions. Therefore the infinite number of energy levels in atoms (or molecules) cannot be 100% accurately represented with any finite basis set.

The true spacial symmetry of these orbitals depends on the point group of the molecule, for a hetero–nuclear diatomic molecule like BeH this is $C_{\infty v}$. This gives spacial symmetries such as σ^+,σ^-,π,δ,ϕ,... and these are the labels given to or-

bitals of molecules which belong to this point group and are an infinite series. The symmetry of electronic states for molecules in this point group are given by the upper case Greek letters and are also an infinite series Σ^+,Σ^-,Π,Δ,Φ.... However to use these computationally it is useful to truncate the symmetry group to one with a finite number of symmetries. Therefore most quantum chemistry packages, including all of those being used in this work, truncate the symmetry group to the highest finite applicable Abelian point group C_{2v} which has the following four orbital symmetries a_1, b_1, b_2, a_2. As electronic state symmetries these are given as A_1, B_1, B_2, A_2. This is clarified in table 2.1 where a conversion is given for a limited number of the $C_{\infty v}$ symmetries referenced in this work.

Table 2.1: Conversion between symmetries of the $C_{\infty v}$ and C_{2v} point groups.

$\mathbf{C}_{\infty v}$	C_{2v}
Σ^+	A_1
Σ^-	A_2
Π	$B_1 + B_2$
Δ	$A_1 + A_2$

These MOs are one electron spatial wavefunctions and in order to properly consider building a multi-electron state we must add a spin (ω) coordinate to the wavefunction. The new spin-orbitals are formed from a product of one of the previous spacial orbitals and a spin wavefunction, either spin up $\alpha(\omega)$ or spin down $\beta(\omega)$, this is shown as

$$\Phi_i(\mathbf{X}) = \phi_i(\mathbf{r})\alpha(\omega) \text{ or } \phi_i(\mathbf{r})\beta(\omega), \tag{2.1.7}$$

where the joined spin-space coordinate is $\mathbf{X} = (\mathbf{r}, \omega)$ and the new spin-orbital Φ is a product of the orbital, ϕ_i, and spin part, α or β. Consequently each spacial σ orbital contains two one-electron spin-orbitals, but the double degeneracy of the spacial π and δ orbitals means that they each contain four one-electron spin-orbitals. The new spin-orbitals retain the spacial symmetry of their spacial part. These new spin-orbitals can now be used to build the multi-electron molecular state wavefunction.

2.1.3 Molecular states: multi-electron wavefunctions

Multi-electron wavefunctions are formed from products of one-electron wavefunctions. The simplest way of making a state with a certain occupation is then to generate what is known as a Hartree product (Szabo and Ostlund 2012) as

$$\psi_{\mathrm{HP}}(\mathbf{X}_1,...\mathbf{X}_n) = \prod_{i=1}^{n} \Phi_i(\mathbf{X}_i). \tag{2.1.8}$$

Significantly, this form of a multi-electron wavefunction does not account for the indistinguishability of the electrons. This means that the wavefunction should be anti-symmetric upon the exchange of electron positions in the product. If an electron at $\mathbf{r}_1$, in orbital ϕ_1, swapped its orbital with an electron $\mathbf{r}_2$, in orbital ϕ_2, then the resultant wavefunction, with $\phi_2(\mathbf{r}_1)$ and $\phi_1(\mathbf{r}_2)$ should be identical to the negative of the previous one as the electrons themselves are indistinguishable fermions which are anti-symmetric upon a swap of coordinates. This is achieved by something called anti-symmetrisation, which is essentially a superposition of all the arrangements of the electrons in all the occupied orbitals with relative phases of either 1 or -1. The anti-symmetrised wavefunction can now be made to include the spin-space orbitals,

$$\psi_{\mathrm{sSD}}(\mathbf{X}_1,...\mathbf{X}_n) = \hat{A}\psi_{\mathrm{HP}}(\mathbf{X}_1,...\mathbf{X}_n) = \hat{A}\left(\prod_{i=1}^{n} \Phi_i(\mathbf{X}_i)\right). \tag{2.1.9}$$

Here the molecular state wavefunction, a single Slater determinant wavefunction ψ_{sSD} is of n electrons and is an anti-symmetrised Hartree product wavefunction, ψ_{HP}, a product of one electron molecular orbitals, with the anti-symmetrisation being handled by an anti-symmetriser operator $\hat{A}$. Being anti-symmetrised ensures that the wavefunction satisfies the Pauli principle that upon exchange of the electron at $\mathbf{X}_1$ and the electron at $\mathbf{X}_2$ the wavefunction changes sign. The effect of the anti-symmetriser is to produce a wavefunction which is a superposition of rearrangements of the electrons and is properly anti-symmetrised upon the exchange of any two electrons. This can be performed and represented using something called a

Slater determinant (Szabo and Ostlund 2012), this is given by

$$\psi_{\text{sSD}}(\mathbf{X}_1,...\mathbf{X}_N) = \frac{1}{\sqrt{N!}} \begin{vmatrix} \Phi_1(\mathbf{X}_1) & \Phi_2(\mathbf{X}_1) & \dots & \Phi_n(\mathbf{X}_1) \\ \Phi_1(\mathbf{X}_2) & \Phi_2(\mathbf{X}_2) & \dots & \Phi_n(\mathbf{X}_2) \\ \vdots & \vdots & \ddots & \vdots \\ \Phi_1(\mathbf{X}_N) & \Phi_2(\mathbf{X}_N) & \dots & \Phi_n(\mathbf{X}_N) \end{vmatrix}. \tag{2.1.10}$$

Here the matrix in the determinant contains all arrangements of the N electrons in all of the occupied orbitals (of which there are also N, occupied orbitals only) with the orbitals changing across the determinant and the electrons changing down. This representation is exactly equivalent to the above in equation (2.1.9), which is why this wavefunction is often known as a single Slater determinant wavefunction, ψ_{sSD}.

2.1.4 The Hartree-Fock Method

The quantum chemistry models tested started with the simplest case, a Hartree-Fock (HF) calculation for the ground state (GS) of BeH. The HF calculation, also known as a self consistent field (SCF) calculation, includes a single Slater determinant meaning that a single configuration of molecular orbitals are considered. This method works by optimising the coefficients, a_{ij}, in the above equation (2.1.6) for a molecular state as given in equation (2.1.9). The coefficients a_{ij} in equation (2.1.6) are taken from some initial guess, an ansatz of the wavefunction ψ_{sSD}, and varied iteratively until the energy of the Slater determinant converges self consistently. This determines a_{ij} and thus the form and energy of the molecular orbitals are set. Only a single molecular state is generated in a HF calculation and its energy obeys the variational principal.

2.1.5 Multi-Slater Determinant Methods

There are several different methods which take advantage of using a sum of multiple Slater determinants with varying occupation of molecular orbitals as shown by

$$\psi_{\text{mSD}}(\mathbf{X}_1,...\mathbf{X}_N) = \sum_{i=1} C_i \psi^i_{\text{sSD}}(\mathbf{X}_1,...\mathbf{X}_N). \tag{2.1.11}$$

Here ψ_{mSD} is the multi–Slater determinant wavefunction and ψ^i_{sSD} are single Slater determinant wavefunctions with coefficients of expansion being C_i. This sum is performed for a given symmetry and the individual single Slater determinants all have the same total symmetry as the multi–Slater determinant. The differences between each ψ^i_{sSD} is in the occupied orbitals; for example, for a two electron system ψ^1_{sSD} might contain orbitals Φ_1 and Φ_2 whereas ψ^2_{sSD} has orbitals Φ_1 and Φ_3. In both ψ^i_{sSD}'s however the Slater determinant still arranges a superposition of the arrangement of each electron in each occupied orbital. Within the multi-Slater construct each of these individual arrangements of occupied orbitals are called a configuration state function (CSF).

These methods mostly start with a HF calculation and then use the orbitals generated as a basis for optimising the superposition of the Slater determinants. This optimisation is, as with the HF calculation above, done to minimise the total energy of the wavefunction. Multi-Slater methods are variational and the absolute energies cannot go below a "true" answer, though the excitation energies, the energies of the excited states relative to the energy of the GS, are not variational.

There are various methods which allow different Slater determinants to make part of the sum. For example the complete active space configuration interaction (CAS-CI) method, which defines an active set of MOs, called a complete active space (CAS), assigns an active number of electrons and then allows all possible configurations of those electrons within that given space. This method scales factorially on both the number of electrons and with the number of orbitals. Ignoring any symmetry restrictions this gives a scaling factor for a complete active space configuration interaction (CAS-CI) method of

$$C_{o,n} = \frac{(o+n)!}{o!n!}, \tag{2.1.12}$$

where $C_{o,n}$ is the scaling factor of the calculation, o are the number of orbitals in the complete active space (CAS) and n is the number of active electrons.

2.1.6 (Frozen Core) Full Configuration Interaction Methods

The most accurate way to represent the molecular states for a given basis set is by doing a full configuration interaction (FCI) calculation. This method starts from a HF calculation, then makes as many molecular orbitals as you have basis functions; it is equivalent to defining a CAS with all MOs and all electrons. The actual formulation of these molecular orbitals however is irrelevant as the full configuration interaction (FCI) method arranges the molecular orbitals into as many state configurations as possible. This means that the a_{ij} coefficients in (2.1.6) are set by the initial HF calculation and then as many Slater determinants as can be generated with coefficients C_i as in (2.1.11) are summed. By principles of linear combination the accuracy of the calculation depends only on the basis set and it gives the best possible answer for a given basis set. As this method is expressible as a CAS with all MOs and all electron it experiences the same scaling as given in equation 2.1.5 making it scale factorially with both with the number of electrons and the number of basis functions.

In order to reduce this scaling there is a method called the frozen core full configuration interaction (FC-FCI), essentially a special case of the CAS-CI. It can be thought of as starting out as a FCI, but then reducing the number of electrons in the CAS by isolating some in the lowest energy orbitals, and thus significantly reducing the computational expense of the calculation while retaining many of the benefits of the FCI method. This method uses HF orbitals for the core electrons and completely fills them in all CSFs formed, forming a CAS from all the remaining MOs and filling it with the valence electrons. In the case of BeH these are the two lowest σ symmetry spin-MOs formed predominately from the 1s orbitals on the Be atom. This means that the reduction takes away two active electrons and two spin-orbitals from the CAS. The validity of doing this can be seen by comparison of the results with a FCI calculation, see table 3.1 and also in considering the substantial energy difference between these two core orbitals and the other MOs of BeH.

Table 2.2: Explanations of the target models.

Target Model	Comments
HF	A single Slater determinant wavefunction. Gives only the GS configuration.
CAS-CI	A multi-Slater determinant wavefunction. Gives excited states, has a certain number of active orbitals and active electrons.
FC-FCI	A multi-Slater determinant wavefunction. Can be described as a special case of the CAS-CI where all electrons and orbitals are active except for selected core orbitals which are fully occupied at all times.
FCI	A multi-Slater determinant wavefunction. Can be described as a special case of the CAS-CI where all electrons and orbitals are active.

2.1.7 Electronic Structure Constraints

Our primary focus in selecting an electronic structure target model is its use in the inner region of an R-matrix calculation. This leads to three major factors to consider in our selection of a electronic target model. (1) Primarily the selected basis set should be able to deliver accurate energy levels (vertical excitation energies) and target properties (e.g. permanent and transition dipole moments) for all molecular states of interest. (2) The basis set should be small enough to be computationally tractable when used, in conjunction with a continuum basis, in a scattering calculation. (3) The target wavefunctions must fit inside the R-matrix sphere as this is the basic assumption of the method. In practice this requirement may be difficult to satisfy because diffuse functions are often necessary to accurately represent certain excited states and diffuse functions require a larger R-matrix sphere. The size of the R-matrix sphere is limited by point (2), as using a larger sphere requires greater computational resources due to the need to include many more continuum functions in the basis. If the target wavefunctions are too spatially extended and "leak out" of the R-matrix sphere then problems, such as spurious resonances, can arise (Gorfinkiel et al. 2002). Furthermore, a large target and continuum basis can also cause issues with numerical linear dependence which can manifest itself in the inner region as unphysical bound states or R-matrix poles. A summary of the different target models used in this work is given in table 2.2.

2.1.8 Potential Energy Curves

The *ab initio* methods described above in section 2.1.1 to 2.1.5 can be used to calculate an adiabatic potential by varying the geometry of the nuclei in the calculation. For a diatomic, such as BeH, this means varying a single variable, the internu-

clear separation, and it produces a potential energy curve (PEC). It is given by $E_{\text{elec}}(\mathbf{R}_j)$ in equation 2.1.3 where multiple calculation results are concatenated to form $\hat{\mathbf{E}}_{\text{elec}}(\mathbf{R})$, which is now an operator with respect to the nuclear wavefunction. *Ab initio* methods which provide a single electronic state produce only a single PEC but multi-state methods, such as configuration interaction (CI), can produce multiple PECs (one per state) i.e. $\hat{\mathbf{E}}^i_{\text{elec}}(\mathbf{R})$ for a given electronic state Ψ^i_{elec}. A PEC is the potential in which the nuclei moves in the Born-Oppenheimer approach to the nuclear motion calculation.

In addition to being derived from *ab inito* calculations PECs can also be given analytical forms. In this work the two electronic states of main interest in BeH are the GS, $X^2\Sigma^+$, and the first excited state, $A^2\Pi$ and they are given the analytical forms of a Morse long-range (MLR) potential (Roy and Henderson 2007) and an extended Morse oscillator (EMO) potential (Lee et al. 1999) respectively.

The form of an EMO potential is represented by

$$V_{\text{EMO}}(r) \equiv \mathscr{D}_e \left[1 - e^{\beta(r)\cdot(r-r_e)}\right]^2, \tag{2.1.13}$$

where $\mathscr{D}_e, r_e$ are the well depth and equilibrium internuclear separation and $\beta(r)$ is given by

$$\beta(r) = \beta_{\text{EMO}}(r) \equiv \sum_{i=1}^{N_\beta} \beta_i [y_q^{\text{ref}}(r)]^i, \tag{2.1.14}$$

where β_i are parameters and $y_q^{\text{ref}}(r)$ is a Šurkus-type variable (Šurkus et al. 1984) type given as

$$y_q^{\text{ref}}(r) = y_q(rlr_{\text{ref}}) \equiv \frac{r^q - r^q_{\text{ref}}}{r^q + r^q_{\text{ref}}}, \tag{2.1.15}$$

where i is a selected small positive integer and r_{ref} a chosen expansion centre.

The form of the MLR potential is represented by

$$V_{\text{MLR}}(r) \equiv \mathscr{D}_e \left[1 - \frac{u_{\text{LR}}(r)}{u_{\text{LR}}(r_e)} e^{\beta(r)\cdot y_p^{r_e}(r)}\right]^2, \tag{2.1.16}$$

where they have a very similar form to the EMO-type potentials except in that the radial variable in the exponent is now a Šurkus-type as in equation 2.1.15 with

$r_{\text{ref}} = r_e$. The function $u_{\text{LR}}(r)$ is defined as

$$u_{\text{LR}}(r) = \sum_{i=1}^{last} D_{m_i}(\rho r)\frac{C_{m_i}}{r^{m_i}}, \tag{2.1.17}$$

where $D_{m_i}(r)$ are "damping functions" and ρ is a system dependent range-scaling parameter. For our purposes $\beta(r)$ in equation 2.1.16 is defined as a polynomial expansion in two Šurkus-type variables, given as

$$\beta(r) = \beta_{\text{PE-MLR}}(r) \equiv y_p^{\text{ref}}(r)\beta_\infty + \left[1 - y_p^{\text{ref}}(r)\right]\sum_{i=1}^{N_\beta}\beta_i[y_q^{\text{ref}}(r)]^i. \tag{2.1.18}$$

This gives us the form of a polynomial-exponent MLR, or PE-MLR, which is the only type of MLR referred to in this work. More information on the formulation of these variables can be found in the paper describing the program LEVEL by Le Roy (2017).

2.1.9 Nuclear Motion Calculations

Our nuclear calculations are carried out on an adiabatic potential energy curve (PEC) with additional adiabatic and non-adiabatic corrections. Nuclear motion calculations can follow once an electronic structure is defined and the total Hamiltonian from equation 2.1.2 can be redefined by substituting the result of equation 2.1.3 for a given electronic state

$$\begin{aligned}\hat{\mathbf{H}}_{\text{total}}\Psi^i_{\text{total}} &= (\hat{\mathbf{K}}_n + \hat{\mathbf{H}}_{\text{elec}})\Psi^i_{\text{elec}}\Psi_{\text{nucl}} \\ &= \hat{\mathbf{K}}_n\Psi^i_{\text{elec}}\Psi_{\text{nucl}} + \hat{\mathbf{H}}_{\text{elec}}\Psi^i_{\text{elec}}\Psi_{\text{nucl}} \\ &= \hat{\mathbf{K}}_n\Psi^i_{\text{elec}}\Psi_{\text{nucl}} + \hat{\mathbf{E}}^i_{\text{elec}}\Psi^i_{\text{elec}}\Psi_{\text{nucl}}.\end{aligned} \tag{2.1.19}$$

Here we can take the first term of equation 2.1.19 and apply the differential chain rule and then make an approximation supported by the mass ratio of the nuclei and the electrons

$$\begin{aligned}\hat{\mathbf{K}}_n\Psi^i_{\text{elec}}\Psi_{\text{nucl}} &= \Psi^i_{\text{elec}}\hat{\mathbf{K}}_n\Psi_{\text{nucl}} + \Psi_{\text{nucl}}\hat{\mathbf{K}}_n\Psi^i_{\text{elec}} + \text{mixed derivatives} \\ &\approx \Psi^i_{\text{elec}}\hat{\mathbf{K}}_{\text{n}}\Psi_{\text{nucl}},\end{aligned} \tag{2.1.20}$$

where the electron nuclear mass ratio makes the second two terms have very small integrals in comparison to that of the first term. Now using the above and the fact that $\hat{\mathbf{E}}^i_{\text{elec}}$ is an not an operator with regards to Ψ^i_{elec} we can continue from equation 2.1.19

$$\begin{aligned}
\hat{\mathbf{H}}_{\text{total}}\Psi^i_{\text{total}} &\approx \Psi^i_{\text{elec}}\hat{\mathbf{K}}_n\Psi_{\text{nucl}} + \Psi^i_{\text{elec}}\hat{\mathbf{E}}^i_{\text{elec}}\Psi_{\text{nucl}} \\
&= \Psi^i_{\text{elec}}(\hat{\mathbf{K}}_n\Psi_{\text{nucl}} + \hat{\mathbf{E}}^i_{\text{elec}}\Psi_{\text{nucl}}) \\
&= \Psi^i_{\text{elec}}(\hat{\mathbf{K}}_n + \hat{\mathbf{E}}^i_{\text{elec}})\Psi_{\text{nucl}} \\
&= \Psi^i_{\text{elec}}(\hat{\mathbf{K}}_n + \hat{\mathbf{E}}^i_{\text{elec}})\Psi_{\text{nucl}} \\
&= \Psi^i_{\text{elec}}E^i_{\text{total}}\Psi_{\text{nucl}} \\
&= E^i_{\text{total}}\Psi_{\text{total}}.
\end{aligned} \tag{2.1.21}$$

So the total molecular wavefunction can be solved within the Born-Oppenheimer approximation by solving the nuclear motion within the potentials which are the solutions of the electronic structure calculations, the PECs $\hat{\mathbf{E}}^i_{\text{elec}}$. Consequently, a nuclear motion code, see section 2.3.2, only requires the PECs from an electronic structure calculation to solve for the nuclear wavefunctions and total energies.

2.1.10 Born-Oppenheimer breakdown

Within the accuracy of the *ab inito* quantum chemistry calculations of the electronic structure there is no significant difference between the three different isotopologues of BeH, BeD and BeT. However when it comes to the nuclear motion calculations the difference is immediately obvious with the heaver isotopologues having decreasing spacing between vibrational energy levels, more of them and tighter vibrational wavefunctions. There are more subtle differences in the rovibronic levels also which occur as the Born-Oppenheimer approximation loses validity. The significance of these changes depend on the specific isotopologue in question. These changes can however still be accounted for with the inclusion of BOB terms to the electronic potentials, as given by Le Roy (2017). The first of these is an adiabatic correction

which is a simple addition to the potential that scales with mass. It has the form

$$\left(\frac{M_a - M_a^{\text{ref}}}{M_a}\right)\left(y^{r_e}_{p\,\text{ad}}(r)u^a_\infty + \left[1 - y^{r_e}_{p\,\text{ad}}(r)\right]\sum_{j=0}^{N^a_{\text{ad}}} u^a_j [y^{r_e}_{q\,\text{ad}}(r)]^j\right), \tag{2.1.22}$$

where M_a is the mass of the specific isotope of the atom $a = Be$ or H, M_a^{ref} is the mass of the chosen reference isotope of that species, u^a_∞ and u^a_j are parameters to be fit, $y^{r_e}_{p\,\text{ad}}(r)$ and $y^{r_e}_{q\,\text{ad}}(r)$ are of the Šurkus variable type as given in equation 2.1.15, but where $r_{\,\text{ref}} = r_e$. There is also a non-adiabatic correction which is a multiplicative factor on the centrifugal potential, $[1 + g_B e(r) + g_H(r)]$, and it takes the form

$$\left(\frac{M_a^{\text{ref}}}{M_a}\right)\left(y^{eq}_{q\,\text{na}}(r)t^a_\infty + \left[1 - y^{eq}_{q\,\text{na}}(r)\right]\sum_{j=0}^{N^a_{\text{na}}} t^a_j [y^{eq}_{q\,\text{na}}(r)]^j\right), \tag{2.1.23}$$

where this is a very similar form to that of equation 2.1.22 except that there is no separate integer $p_{\,\text{na}}$, parallel to $p_{\,\text{ad}}$ of equation 2.1.22, since no general theoretical prediction of the limiting long range behaviours of these functions is available, see Le Roy (2017).

2.2 R-Matrix Method

We use the R-matrix method (Burke 2011, Tennyson 2010), the theory in this section coming largely from Burke (2011). It spatially separates the scattering problem into an inner and an outer region. The two regions are separated by a sphere of radius $r = a$ upon which the energy-dependent R-matrix is constructed.

2.2.1 Inner Region

In the inner region, quantum chemistry methods are used to produce full scattering-energy-independent wavefunctions for the target molecule and for the target molecule plus the scattering electron. The form of the inner region wavefunction for a given set of total symmetry is

$$\Psi_k = \hat{A} \sum_{i,j} c_{ijk} \psi_i^N \eta_j + \sum_m b_{mk} \psi_m^{N+1}, \tag{2.2.1}$$

where k is the index for the whole inner region solution Ψ_k. On the right of the equation the first of the two terms is a sum over i, j, respectively the indices for the scattering channels, and the continuum orbitals within a channel, ψ_i^N are the N-electron target solutions and η_j are the continuum spin-orbitals, where c_{ijk} is the coefficient for the i^{th}, j^{th}, k^{th} term. Scattering channels are the final asymptotic state of the system, i.e. resolved target states that obey symmetry rules in combination with the scattering electron. The index j is constrained to a set of η_j continuum spin-orbitals which, dependent upon the target state ψ_i^N, satisfy the symmetry $\mathrm{SYM}[\psi_i^N \eta_j] = \mathrm{SYM}[\Psi_k]$. $\hat{A}$ is an anti-symmetriser as with the Slater determinant above in equation 2.1.9 and 2.1.10 and deals with swapping electrons between the N-electron wavefunction and the continuum spin-orbital. The second term, called the L^2 term, is necessary to describe polarisation/correlation and resonance formation, this involves forming a wavefunction of the target molecule plus the scattering electron using occupied and virtual target orbitals, the N+1-electron solution, ψ_m^{N+1}, where b_{mk} is the coefficient for the m^{th}, k^{th} term and m is an index over the N+1 solutions. ψ_i^N and ψ_m^{N+1} are both multi-Slater wavefunctions as defined in equation 2.1.11.

The inner region wavefunction in equation 2.2.1 is the solution of the inner region expressed as

$$\langle \Psi_k | \hat{\mathbf{H}}^{N+1} + \mathscr{L}^{N+1} | \Psi_{k'} \rangle = E_k \delta_{k,k'}, \tag{2.2.2}$$

where $\hat{\mathbf{H}}^{N+1}$ is the Hamiltonian of the inner region, $\mathscr{L}^{N+1}$ is an addition called the Bloch term (Bloch 1946), and E_k are the energies of the inner region total (N+1) eigenfunctions. The Bloch term is necessary to ensure Hermicity over the confined region of space in the inner region of the R-matrix sphere of radius a_0 and it is given as

$$\mathscr{L}^{N+1} = \frac{1}{2} \sum_{i=1}^{N+1} \delta(r_i - a_0) \left(\frac{d}{dr_i} - \frac{b_0 - 1}{r_i} \right), \tag{2.2.3}$$

where b_0 is an arbitrary constant which may be set to zero and r_i are electron co-ordinates. The Bloch terms makes, by construction, $\hat{\mathbf{H}}^{N+1} + \mathscr{L}^{N+1}$ Hermitian over the internal region of the sphere of radius a_0. The application of a Buttle correction is here not necessary as the functions satisfy arbitrary boundary conditions.

2.2.2 R-matrix Boundary

At the boundary the inner region wavefunction matches onto the outer region reduced radial wavefunction, which is given by

$$F_i(a_0) = \sum_{i'=1} R_{ii'}(r_{N+1}, E) \left(r_{N+1} \frac{dF_{i'}(r_{N+1})}{dr_{N+1}} - b_o F_{i'}(r_{N+1}) \right) \Bigg|_{r_{N+1}=a_0}, \tag{2.2.4}$$

where the constant b_0 may be set to zero. Here the reduced radial wavefunction is being given as a function of its derivative and the link between the inner and outer functions, the titular radial or R-matrix. The elements of the R-matrix, $R_{ii'}(r_{N+1} = a_0, E)$, which are functions of the scattering energy and the scattering electron coordinates and are given as

$$\begin{aligned} R_{ii'}(a_0, E) &= \frac{1}{2a_0} \sum_{k}^{\infty} \frac{w_{ik} w_{i'k}}{E_k - E} \\ \text{where } \; w_{ik} &= \left\langle \psi_i^N \middle| \Psi_k \right\rangle \Big|_{r^{N+1}=a_0} = \sum_j c_{ijk} \eta_j(a_0), \end{aligned} \tag{2.2.5}$$

where term definitions are as above, and $R_{ii'}$ is an initial and final channel element of the R-matrix, a_0 is the radius of the R-matrix sphere, and E_k are the energies of the inner region solutions Ψ_k referred to as the R-matrix poles. The bra-ket $\left\langle \psi_i^N \middle| \Psi_k \right\rangle$ is being integrated over the N-electron coordinates and the remaining electron coordinate of r^{N+1} is evaluated at a_0. E, the total scattering energy, is given as

$$E = E_i^{\text{kinetic}} + E_i, \tag{2.2.6}$$

where E_i^{kinetic} is the incoming scattering electron kinetic energy and E_i the target state energy associated with channel i (eigenenergy of target bound state Ψ_i^N).

2.2.3 Outer Region

The outer region wavefunction is a function of the energy of the scattering electron and it is given as

$$\Psi^{N+1}(E) = \sum_{i=1}^{n} \psi_i^N F_i(r_{N+1}) Y_{l_i,m_i}(\theta,\phi), \tag{2.2.7}$$

where the radial part, $F_i(r_{N+1})$, has been generalised to a function over the scattering electron coordinates, the sum over i goes from $1 \rightarrow n$, the number of channels, $Y_{l_i,m_i}(\theta,\phi)$ is a spherical harmonic function (Weisstein 2004), and ψ_i^N is a target molecule wavefunction. The spherical harmonics, $Y_{l_i,m_i}(\theta,\phi)$, link to the angular momentum (partial wave) of the channel, i, as shown by the sum script on the angular momentum, l_i, and magnetic angular momentum, m_i, quantum numbers. This gives us a partial wave model of the scattering wavefunctions where computationally only a finite number of partial waves, angular momenta l_i, are included in the summation calculations given by equation 2.2.7. This leaves a infinite number of partial waves unaccounted for, a problem which is partially addressed below in section 2.2.10.

The asymptotic solutions to the reduced radial functions for when channel i to channel i' is open is given as

$$F_{ii'}(r_{N+1} \rightarrow \infty) \approx \frac{1}{\sqrt{k_i}} (\delta_{ii'} \sin\theta_i + K_{ii'} \cos\theta_i), \tag{2.2.8}$$

where k_i is the scattering wave number for channel i and is given as $k_i = \sqrt{2E_i^{\text{kinetic}}}$ where E_i^{kinetic} is as defined in equation 2.2.6, being proportional to the scattering electron momentum. θ_i is the channel angle and is given as $\theta = k_i r - \frac{1}{2} l_i \pi$. $K_{ii'}$ are the elements of the K-matrix, explained below.

From its initial calculation at the boundary the R-matrix is incrementally calculated propagating outwards radially until a convergence is reached. In programmatic terms this is not a propagation to infinity as equation 2.2.8 would suggest, but just to some finite large distance usually of the order of 100 a.u.. This propagation of the R-matrix, proportional to the wavefunction divided by its derivative (see equation 2.2.4) has greater numerical stability than a direct propagation of the wavefunction. The propagation uses the asymptotic expansion method of Gailitis (1976) which impose boundary conditions on the reduced radial wavefunctions (see equation 2.2.4) through their matching to the asymptotic solutions (see equation 2.2.8) (Noble and Nesbet 1984). The final, converged, R-matrix is used to calculate K-matrices which are functions of the scattering energy, which are related to the scattering eigenphases. The K-matrix elements given by equation 2.2.8 form a matrix as

$$\mathbf{K}(E) = \sum_{i,i'} K_{ii'}(E) \left|i\right\rangle \left\langle i'\right| . \tag{2.2.9}$$

The K-matrices are used to calculate T-matrices which are related to the scattering cross-sections, and are given as

$$\mathbf{T} = \frac{2i\mathbf{K}}{\mathbf{I} - i\mathbf{K}}, \tag{2.2.10}$$

where $\mathbf{T}$ are T-matrices, $\mathbf{K}$ are K-matrices, $\mathbf{I}$ is the identity matrix and i is the imaginary unit.

T–matrices are used to calculate the cross-sections for inelastic processes as given by Burke (2011)

$$\sigma(i \to j) = \frac{\pi}{k_i^2} \sum_S \frac{2S+1}{2(2S_i+1)} \sum_{l_i L_j} \left| \hat{\mathbf{T}}^{S\Gamma}_{il_i jl_j} \right|^2, \tag{2.2.11}$$

where i, j denote an initial and a final state ($i \neq j$), k_i is as defined above, S_i is the spin of the state i and the total spin of the system is S, Γ represents spacial symmetry, and l_i, l_j represent the partial wave connected with the initial and final states i, j. For elastic cross-sections ($i = j$) equation 2.2.11 using T-matrices will not work and so we use S-matrices which are given as $\mathbf{S} = \mathbf{T} - \mathbf{I}$.

2.2.4 Scattering models

The description of the scattering model involves including an additional set of orbitals to represent the continuum which must be orthogonal to the orbitals used to represent the target and the addition of the scattering electron. The simplest scattering model is the static exchange (SE) model, consisting of a HF target, $i = 1$ in Equation 2.2.1. In this model the ψ_m^{N+1} functions are formed by the target wavefunction, ψ_1^N, multiplied by singularly occupied target virtual spin-orbitals, $m = 1$ to the number of virtual spin-orbitals included. This type of calculation is only able to represent electronically elastic collisions since there is only one target state. The lack of excited states also limits the resonances that can be represented to shape resonances.

The static exchange plus polarisation (SEP) model includes all the L^2 functions generated in a static exchange (SE) calculation and an additional set of L^2 functions in which a single electron is excited into the the virtual orbitals along with the scattering electron. This model represents collisions where the incoming electron momentarily polarises the target molecule in the interaction but leaves it in the initial state, asymptotically, after scattering. Thanks to the polarisation it can represent some Feshbach resonances, as well as the shape resonances. However, like the SE model, it does not include any excited states and therefore cannot give parent states for these Feshbach resonances and it represents only elastic scattering.

Using any target model with more than one target electronic state produces what is called a close coupling (CC) scattering model. One target model that can be used to achieve this would be the CAS-CI; this method (Tennyson 1996) and its special case the frozen core full configuration interaction (FC-FCI) are used extensively in this work. Target states are the states formed by the CAS-CI and the

ψ_m^{N+1} functions are formed by adding one more electron to the CAS, where the CAS for the $N+1$ wavefunction has optionally been increased by the addition of virtual spin-orbitals.

The most complete treatment of the scattering model is a close coupling-full configuration interaction (CC-FCI) calculation. This method has the advantage that it allows a balanced treatment of the target and scattering problems as demonstrated in scattering calculations for few-electron targets (Stibbe and Tennyson 1997). It forms target states by an FCI calculation and the ψ_m^{N+1} functions are formed by adding one more electron to the CAS. Here the addition of virtuals is unnecessary and would also impossible as the target CAS already contains all the spin-orbitals as per the definition of the FCI. A close coupling-frozen core full configuration interaction (CC-FC-FCI) calculation comes close to this level of accuracy as here also all spin-orbitals are already included in the target model. The only loss on a frozen core method is in the flexibility of the wavefunction as the core electrons cannot move from the core orbitals. The impact of this is discussed below in the target model results.

2.2.5 Representation of the continuum

In our calculations the continuum orbitals (see $\eta_j(\mathbf{r})$ in Equation 2.2.1) are built from an additional set of continuum functions centred on the centre of mass (Faure et al. 2002) orthogonalizing the continuum functions against the given set of target orbitals. The orthogonalization proceeds by performing at first Gramm-Schmidt orthogonalization of the continuum orbitals against the set of target orbitals. In the second step the continuum orbitals are orthogonalized using symmetric orthogonalization and those continuum orbitals with eigenvalue of the overlap matrix smaller than a given threshold are removed from the basis. The last step is crucial to maintain numerical stability of the integral calculation: continuum orbitals corresponding to eigenvalues of the overlap matrix smaller than approximately 10^{-7} contain large coefficients with alternating signs which can cause a significant precision loss (even in double precision) when performing transformation of the atomic integrals to the molecular orbital basis. In other words, a careful choice of the deletion thresh-

old is needed to prevent numerical linear dependency problems in the continuum orbital basis.

In the UKRMol suite the continuum functions are GTOs, derived as described by Faure et al. (2002). There is a linear molecules code which has an option to use a Slater type orbital (STO) (Slater 1930) basis set for the target and numerically defined continuum basis set. This STO option has the advantage of being usable with an arbitrarily large R-matrix sphere. However, due to the numerical continuum it suffers from numerical problems to do with the need to evaluate the molecular integrals numerically which leads to linear dependence difficulties with larger target basis sets, especially at larger energies. Therefore it is not acceptable for use in this project. In practice recent high-accuracy studies have used the GTO option even for diatomic molecules (Little and Tennyson 2013, 2014) where the integrals over the interior of the R-matrix sphere can be evaluated efficiently and accurately (Morgan et al. 1997).

However use of GTOs to represent the continuum puts a strong upper limit on the size of the R-matrix sphere, because increasing the radius of the sphere lowers the effective energy range for which the continuum basis is sufficiently good (Tarana and Tennyson 2008). This problem can be solved by adding more continuum basis functions but only up to a certain number of functions: too many continuum basis functions will cause numerical linear dependence problems within the continuum.

These limitations are best overcome by substituting the radial parts of the continuum GTOs with functions more suitable for representation of the oscillating continuum wavefunction such as numerical functions with compact support. This is the approach used in the new UKRMol+ (Zdenek Mašín 2017, Darby-Lewis et al. 2017) suite where the Gaussian radial part of the continuum functions is replaced with B-splines. As opposed to Gaussians the B-spline radial basis set is very flexible and does not suffer from numerical linear dependencies. The corresponding B-spline type orbital (BTO) has the form (Zatsarinny 2006)

$$\mathscr{B}(\mathbf{r})_{i,l,m} = \frac{B_i(r)}{r} X_{lm}(\Omega), \tag{2.2.12}$$

where $B_i(r)$ is the i-th radial B-spline drawn from the set of B-splines which are uniquely specified by the set of knots, breakpoints and polynomial order of the B-splines and $X_{lm}(\Omega)$ is the real spherical harmonic. B-splines have been used successfully in various atomic (Zatsarinny and Bartschat 2004, Zatsarinny 2006) and molecular calculations (Sanchez and Martin 1997, Bachau et al. 2001). However, to the best of our knowledge there is currently no application of B-splines to represent the continuum in molecular problems where the target molecule is represented by the standard quantum chemistry form of atom-centred GTOs. This application of BTOs to molecular R-matrix calculations was developed in code by Zdenek Mašín (2017).

In our approach the BTOs and the continuum GTOs can be mixed freely. This approach is useful when the set of BTOs (radial B-splines) is chosen to span the radial range $a_{GTO} < r \leq a$, i.e. the radial range outside of the sphere with radius a_{GTO} up to the radius of the R-matrix sphere a. It is convenient to choose a_{GTO} so that all core-type GTOs and possibly the inner valence GTOs are fully contained inside it. Consequently, all mixed BTO/GTO integrals involving the product of a GTO fully contained inside the sphere $r \leq a_{GTO}$ and a BTO are zero, thus alleviating substantially the computational demand required to calculate the mixed integrals. For small and medium-sized molecules a_{GTO} would be typically less than about 5 Bohr. In this reduced radial range, GTOs can be used to represent the continuum without linear dependency problems and to give a good representation over a wide energy range. The long distance part of the continuum wavefunction is represented by BTOs: the quality of the radial wavefunction is controlled easily by the density of the knots and the order of the B-splines. Finally, we note that our codes do not require the use of continuum GTOs, i.e. in principle only BTOs can be used over the whole radial range ($a_{GTO} = 0$) and vice-versa the new method for continuum representation does not require the use of BTOs, i.e. the traditional GTO-only approach ($a_{GTO} = a$) is still available.

Despite their attractive properties in describing the continuum, the use of numerical functions leads to the problem of performing an efficient and accurate cal-

culation of the multi-centric molecular integrals involving the numerical function and the GTOs. An approach combining the use of a finite element method - discrete variable representation (FEM-DVR) for the continuum and atom-centred GTOs has been used successfully for small molecules in the photo-ionisation calculations of Yip et al. (2014). Legendre expansion of the Coulomb potential and Lebedev numerical quadrature were used to calculate required molecular integrals for one and two particles in the continuum.

2.2.6 Structure of the UKRMol+ Inner Region Codes

The calculation of both GTO-only and the mixed BTO/GTO molecular integrals has been implemented in a new integral library (Zdenek Mašín 2017). The new code replaces completely the original GTO integral core of the inner region part of the UKRMol suite (programs swmol3, sword, swtrmo, gausprop, swedmos) with a single new binary (scatci_integrals). The calculation of the atomic integrals, generation of the continuum orbitals and the integral transformation are all carried out at once using a parallelised integral library. The new integral library and the set of UKRMol programs adapted to it form the UKRMol+ suite of codes.

The polyatomic codes UKRMol and UKRMol+, in common with most quantum chemistry codes, cannot use full linear symmetry. Figure 2.1 shows a flow diagram of the binaries involved in the UKRMol+ calculations in this work. All calculations presented here were therefore performed in C_{2v}; C_{2v}-symmetry notation is used when discussing input to the codes but all final results, except for eigenphases, are transformed to the full ($C_{\infty v}$) symmetry notation which is straightforward to achieve. Table 2.1 gives the C_{2v} to $C_{\infty v}$ translation as used in this work. The total symmetry is a combination of spacial and spin symmetry, that is, due to the addition of the scattering electron, the scattering symmetry is different from the target symmetry by a change in the total spin of $\frac{1}{2}$. This is equivalent to a change from even to odd (or vice versa) multiplicity between the target molecule and the scattering symmetries.

The integral calculation requires on input a set of molecular orbitals saved in the MOLDEN format (Schaftenaar and Noordik 2000) which can be obtained using

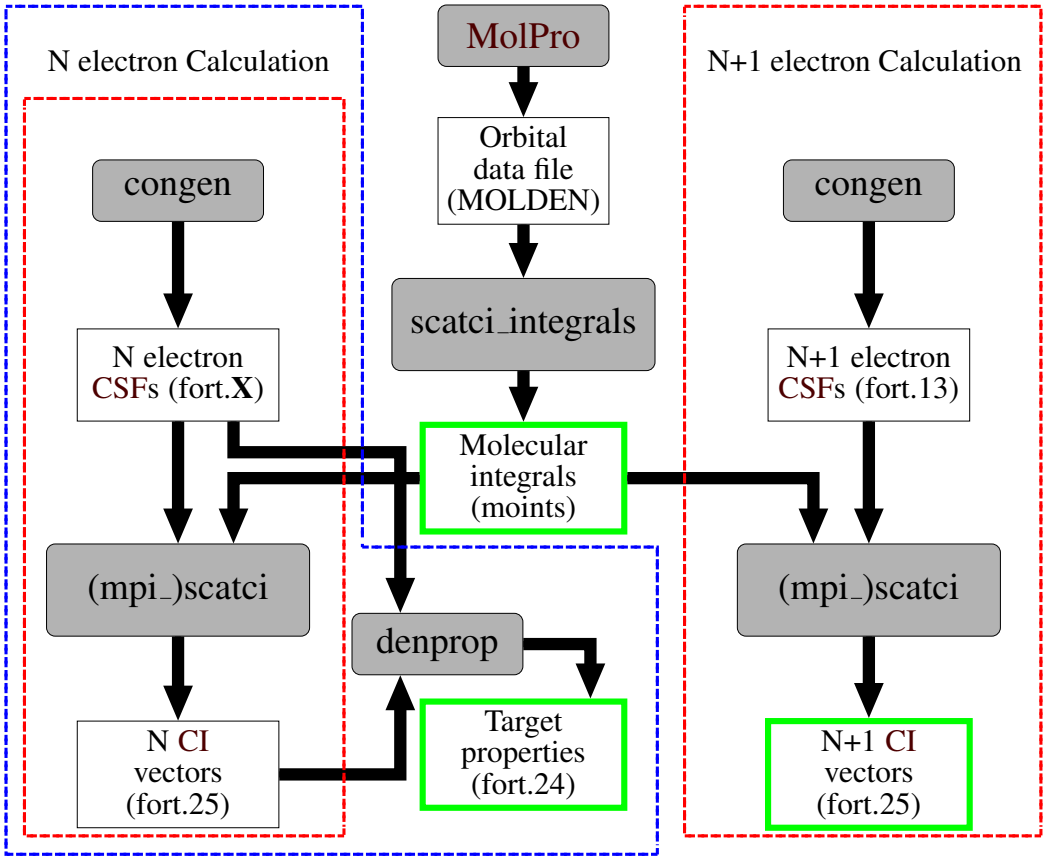

Figure 2.1: Flow diagram showing the inner region UKRMol+ calculation. Programs are in rounded boxes with grey backgrounds and output data files are in sharp cornered boxes with white backgrounds. Output files in the green boxes are needed for the outer region calculation. The "moints" file is soft linked to fort.16 and fort.17 for the N electron scatci calculation, to fort.17 for the N+1 scatci calculation and then to fort.22 for sw_interf in the outer region. The two dashed red boxes, left and right, are repeated for each N and N+1 symmetry respectively. The blue dashed box is the target calculation.

a range of quantum chemistry software; in this work MolPro (Werner et al. 2012) was used. The integral calculation is carried out by the scatci_integrals program and all the integrals, atomic and molecular basis sets are saved in a single file and accessed by the standard UKRMol (Carr et al. 2012) programs.

Hamiltonian construction and diagonalisation is carried out by scatci or mpi-scatci (Al-Refaie and Tennyson 2017). For the N electron calculation this requires the N-electron CSFs generated by congen, in fort.**X**, and the N electron molecular integral calculations by soft linking the moints file to fort.16 and fort.17. This produces eigen-energy and eigen-vector results on file fort.25. For a calculation with

multiple target states (i.e. a CI calculation) this requires a congen and scatci calculation for each symmetry for which there are target states. The results from each of these calculations are concatenated in different sets into the same fort.25 file. The fort.**X** files from congen calculations are given per symmetry, usually **X**=69 + *S* where *S* equals zero to max symmetries minus one. Dipoles and quadrupoles are then calculated by denprop and along with target energies and quantum numbers are printed into a file containing all the target electronic information, fort.24. For the N+1 electron calculation scatci requires the moints file to be softlinked to fort.17 and the N+1 electron CSFs from congen on fort.13. The N+1 congen and scatci calculation is repeated for each N+1 (scattering) symmetry. The results can be saved in separate fort.25 files or in the same file in concatenated sets. An interface to the cdenprop program used for photoionization calculations has been implemented too but not used as part of the work in this project (Harvey et al. 2013). Three files produced in this inner region calculation need to be preserved for use in the outer region calculation; they are the molecular integral file, moints, the target properties file, fort.24, and the N+1 CI vectors file, fort.25.

2.2.7 Structure of the UKRMol+ Outer Region Codes

The outer region codes of the UKRMol suite remain mostly unchanged for use in UKRMol+ but have received updated routines in sw_interf for reading the scatci_integrals output. The three files preserved from the inner region calculation now serve as the basis for constructing an R-matrix and propagating it to obtain scattering quantities. First however the inner region data is converted into a format which is used by the outer region codes. This is done by sw_interf and results in a channel data file, fort.10 and a boundary amplitudes data file, fort.21. This and subsequent steps in an outer region calculation are shown in a flow chart in figure 2.2. The individual binaries are discussed further below.

After the inner region conversion is performed by sw_interf all the necessary inner region data is contained in the two files it produced and only fort.24 from the inner region need be retained, as it is used by some outer region binaries (not shown in figure). The R-matrix is actually formed and propagated by the program r_solve,

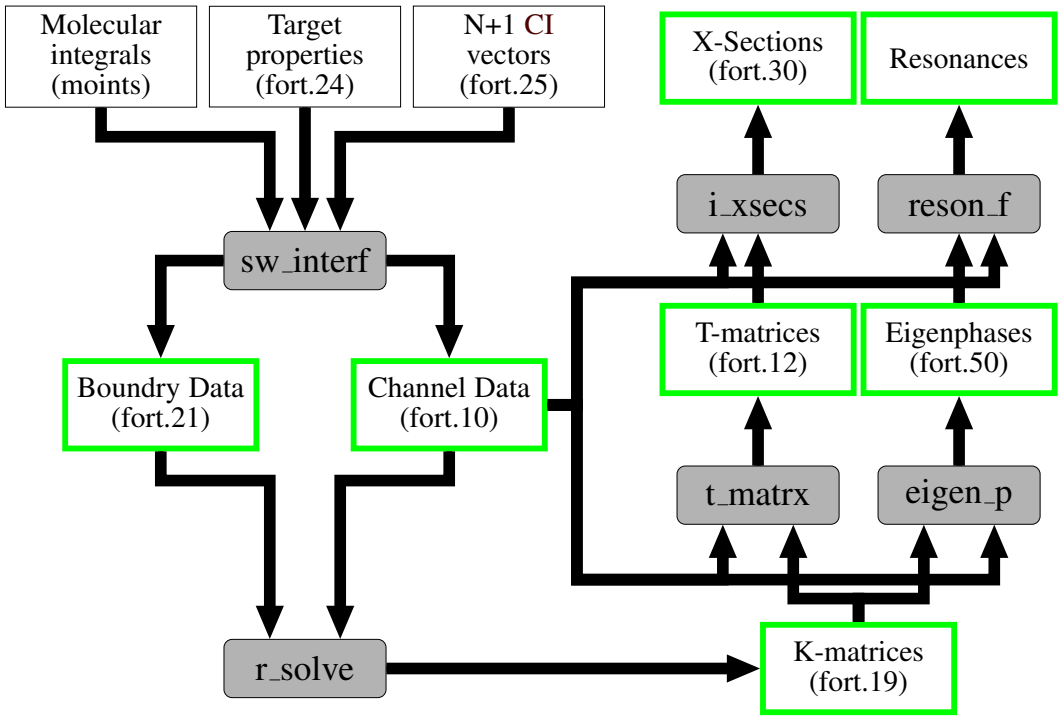

Figure 2.2: Flow diagram showing the outer region UKRMol+ calculation. Programs are in rounded boxes with grey backgrounds and output data files are in sharp cornered boxes with white backgrounds. Output files in the green boxes contain final scattering data. The "moints" file is soft linked to fort.22 for sw_interf. X-sections is short for cross-sections.

which produces K-matrices that are written to fort.19. The K-matrices and the channel data file are both used by t_matrx and eigen_p, these programs respectively calculating the T-matrices, file fort.12, and the eigenphases, fort.50. The program i_xsecs then calculates the X-sections, short for cross-sections, from the T-matrices.

The program reson_f (Tennyson and Noble 1984) can be used to calculate resonances from the eigenphases (Tennyson and Noble 1984) and is recursive, meaning that it calculates new K-matrices at new energies to give a finer grid for finding and isolating resonances. It finds resonances by fitting eigenphases to the Breit-Wigner form (Breit and Wigner 1936) which is given as

$$\delta(E) = \delta_o(E) + \sum_{i=1}^{m} \tan^{-1}\left(\frac{\Gamma_i}{2(E_i^{\text{res}}) - E}\right), \tag{2.2.13}$$

where E_i^{res}, Γ_i are the the resonance positions and widths respectively and $\delta_0(E)$ represents the background eigenphase contribution; in reson_f, these are considered

to be low order polynomials.

Each of the binaries represented here can be compiled into a single executable which contains the binaries you wish to run or alternatively can be compiled into separate binaries and run individually.

2.2.8 Vibrational Resolution

In this work I have programmed two methods for the vibrational resolution of R-matrix electron scattering data. R-matrix data produces elastic and inelastic electronic channels and the aim is to have elastic and inelastic vibronic channels. The two methods are implemented in two different programs: the first and simpler method uses Franck-Condon factors (Franck and Dymond 1926, Condon 1926) and single-geometry R-matrix results and is implemented in the program fcfcros; the second approach uses vibrational wavefunction averaging and multi-geometry R-matrix results and is implemented in the program vibaver. The methods are explained in detail below in sections 2.2.8.1 and 2.2.9 and a flow chart showing the operation of each program is given in figure 2.3.

Vibrational resolution of cross-sections from R-matrix calculations has been performed using both these methods before (Danby and Tennyson 1991, Stibbe and Tennyson 1997, Rabadán et al. 1998, Teillet-Billy et al. 1999). There have also been recent calculations on BeH^+ cation vibrational resolution (Laporta et al. 2017, Faure et al. 2017). As far as we are aware only the FCF method has so far been applied to BeH (Celiberto et al. 2012a).

2.2.8.1 Franck-Condon Factor Method

The simplest method for achieving vibronic resolution from electronic scattering results is to use a weighted averaging approach where the electronic inelastic results are split into an initial vibrational state in the initial electronic level and a final vibrational state in the final electronic level. The value of the weights is given by the overlap of the initial and a final vibrational wavefunctions, this is a Franck-Condon factor (FCF). FCFs are calculated by the nuclear motion code Duo (Yurchenko et al.

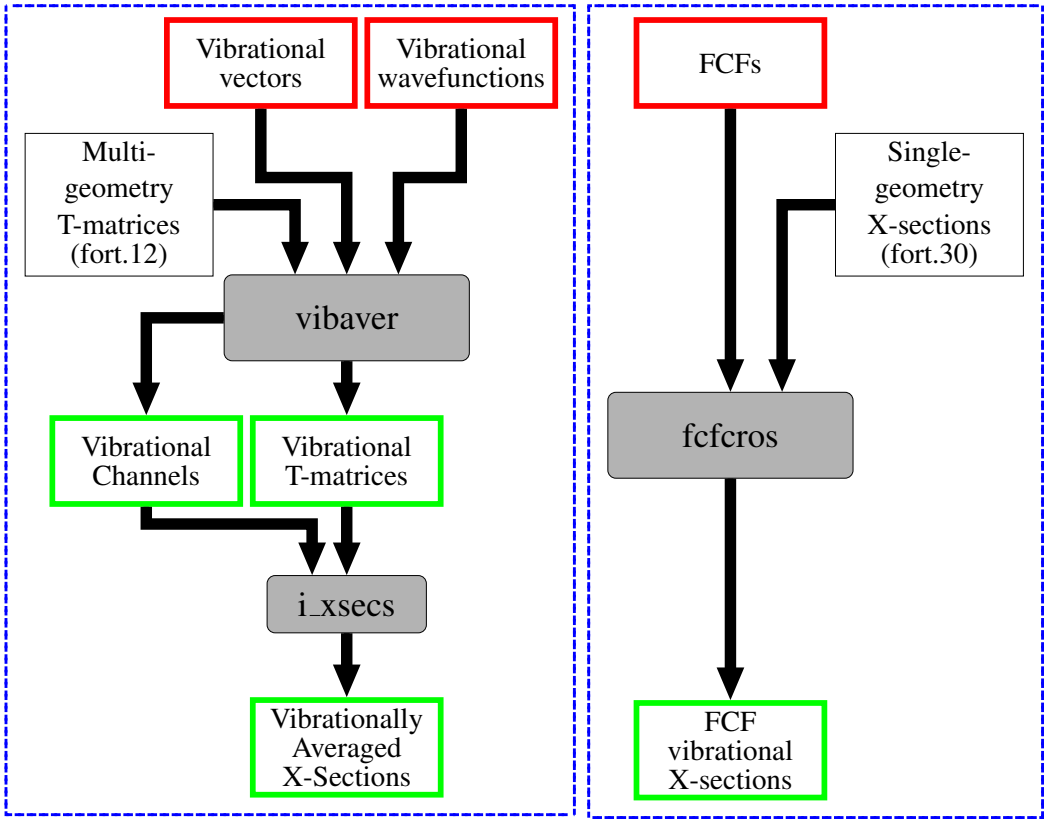

Figure 2.3: Flow diagram showing the two paths taken to vibrational resolution. Programs are in rounded boxes with grey backgrounds and data files are in sharp cornered boxes with white backgrounds. Output data files in green are scattering quantities, and in red are files from nuclear motion code Duo. The left blue dashed box shows vibrational resolution by the vibrational averaging of multi-geometry T-matrices, the right dashed box shows the use of Franck-Condon factors and single geometry scattering calculations.

2016) and are given by the formula (Franck and Dymond 1926, Condon 1926)

$$F_{e'',v'',e',v'} = \int |\left\langle \phi_{e'',v''}(R) \middle| \phi_{e',v'}(R) \right\rangle|^2 dr = \begin{cases} 0 \to 1, & \text{Real number between 0 and 1,} \\ \delta_{v'',v'}, & \text{if } e'' = e', \end{cases} \tag{2.2.14}$$

where e', v' here indicate the initial electronic and vibrational state, e'', v'' indicate the final electronic and vibrational state, and $\left|\phi_{e',v'}(R)\right\rangle$ is the vibrational wavefunction from the electronic state e' and with vibrational quanta v'. Within a given electronic state all FCFs are zero except those between the same vibrational state. This is assuming that the vibrational wavefunctions are totally and perfectly or-

thornormal, otherwise there maybe off diagonal values within an electronic state. This is likely to occur computationally and numerically where the integral cannot truly go over all space and thus there is not complete closure with the basis of the vibrational wavefunctions. The vibronic resolution from FCFs is therefore elastic within an electronic state and can only be inelastic when there is a change in electronic state. The vibronic results can be given by T-matrices or by cross-sections, the former as block diagonal T-matrices and the cross-sections given by

$$\sigma_{e'',v'',e',v'}(E) = \sigma_{e'',e'}(E) F_{e'',v'',e',v'}, \tag{2.2.15}$$

where $\sigma_{e'',e'}$ is the electronically resolved cross section from the equilibrium geometry R-matrix calculation, E is the scattering energy, $F_{e'',v'',e',v'}$ is the FCF as defined above. This method requires only the equilibrium geometry R-matrix calculation data. The FCF method has previously been applied to R-matrix results for BeH by Celiberto et al. (2012a).

2.2.9 Vibrational Wavefunction Averaging

Vibrational averaging is the other method of producing vibronic scattering results which I have used in this project. The method of vibrational averaging is used to transform a function of geometry into a matrix with vibrational resolution. This method has been used previously and was also developed for ground electronic state vibrational excitation calculation with the UKRMol code (Rabadán and Tennyson 1999). My approach is to allow a vibronic (de)excitation from any vibronic state to any other. The method is applied in our application to T-matrices and is best understood by looking at a single geometry calculation for a T-matrix as an operator on electronic channels as

$$\hat{T}(E) = \sum_{e'',e'} C_{e'',e'}(E) \left|e''\right\rangle \left\langle e'\right|, \tag{2.2.16}$$

where $\hat{T}$ is the T-matrix, as a function of E, the scattering energy (in reality each energy is a separate calculation point), $C_{e'',e'}$ is the value of the T-matrix element with

initial electronic channel e' and final electronic channel e'' and the ket and bra pair represent those electronic channels. It should be noted that e' and e'' are electronic channels not electronic states, which means that they include the asymptotic state of both the target molecule (electronic state) and of the scattering electron (angular momentum of a partial wave); as such there may be multiple electronic channels each mapping to one electronic state i. Using this representation of the T-matrix we can also add the multi-geometry aspect by considering each calculation of $\hat{T}$ along with its internuclear separation, R_j to be $\hat{T}_{R_j}$ and concatenating these results along j to give a point-wise function of geometry $\hat{T}(R)$ just as we implicitly did so for the cross sections and T-matrices above in making them functions of scattering energy.

Now we can consider taking the expectation value of the T-matrices with the vibrational functions, because as functions of geometry they may now also be considered operators of the vibrational wavefunctions. Looking at calculating a single element of this new vibronically resolved T-matrix gives us

$$T_{i'',v'',i',v'}(E) = \left\langle \phi_{e'',v''}(R) \middle| \hat{T}_{i'',i'}(E,R) \middle| \phi_{e',v'}(R) \right\rangle, \tag{2.2.17}$$

where $T_{i'',v'',i',v'}(k)$ is an element of the vibronically resolved T-matrix (still a function of the scattering energy), $\left|\phi_{e',v'}(R)\right\rangle$ is a vibrational wavefunction as defined above for equation 2.2.14 and where e' is the electronic state represented in the electronic channel i', and $\hat{T}_{i'',i'}(E,R)$ is an element of the electronically resolved T-matrix, $\hat{T}_{i'',i'}(E,R) = C_{i'',i',R}(E)$.

The code developed in this work to do this process of vibrationally averaging electronic T-matrices is called vibaver. This program requires input from the R-matrix codes, specifically the inner region file fort.24 (target properties) and outer region files fort.10 (channels) and fort.12 (T-matrices) all for multiple geometries. It also requires input from Duo containing the vibrational wavefunctions and some auxiliary information. In this project the Duo files were already generated as part of the spectral modelling. The vibaver program is currently restricted in its use to only cover geometries between which electronic states do not cross each other.

One important note to make on this theory is the assumption made in linking

results from different geometries along the scattering energy axis. This is an issue because the definition of the total scattering energy, the energy of each outer region calculation, is not strictly geometry independent as it depends on the initial target state energy. The usual definition of the scattering energy is given as

$$E = E_{k,l} + E_l = E_{k,u} + E_u, \tag{2.2.18}$$

where the total energy E is the scattering energy at which calculations are performed and E_l, E_u are the energies of the upper and lower states, $E_{k,u}$ and $E_{k,l}$ are the electron kinetic energy linked with the upper and lower states (in a time dependent framework one would be the initial and the other the final kinetic energy of the electron). However the multi–geometry calculation means we are actually dealing with E_l and E_u which vary with geometry, and thus the definition of the total scattering energy, E, also varies with geometry as the electron kinetic energy is the geometry independent component. The assumption made in the vibrational averaging program vibaver is that the quantities $E_{k,l}$ and $E_{k,u}$ are geometry independent. The result of this assumption is given by the rearrangement of equation 2.2.18

$$E(R) = E_{k,l} + E_l(R) = E_{k,u} + E_u(R) \rightarrow E_{k,u} - E_{k,l} = \Delta E_{\text{ul}} = E_l(R) - E_u(R), \tag{2.2.19}$$

where the quantity ΔE_{ul} represents the difference in the initial and final kinetic energies which in a vibrationally averaging calculation comes to represent the difference in energy between the upper and lower vibrational states. This is a definitively geometry independent quantity. For the resultant equality of equation 2.2.19 to be true the geometry dependence of the upper and lower states must cancel each other out, i.e. the PECs must parallel. Provided this assumption is approximately true, valid it validates our concatenation of the multi–geometry results along the scattering energy. This is equivalent to the assumption made by Trevisan and Tennyson (2002) in asserting that: ”The bond-length dependent $E_{\text{out}} + \varepsilon(R)$ is not exactly the incoming electron energy E_{in}. However, this approximation is necessary to allow a well defined energy for the nuclear continuum function.”

2.2.10 Born correction and Principal of Detailed Balance and Extrapolation

The R-matrix method calculates the scattering results by propagating partial waves in the outer region for a finite number of angular momenta, from $l = 0$ to l_{max}. This means that there is in fact an infinite number of partial waves left unaccounted for, and even though it is the lowest partial waves which have the largest contribution the remaining waves, from l_{max} to $l = \infty$, can still include a significant area. This extra area is especially significant in the case where there is a strong long range dipole for the transition (or permanent dipole for an elastic cross-section). This is because, for neutral molecules, a long range dipole changes the long range potential from being $\propto 1/R^3$ to $\propto 1/R^2$.

We use a model for the Born cross-section detailed by Kaur et al. (2008) and implemented in the code borncros. The work of Norcross and Padial (1982) gives a more complete picture of electron scattering off by polar molecules. This takes the R-matrix cross-sections and adds a Born cross-section for $l = 0$ to ∞ and subtracts a Born cross-section from $l = 0$ to l_{max}.

$$\sigma_{tot}(E) = \sigma^{RMat}_{l=0\rightarrow l_{max}}(E) + \sigma^{Born}_{l=0\rightarrow\infty}(E) - \sum_{l}^{l_{max}} \sigma^{Born}_{l}(E), \tag{2.2.20}$$

where E is the scattering energy, $\sigma^{RMat}_{l=0\rightarrow l_{max}}$ is the cross-section from the R-matrix calculations, including contributions from partial waves of angular momenta up to $l = l_{max}$, $\sigma^{Born}_{l=0\rightarrow\infty}$ is the Born correction for all partial waves and σ^{Born}_{l} is the Born correction for a given partial wave. The reason for making the correction in this fashion is due to the existence of an analytical form of the Born cross-section from $l = 0$ to ∞ given by

$$\sigma^{Born}_{l=0\rightarrow\infty} = g_c \frac{8\pi}{3} \frac{D^2}{k_i^2} \ln \frac{(k_i + k_f)}{(k_i - k_f)}, \tag{2.2.21}$$

where D is the relevant dipole and k_i, k_f are the initial and final momentum of the scattering electron and g_c is a combined statistical weighting. The form of the partial and total Born cross-section is given by Kaur et al. (2008).

For elastic and lower to upper state transitions the Born correction is applied

as above however in the cases where the transition is from a higher energy state to a lower one I have modified the program to use the principle of detailed balance. The principle of detailed balance (Tolman 1979) uses the time-independence of electron scattering processes to calculate a cross-section from an upper state to a lower state using a cross-section from the lower state to the upper state. It is given by

$$\sigma_{l\rightarrow u}(E_{k,l})g_l E_{k,l} = \sigma_{u\rightarrow l}(E_{k,u})g_u E_{k,u} \tag{2.2.22}$$

where $\sigma_{l\rightarrow u}$ and $\sigma_{u\rightarrow l}$ are cross-sections from lower to upper and upper to lower states respectively, g_l, g_u are statistical weights for the lower and upper states, $E_{k,l}$ $E_{k,u}$ are electron kinetic energies which are related to the total energy as given in equation 2.2.18. This definition of energy is related to either vibrational state energies, which are geometry independent, or to single geometry electronic state energies. The addition of detailed balance to the borncros code was made by myself as a part of this project.

This has led to the borncros program being significantly changed, although the underlying physics remains the same. There is one final task for which the borncros code has been adapted. This is to extrapolate the cross-sections to higher energy regions. When there are dipoles, the extrapolations are made using the Born correction of equation 2.2.21, $\sigma^{Born}_{l=0\rightarrow\infty}(E)$, scaled to match the cross-section area for the last energy where the total cross-section, $\sigma_{tot}(E)$, is calculated. In the case where there is no significant dipole it just applies a $1/E$ scaling factor, which gives a faster decline in area than the and is the appropriate form for a non-dipole Born correction. This makes physical sense, since if there is no dipole the cross-section would be expected to be lower.

The use of the borncros program is shown as a flow chart in figure 2.4. The borncros code uses the cross-sections produced by i_xsecs (fort.30) and the inner region target properties file (fort.24) to produce a cross-sections file for the Born correction and a cross-sections file which contains the R-matrix cross-sections plus the correction. It also produces a separate, optional, set of files which contain cross-sections printed with the extrapolations and the scattering electron kinetic energy

rather than the total scattering energy present in the standard cross-sections files. The program can also work with the vibrational cross-sections produced from the vibrationally averaged T-matrices of vibaver by providing a file with vibrational energy corrections, containing the difference between the vibrational and electronic energies. This makes the calculation of rates much easier as these files can have their data directly convoluted with a Boltzmann distribution.

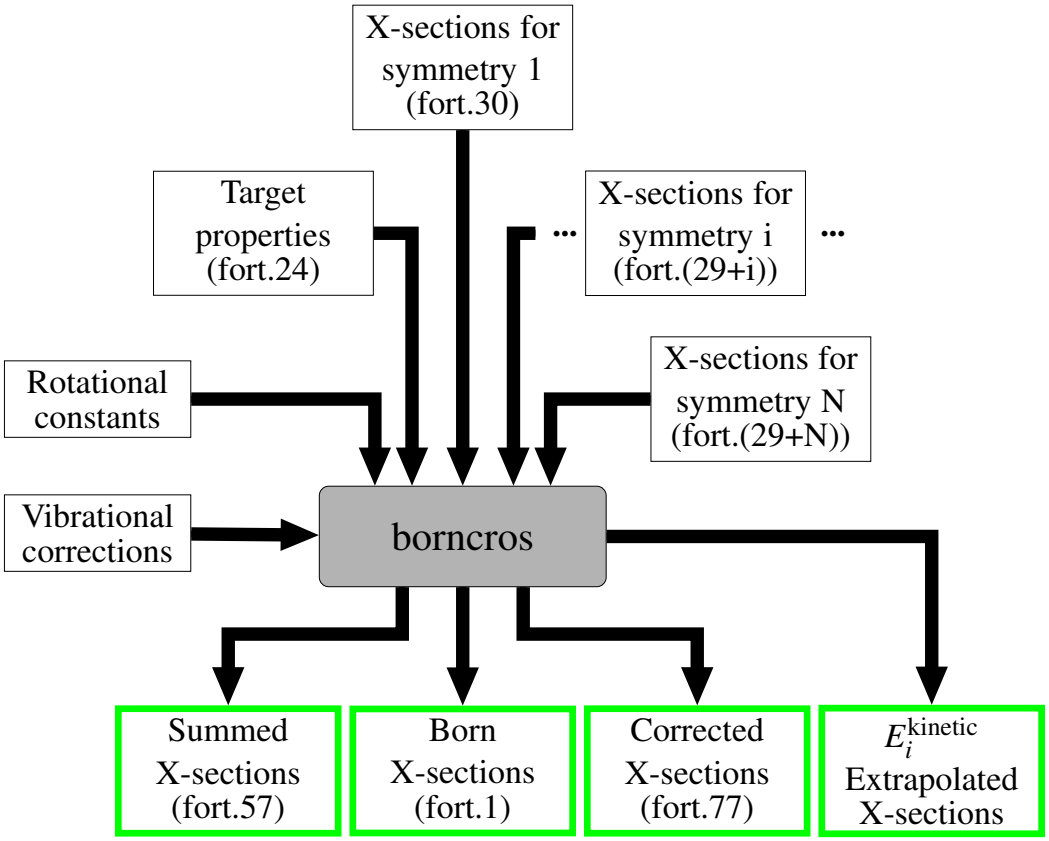

Figure 2.4: Flow diagram the use of the modified borncros program, in a rounded box with grey background, data files are in sharp cornered boxes with white backgrounds. Output data files containing cross–sections are in green.

2.3 Spectral Modelling

There are four main steps used here in generating assigned synthetic spectra fitted with rotational and vibrational temperatures. Experimental transitions are inverted to give vibronic energy levels using the online implementation of MARVEL (measured active rotation vibration energy levels)(Furtenbacher et al. 2007). These are then used in Duo to fit PECs which can accurately reproduce all the empirical energy levels. Empirical energy levels belonging to the X $^2\Sigma^+$, A $^2\Pi$ and C $^2\Sigma^+$ electronic states are provided by our MARVEL treatment, although PECs were fitted only for the X and A states. This is because of a lack of transition data for the C state, which in any case does not give rise to a significant feature in the JET emission spectrum (Darby-Lewis et al. 2018). To date, the molecular spectrum is dominated by the A – X band. I use an *ab initio* X state to A state transition dipole, from Pitarch-Ruiz et al. (2008), to produce Einstein A–coefficients for the observed X to A transitions. The output from Duo contains all transitions between states within a given wavenumber range (parameter in the Duo input, see supplementary data) and all the Einstein A–coefficients associated with those energy levels. These are used by ExoCross (Yurchenko et al. 2018) to generate synthetic spectra with varying rotational and vibrational temperatures. These spectra are compared to experimental spectra to obtain a metric for the fit.The flowchart in Figure 2.5 illustrates the links between the steps of this process, each step is presented in detail below.

2.3.1 MARVEL

The MARVEL procedure (Furtenbacher et al. 2007, Furtenbacher and Császár 2012) is implemented in a program with an online user interface (MARVEL Online) and works by taking experimental transition frequencies and calculates networks of empirical energy levels. These are called spectroscopic networks as they are networks of energy levels linked to each other by recorded spectroscopic transitions (Császár and Furtenbacher 2011). Each transition consists of (1) a transition frequency in cm^{-1} (2) as uncertainty in cm^{-1} (3) a set of assigned quantum numbers for the upper and one for the lower state and (4) a unique label referring to the source. The MARVEL procedure weights each transition per its uncertainty and

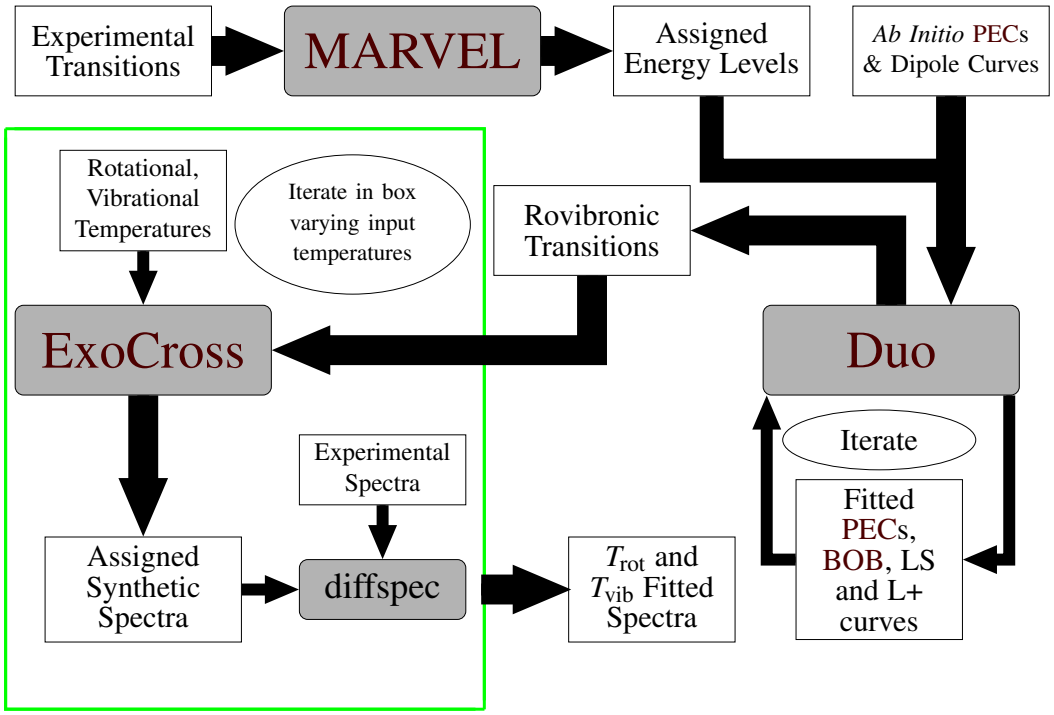

Figure 2.5: Flow diagram showing the production of high accuracy synthetic spectra, starting in the top left corner with collated experimental transitions and resulting in, bottom centre, synthetic spectra with the best fit rotational and vibrational temperatures.

produces multiple spectroscopic networks if there aren't transitions to join each energy level to others through at least one path. This is commonly the case if there are ortho- and para-states or spin splitting between which transitions are forbidden.

These transitions are run through the program and various unlinked spectroscopic networks of energy levels are generated. Separate networks can be joined with "linking" transitions, e.g. joining the degenerate spin up and spin down states of the ground state with a transition of zero energy from one degenerate state to another. This linking transition is an artificial transition whose energy, sometime called a "magic" wavenumber, may be calculated from empirical, effective Hamiltonian energy levels belonging to separate networks or, as in this work taken to produce the correct degeneracy between two levels in separate networks. The result of this process is to give a set of empirical energy levels with quantum number assignments.

The "good" quantum numbers in this application are the total rotational quan-

tum number (J) and total parity (+ or -). Quantum numbers of operators not strictly conserved in this application can still be used in state assignment. They are electronic state, vibrational quantum number (v), nuclear rotational angular momentum (N), projection of total spin angular momentum (Σ), projection of total orbital angular momentum (Λ), and the projection of total electronic angular momentum $\Omega = \Lambda + \Sigma$. This places our representation in Hund's case b (Huber and Herzberg 1979, Bernath 2005).

2.3.2 Duo

Duo (Yurchenko et al. 2016) is a fully-coupled rovibronic nuclear motion code which generates rovibronic energy levels and wavefunctions for diatomic molecules from potential energy curve (PEC)s, couplings between PECs, and Born-Oppenheimer breakdown terms. This program contains an iterative fitting procedure where PECs and other terms can be fitted to experimental, or empirical data. Additions were made to the program Duo by myself to include the potential form given in equation 2.1.16.

The iterative fitting procedure allowed the ground and first excited state PECs to be modified by the fitting of adiabatic and non–adiabatic Born-Oppenheimer breakdown (BOB) curves as given in equations 2.1.23 and 2.1.22 (Le Roy 2017) using the BeD and BeT isotopologue energy level data from MARVEL. Using BOB correction terms makes these data applicable to all isotopologues of BeH through providing an accurate scaling with atomic masses of the small scale changes in the molecular structure. This allows data from all three isotopologues to improve the fit from the same set of PECs and coupling terms.

2.3.3 Exocross

The final step in generating an assigned synthetic spectra is performed using a program called ExoCross (Yurchenko et al. 2018). ExoCross produces cross-sections for the absorption or emission of photons by molecules. It was modified by myself to use rotational, vibrational and electronic temperatures to produce a statistical (Boltzmann) population model for emission spectra. The equation for the popula-

tion of a state: $P_{e,v,J}$ where $e =$ electronic state, $v =$ vibrational quanta, and $J =$ total angular momentum quantum number is

$$P_{e,v,J} = e^{-\frac{(E_{e,v,J}-E_{e,v,J=0})}{kT_{\text{rot}}}} e^{-\frac{(E_{e,v,J=0}-E_{e,v=0,J=0})}{kT_{\text{vib}}}} e^{-\frac{E_{e,v=0,J=0}}{kT_{\text{ele}}}}, \tag{2.3.1}$$

where the temperature dependence is split into three exponentials with exponents relating to the rotational, vibrational and electronic state temperatures respectively. The first term is a function of the rotational temperature, T_{rot}, and pure rotational energy, $(E_{e,v,J} - E_{e,v,J=0})$, the second the vibrational temperature, T_{vib}, and pure vibrational energy, $(E_{e,v,J=0} - E_{e,v=0,J=0})$, and the third the electronic state temperature, T_{ele}, and the pure electronic state energy, $E_{e,v=0,J=0}$.

Einstein A-values, here provided by Duo, along with the populations are used to generate transition intensities, $I_{e'',v'',J'',e',v',J'}$. ExoCross then uses line positions, also from Duo, and the width of the comparison spectrometer's instrument function to generate Gaussians with areas equal to the calculated transition intensities. These are then summed to give the emitted intensity profile.

In taking different rotational, vibrational and electronic temperatures ExoCross allows us to more accurately fit non– LTE spectra. This procedure is useful in the case where LTE has not been reached by the molecule producing the spectra. In such an instance the different spacing between electronic, vibrational, and rotational energy levels means that they adapt to changing temperatures and plasma conditions at different rates.

2.3.4 Program: diffspec

The program diffspec was written by myself to quantify the fit of a theoretical spectrum to an experimental spectrum. The fit is given a quality index which takes into account only the relative shapes of the spectra and not the absolute value of either as it is intended to be used at a stage before calibration between theory and experiment has been fixed; indeed it can provide a method of fixing it after a full fitting has been achieved.

The program is run many times while looping over a range of temperatures

at which the theoretical spectrum is produced, potentially varying vibrational and rotational temperatures separately or making any other changes to the theoretical spectrum with each iteration of the loop. This part of the process is shown in the green box in figure 2.5. For each iteration diffspec compares the theoretical spectrum to the experimental spectrum by integrating the area under both curves, finding the overlap, and integrating the area between the curves, finding the difference. The metric minimised to find the best fit temperature is the difference divided by the overlap.

The theoretical and experimental spectra are both normalised, in the first instance, to have Q-branch peak values of 1.0. A multiplicative factor is then required to allow the peak values to differ. The experimental spectrum may also contain a background intensity which must be removed before matching to the theoretical spectrum. This necessitates a threshold being placed on the experimental spectrum. Also a higher weighting should be placed on fitting to the more intense parts of the experimental spectrum, since these have the smallest experimental uncertainties in measurement. To this end, there are three inputs which adjust the intensity to control the nature of the fitting: factors, background thresholds and weight. The factors are applied to the synthetic spectrum by multiplying the intensity by a series of factors allowing the normalised spectra of arbitrary intensities to have different maximum values with respect to one another. For each factor, background thresholds are applied to the experimental spectrum, adding or subtracting each threshold so as to account for the background in the experimental spectrum as indicated by the quality index. The last control input is a weight, allowing a higher weighting to be given to the higher intensity portions of the spectrum for both the difference and the overlap. This is achieved by weighting each intensity by a power. Usually a weighting of 2.0 was used effectively, squaring the area, ensuring a sensible relation between the uncertainty in an intensity measurement and the magnitude of that intensity. Finally diffspec can take input parameters instructing it to ignore certain regions of the spectra from the area summation, which is used in the case of invasive transitions from other species into the experimental spectra.

Chapter 3

Results

This chapter discusses the results from the various parts of this project. It is broken down into sections by the portion of the work.

There are four main sections to the results, the raw electron scattering data, the vibrational resolution of the R-matrix scattering data, the theoretical spectroscopic model produced, and the comparison to experimental spectra. The electron scattering data is produced using UKRMol/UKRMol+, detailed results being given for the equilibrium geometry results which are also compared to previous literature and an overview is given for the multi–geometry results. The vibrationally resolved scattering results are shown and a comparison in words to the vibrational resolution of R-matrix scattering results given by Celiberto et al. (2012b) is included.

The spectroscopic models for BeH, BeD and BeT are explained in detail and results for comparisons to experimental transitions are given. The experimental work is outlined and the recording of spectra on JET by myself as part this project is highlighted. This experimental spectra is compared to the theoretical spectra produced by the spectroscopic model provided in this work and a prediction of spectra that could be observed in future tritium campaigns on JET or ITER is given.

3.1 R-Matrix

3.1.1 Equilibrium Geometry

3.1.1.1 Target Model Comparisons

The target model selection was based upon the premise of getting the most accurate target energies and dipole moments within the allowed computational and R-matrix radius constraints. To select the optimal model we tested the use of different atomic basis sets in combination with the FCI and FC-FCI methods. We also tested a smaller CAS-CI model in which the two core electrons on Be are frozen and three electrons occupy a smaller set of $8a_1$, $3b_1$, $3b_2$ and $1a_2$ molecular orbitals. Due to the factorial scaling of the CI methods the computational demands significantly increase when going from three (i.e. frozen core) to five (i.e. all) active electrons and from the double zeta (pVDZ) to triple zeta (pVTZ) basis sets.

While some tests were performed for our target wavefunctions over a range of bond-lengths, all calculations presented here were performed in the centre-of-mass frame at the experimental equilibrium bond-length of $R = 1.3426$ Å (Huber and Herzberg 1979). The target calculations were performed using Hartree-Fock orbitals generated using MolPro (Werner et al. 2012).

Table 3.1 shows the calculated ground state (GS) energy, in Hartree, vertical electronic excitation energies, in eV, and the dipole moments for the various models tested by us and in comparison with the high accuracy electronic structure calculations of Pitarch-Ruiz et al. (2007) and the available experimental values of adiabatic excitation energies. The state labels and the experimental values have been taken from Pitarch-Ruiz et al. (2007). We note that Pitarch-Ruiz et al. (2007) used a slightly different value for the bond length (1.326903 Å) in their single geometry calculations, but this difference has only a minimal effect on the calculated values. Nonetheless energies in Table 3.1 are taken from potential energy curves from Pitarch-Ruiz et al. (2008). According to Pitarch-Ruiz et al. (2007) the adiabatic nature of the experimental electronic excitation energies compared to the vertical nature of theoretical excitation energies is the most important factor explaining

Table 3.1: Ground state energy (in Hartree), vertical excitation energies (in eV), permanent dipole moment for the ground state (in a.u.) and the magnitudes of the transition dipole moments for the initial ground state (in a.u.) as calculated in this work and compared with reference experimental and theoretical values.

Ground state energy and excitation energies								
			CAS-CI	FCI	FC-FCI			
State	Experimental[a]	Literature[b]	cc-pVDZ	cc-pVDZ	cc-pVDZ	aug-cc-pVDZ	cc-pVTZ	aug-cc-pVTZ
X $^2\Sigma^+$		-15.194	-15.173	-15.189	-15.188	-15.190	-15.196	-15.197
1 (A) $^2\Pi$	2.48	2.500	2.481	2.554	2.557	2.524	2.519	2.500
2 $^2\Sigma^+$		5.539	5.614	5.690	5.695	5.530	5.696	5.521
3 (C) $^2\Sigma^+$	3.84	5.532	7.617	7.647	7.649	5.633	6.812	5.646
1 $^4\Pi$		5.770	5.609	5.796	5.799	5.753	5.852	5.821
4 $^2\Sigma^+$	6.06	6.107	8.989	9.055	9.054	6.233	7.202	6.226
2 (B) $^2\Pi$	6.31	6.313	7.472	7.582	7.592	6.435	7.564	6.465
5 $^2\Sigma^+$		6.706	10.059	10.221	10.227	7.450	9.077	7.219
3 (D?) $^2\Pi$	6.71	6.712	7.948	8.100	8.109	7.366	7.905	7.316
6 (E) $^2\Sigma^+$	6.71	7.019	10.876	10.992	10.998	7.645	10.391	7.420
4 (G) $^2\Pi$	7.28	7.352	9.860	9.933	9.936	7.814	8.434	7.766
1 (D?) $^2\Delta$	6.74	6.747	9.039	9.255	9.261	8.290	9.109	7.942
5 $^2\Pi$		7.266	13.468	13.632	13.636	8.576	12.147	8.165

Permanent Dipole Moment for the ground state							
		CAS-CI	FCI	FC-FCI			
State	Literature[b,c]	cc-pVDZ	cc-pVDZ	cc-pVDZ	aug-cc-pVDZ	cc-pVTZ	aug-cc-pVTZ
X $^2\Sigma^+$	0.065 (0.0561)	0.003	0.061	0.060	0.095	0.070	0.090

Transition Dipole Moments for the initial ground state							
		CAS-CI	FCI	FC-FCI			
State	Literature[b]	cc-pVDZ	cc-pVDZ	cc-pVDZ	aug-cc-pVDZ	cc-pVTZ	aug-cc-pVTZ
1 (A) $^2\Pi$	0.871	0.812	0.840	0.840	0.859	0.857	0.865
2 $^2\Sigma^+$	0.612	0.352	0.303	0.302	0.577	0.291	0.595
3 (C) $^2\Sigma^+$	0.188	1.051	1.077	1.078	0.207	0.051	0.101
4 $^2\Sigma^+$	0.594	0.772	0.732	0.729	0.369	1.152	0.443
2 (B) $^2\Pi$	0.390	0.819	0.917	0.917	0.212	0.879	0.246
5 $^2\Sigma^+$	0.757	0.525	0.560	0.563	1.327	1.003	1.380
3 (D?) $^2\Pi$	0.417	1.086	0.957	0.961	0.720	0.961	0.733
6 (E) $^2\Sigma^+$	0.207	0.466	0.430	0.428	0.540	0.051	0.109
4 (G) $^2\Pi$	0.307	0.251	0.244	0.240	1.015	0.135	0.979
5 $^2\Pi$	0.342	0.164	0.166	0.065	0.935	0.184	0.907

[a] Collected experimental adiabatic excitation energies taken from Pitarch-Ruiz et al. (2007). [b] Theoretical results of Pitarch-Ruiz et al. (2007) and Pitarch-Ruiz et al. (2008). [c] The value in braces is from calculations by Celiberto et al. (2012b)

the sometimes significant differences between their calculated and the experimental values, like the large difference between these values for the C-state. Excluding the C-state the agreement of their calculated data with experiment is very good and therefore in the following we use the calculated values of Pitarch-Ruiz et al. (2007) as an accurate reference for our calculations.

Comparing our results obtained using the cc-pVDZ basis set and the three different models for electron correlation, we observe only negligible differences between the FCI and the FC-FCI results for both the vertical excitation energies and the dipole moments. We conclude that the frozen core approximation leads to an

insignificant loss of accuracy, especially for the low-lying states, compared to the five-electron FCI calculation, despite a very significant reduction in computational cost. The differences between the FC-FCI model and the CAS-CI model are mostly small but non-negligible making the FC-FCI model preferable.

The vertical excitation energies obtained using the FC-FCI (cc-pVDZ) model are in good agreement (within 0.2 eV) with the reference values only for the states 1 (A) $^2\Pi$, 2 $^2\Sigma^+$ and 1 $^4\Pi$ which are all valence states while most of the remaining states have a Rydberg character (Pitarch-Ruiz et al. 2007). These results suggest that the main deficiency of this model is the absence of diffuse functions in the atomic basis. Indeed, as seen from the Table the use of the cc-pVTZ basis which is larger than cc-pVDZ but does not include diffuse functions does not lead to a better agreement between ours and the reference values for the diffuse states. The agreement with the reference values is dramatically improved when the FC-FCI method together with the augmented (diffuse) basis sets is used: the agreement is excellent (within 0.12 eV) for the lowest six excited states. The differences between the aug-cc-pVDZ and aug-cc-pVTZ are mostly negligible but the FC-FCI model using the aug-cc-pVDZ basis is computationally significantly cheaper than the one using the aug-cc-pVTZ basis. We also tested the use of the aug-cc-pVQZ basis set (not shown) but found little improvement over the aug-cc-pVTZ results despite the increase in computational cost.

Table 3.1 includes the dipole transition moments between the ground state and the excited states and the value of the permanent dipole moment for the ground state obtained using the different target models. The comparison of the dipole transition moments for the FC-FCI (aug-cc-pVDZ) model with the reference values shows larger differences in comparison with the vertical energies but that is to be expected since dipole moments are generally the more sensitive property. Nevertheless, the agreement with the reference values for the first six states is still good. We conclude that the FC-FCI model using the aug-cc-pVDZ atomic basis is optimal in terms of accuracy and computational cost. This will be our preferred model for use in the scattering calculations.

3.1.1.2 Scattering models for GTO-only UKRMol calculations

The calculations using the GTO-only representation of the continuum were performed using the UKRMol suite (Carr et al. 2012). We found that the scattering calculations using our preferred target model FC-FCI (aug-cc-pVDZ) were not possible due to the limits on the size of the R-matrix sphere and the diffuse character of the target states resp. target orbitals. To avoid these problems we have used the compact cc-pVDZ atomic basis set and R-matrix radius $a = 14$ Bohr. The exponents of the continuum GTOs were optimised according to the methods of Faure et al. (2002) and a largest angular momentum for the continuum electron of $l = 4$. The deletion threshold used in the symmetric orthogonalization was set to 2×10^{-7}.

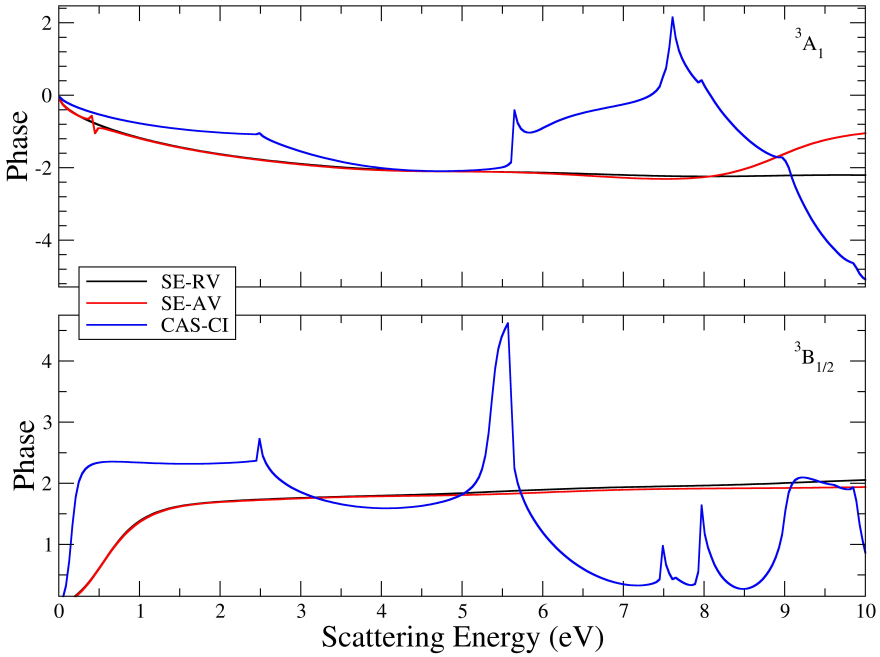

Figure 3.1: Eigenphase sums for the $^3A_1$ and $^3B_{1/2}$ symmetry calculated using UKRMol and various scattering models: static exchange using all virtuals (SE-AV), static exchange using a reduced set of virtuals (SE-RV) and complete active space CI (CAS-CI).

We have found that even with the compact atomic basis we could not include all target molecular orbitals in the calculation: some virtual orbitals were too spatially extended to be contained within the R-matrix sphere. To illustrate this point we

show in Figure 3.1 eigenphase sums for the $^3A_1$ and $^3B_{1/2}$ scattering symmetries obtained from three different models: the static exchange model using all virtuals (SE-AV), the static exchange model using a reduced set of virtuals (SE-RV) and the CAS-CI model using the reduced set of virtuals and all 21 target states lying below 11 eV (CAS-CI). The SE calculations are not able to describe electronically inelastic processes and therefore have only a limited validity for electron energies larger than the threshold for the first electronically excited state ($\approx$ 2.5 eV). The CAS-CI calculations are reliable up to the ionisation threshold ($\approx$ 8.2 eV); the results beyond this energy must be interpreted with care.

The calculations using the SE-AV model included the HF wavefunction to represent the ground state of the molecule and all virtual orbitals available ($10a_1$, $4b_1$, $4b_2$ and $1a_2$) coupled to it to represent the L^2 functions in the scattering model (see Equation (2.2.1) above). The eigenphase sum for the SE models $^3B_{1/2}$ symmetry displays a broad jump around 5 eV which is a signature of a shape resonance - the only type of resonance the SE model can represent. In the CAS model this same $^3B_{1/2}$ resonance appears much lower in energy, around 0.2 eV, due to a more accurate representation of the BeH^- states. The eigenphase sum for the SE-AV model $^3A_1$ symmetry displays a sharp jump around 0.5 eV and a broader one around 9 eV. In the SE-RV model the number of virtual orbitals used is decreased to $8a_1$, $3b_1$, $3b_2$ and $1a_2$ and both of the resonance structures in the $^3A_1$ disappear, confirming they are unphysical. This problem is typical for calculations in which some of the target orbitals are not fully contained by the R-matrix sphere. Increasing the size of the R-matrix sphere beyond 14 Bohr is possible but only at the expense of reducing the energy range for the scattering electron. For the present case of $a = 14$ Bohr the continuum basis set is accurate up to scattering energy of approximately 15 eV but increasing the radius to 16 Bohr makes the valid energy range drop to below 10 eV. To the best of our knowledge the largest radius used in any GTO-based R-matrix scattering calculation was the calculation of Tarana et al. (2009) on Li_2 where a radius of 22 Bohr was used but the electron energy range was limited to energies below approx. 2.5 eV.

The results for the CAS-CI model using the reduced set of virtuals and 21 target states represent the highest-level results obtained in this work using the UKRMol code. The eigenphase sums for this model clearly show a number of resonances which we further discuss below. Here we only note the importance of modelling polarisation/correlation for and accurate description of the lowest-lying resonance in the $^3B_{1/2}$ symmetry which appears much lower in energy and has a smaller width in the CAS-CI results compared with the SE-AV results.

Although a CAS-CI calculation with the cc-pVTZ atomic basis is computationally tractable it has worse issues with linear dependence and functions leaking outside of the sphere. The increase in accuracy potentially achievable from the increase from cc-pVDZ to cc-pVTZ, as discussed in the preceding section, is also not significant in comparison to the increase in computational cost.

3.1.1.3 Scattering models for GTO/BTO UKRMol+ calculations

The calculations performed using UKRMol+ and the mixed GTO/BTO basis for the continuum were not limited by the size of the R-matrix sphere, a crucial advantage over UKRMol. Here we present only the results obtained using the preferred model FC-FCI (aug-cc-pVDZ) but calculations were performed using the simpler UKRMol models to verify the correctness of the new code. The close-coupling calculations included all electronic states below 12 eV, 50 states in total. We found that to confine them sufficiently a large radius of 35 Bohr is needed. This was achieved using a mixed basis for the continuum comprising a small set of continuum GTOs with exponents shown in Table 3.2 and a basis of BTOs built from a basis of radial B-splines spanning the radial range from $a_{GTO} = 3.5$ Bohr to the R-matrix sphere. Continuum angular momenta up to $l = 6$ were included in the calculation. The basis of continuum GTOs was optimised using NUMCBAS and GTOBAS (Faure et al. 2002) for a small radius of 4 Bohr. The basis of radial B-splines comprised 20 functions of order 9 but the first two had to be removed from the calculation since they do not have smooth first derivatives at the starting point $r = 3.5$ Bohr. Figure 3.2 shows the continuum GTOs and BTOs selected for use in this scattering model normalised as they are for use in the calculation by the scatci_integrals pro-

gram. Since the linear dependency problems are mitigated when BTOs are used the deletion threshold for orthogonalization was set to 10^{-5}, a value much larger than in the UKRMol calculations, while removing only a few continuum orbitals per symmetry from the basis. With these parameters the continuum basis was accurate for electron energies up to approx. 15 eV. Table 3.3 shows a summary of the issues with the trialed target and scattering models.

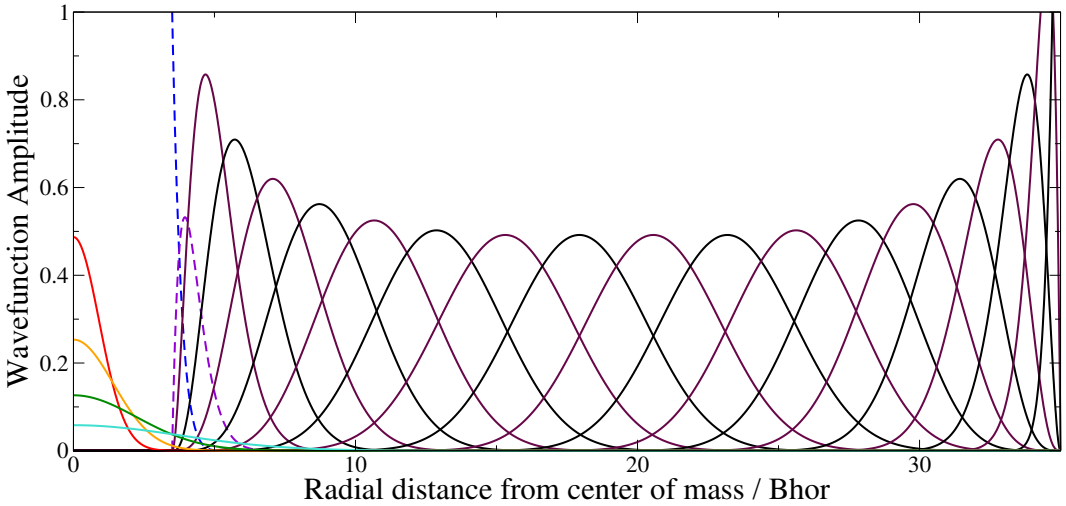

Figure 3.2: The continuum GTOs optimised for a sphere of 3.5 Bohr are shown centred on $R = 0$ and are coloured from red to cyan. The continuum BTOs optimised for a sphere of 35 Bohr are shown in black and maroon. In dashed blue and violet are the BTO discarded for being discontinuous in the function and first derivative respectively.

Table 3.2: Exponents of the continuum GTOs for partial waves up to $l = 6$ optimized for radius of 4 Bohr.

l	Exponents			
0	0.6018850	0.2517630	0.0997470	0.0355189
1	0.6279660	0.3026600	0.1392060	0.0575246
2	0.4300720	0.2046800	0.0891347	
3	0.4744870	0.2373500	0.1088240	
4	0.3118840	0.1353390		
5	0.3484640	0.1577080		
6	0.3847250	0.1798360		

Table 3.3: Comparison of issues with scattering results for various models and basis sets calculated with UKRMol and UKRMol+.

Model	**S**cattering Wave-function	**T**arget Model	**U**KRMol Comments	**U**KRMol+ Comments
SE	Reduced virtual	{HF cc-pVDZ	{HF target model, well behaved.}	{Unchanged.}
		HF aug-cc-pVDZ		
		HF cc-pVTZ}		
	All virtual	{HF cc-pVDZ	{HF target model, functions outside box, linear dependence and spurious resonances.}	{HF target model, box size and linear dependence issues removed.}
		HF aug-cc-pVDZ		
		HF cc-pVTZ}		
SEP	Converged virtual	HF cc-pVTZ	{HF target model and only limited resonances found.}	{Unchanged.}
CC CAS-CI	{Converged virtual, frozen core}	CAS-CI cc-pVDZ	{Poor target model.}	{Unchanged.}
		CAS-CI aug-cc-pVDZ	{Functions outside box.}	{Box size issues removed.}
		CAS-CI cc-pVTZ	{Poor target model.}	{Unchanged.}
CC FC-FCI	{All virtual,	FC-FCI cc-pVDZ	{Poor target model and linear dependence.}	{Poor target model, linear dependence issues removed.}
	frozen core}	FC-FCI aug-cc-pVDZ	{Accurate target model, functions outside box and linear dependence.}	{Accurate target model, box size and linear dependence issues removed.}
		FC-FCI cc-pVTZ	{Poor target model, functions outside box, linear dependence and computationally untractable.}	{Poor target model and computationally untractable, box size and linear dependence issues removed.}
CC FCI	{All virtual,	FCI cc-pVDZ	{Poor target model and linear dependence.}	{Poor target model, linear dependence issues removed.}
	active core}	FCI aug-cc-pVDZ	{Accurate target model, functions outside box, linear dependence and computationally untractable.}	{Accurate target model, box size and linear dependence issues removed, severely computationally untractable.}
		FCI cc-pVTZ	{Poor target model and severely computationally untractable.}	{Unchanged.}

3.1.1.4 Scattering Results

In Figure 3.3 we show the elastic and total scattering cross sections for the ground electronic state. Results of several calculations are shown: the UKRMol calculations were performed using the CAS-CI (cc-pVDZ) model while the UKRMol+ calculations employed the FC-FCI (aug-cc-pVDZ) model. Since the BeH molecule has a permanent dipole moment the long range interaction of the dipole with the continuum electron causes a slow convergence of the partial wave expansion for the continuum wavefunction. We estimate the contribution of partial waves beyond $l = 4$ (UKRMol) and $l = 6$ (UKRMol+) using the Born correction for the rotating dipole as implemented in borncros Norcross and Padial (1982). The corresponding Born–corrected total and elastic cross sections are plotted using solid lines, the total Born correction including the elastic and inelastic Born corrections.

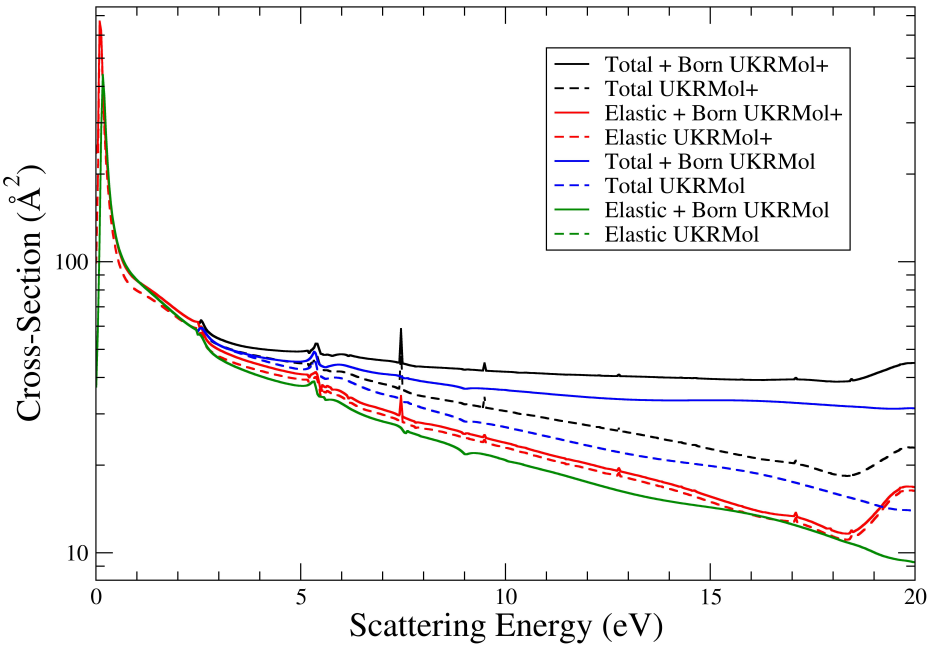

Figure 3.3: Total and elastic fixed geometry cross-sections for the ground state calculated using the UKRMol and UKRMol+ codes. The cross sections including the Born correction are plotted using solid lines.

Comparing first the elastic cross sections obtained using UKRMol (green) and UKRMol+ (red) we see that the latter is larger which can be explained mainly by the larger dipole moment of the ground state in the FC-FCI model (0.095 a.u.) compared with the CAS-CI value (0.003 a.u.). The small magnitude of the CAS-CI permanent dipole is also reflected in a very small contribution of the Born correction making the *ab initio* (dashed green line) and the Born-corrected cross sections (solid green line) indistinguishable in the plot. However, the UKRMol and UKRMol+ cross sections have a similar shape and show the same resonant peaks with the exception of a few narrow peaks appearing in the UKRMol+ results, discussed below.

The total cross sections (blue UKRMol, black UKRMol+) are much larger than the elastic ones for energies beyond the first excited state highlighting the importance of inelastic processes for electron collisions with BeH. We also observe the significant difference between the magnitudes of the UKRMol and UKRMol+ total cross sections at higher energies which is not explained by the difference in the elastic cross sections alone and points to the importance of using a highly accurate model to describe electronically inelastic processes.

Figure 3.4 gives a log plot of the cross-sections for electron impact electronic excitation from the ground state to the first six excited states. In solid lines are inelastic cross-sections including the Born correction calculated using the approach of Norcross and Padial (1982). The Born correction was calculated for all dipole allowed transitions from the ground state, i.e. excluding the spin-forbidden transition to the 1 $^4\Pi$ state. We can see that the Born correction makes a very significant contribution to the cross section for excitation of some of the states, e.g. the first excited state 1 (A) $^2\Pi$ and reflects the magnitudes of the corresponding transition dipole moments listed in Table 3.1.

Figure 3.5 compares our cross sections for impact excitation of the A-state with the one calculated by Celiberto et al. (2012a). The blue line is the R-matrix cross-section from Figure 3.5 of the paper by Celiberto et al. (2012a). The lines in black are results from the final model of UKRMol+ and in red are the results from the

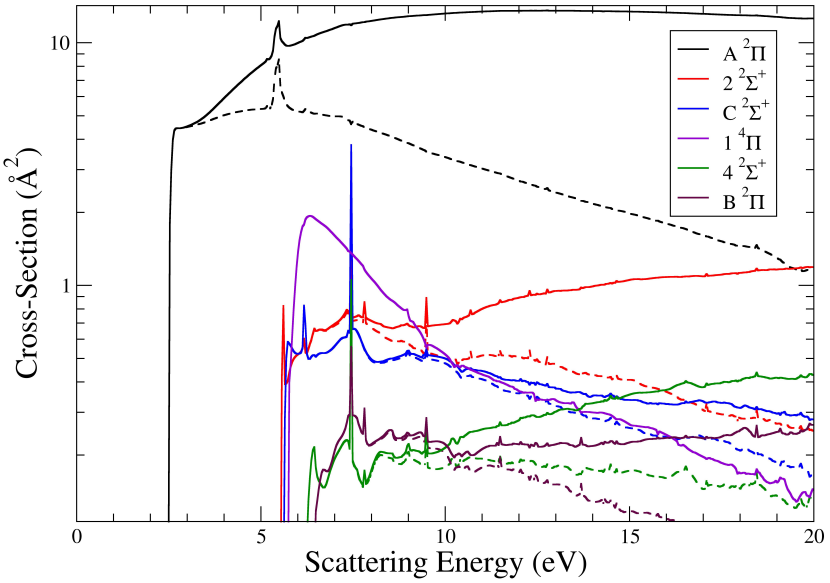

Figure 3.4: Electron impact electronic excitation cross-sections for the ground initial state (X $^2\Sigma^+$) and the six lowest lying final electronic states calculated using UKRMol+. The cross sections including (excluding) the Born correction are plotted in solid (dashed) lines.

final model of UKRMol. The results in dashed lines are without the Born correction and the solid lines are results with the Born correction added. We observe that above about 8 eV our uncorrected cross sections are significantly smaller than those of Celiberto et al. (2012a) and that the resonances in our calculations are found at lower energies and have smaller widths. This is consistent with our target and scattering models being larger and more accurate at describing polarisation/correlation effects.

Figure 3.5 also shows the importance of the Born correction: at 10 eV the Born-corrected results are approximately a factor of three to four larger than the corresponding uncorrected results. This finding can be put in contrast with the results of Celiberto et al. (2012a). Celiberto et al. (2012a) calculate the impact cross section in the Born approximation, which includes contributions of all partial waves, and compare it to their *ab initio* result which includes partial waves only

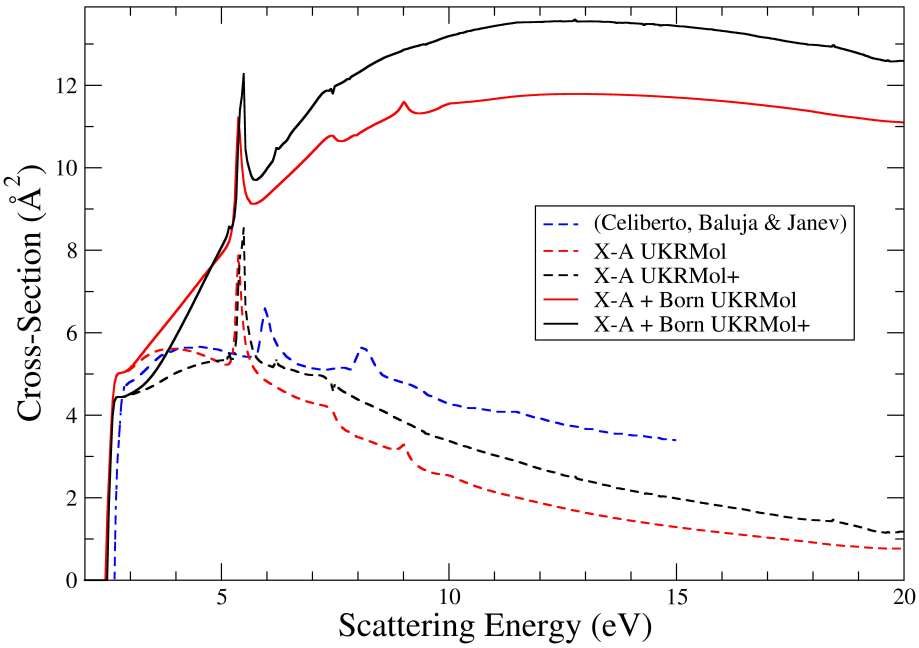

Figure 3.5: Comparison of electron impact electronic excitation cross-sections from the ground state, X $^2\Sigma^+$, to the lowest lying excited state, A $^2\Pi$. Solid lines are the cross sections including the Born correction. Dashed blue line is the R-Matrix result from literature Celiberto et al. (2012a).

up to $l = 4$ and to a result of the Modified Mott-Massey approximation (TM MM) scaled down to match the R-matrix result. The scaled TM MM results are then used to estimate the cross section for very large electron energies up to 1000 eV. However, since the Born correction is large scaling the TM MM result to a cross section not including it causes a significant underestimation of the TM MM results for the whole energy range.

Figure 3.6 shows sample differential cross sections, calculated using POLY-DCS (Sanna and Gianturco 1998) for scattering energies of 1.01 eV, 1.49 eV, 2.01 eV and 2.49 eV. As would be expected for a dipolar system, the cross sections are largest at 0^o, where the cross sections are all in the order of 10^6 Å^{2}sr^{-1} in comparison to the magnitude of 10^1 Å^{2}sr^{-1} at higher angles.

Electron resonances can influence cross sections for a range of processes in-

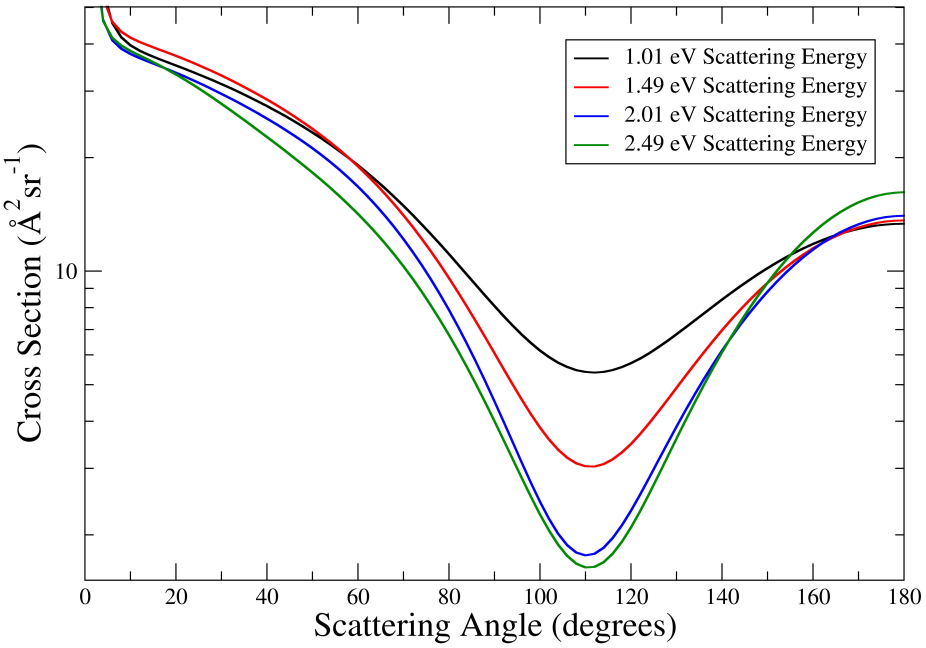

Figure 3.6: Differential cross sections of from the UKRMol+ final model. The peak values are 1.68×10^6 Å^{2}sr^{-1}, 3.01×10^6 Å^{2}sr^{-1}, 4.73×10^6 Å^{2}sr^{-1} and 6.52×10^6 Å^{2}sr^{-1} at scattering energies of 1.01 eV, 1.49 eV, 2.01 eV and 2.49 eV respectively.

cluding impact excitation. This can be seen, for example, in Figure 3.5 where the most prominent peak at around 5.2 eV is caused by a resonance. Table 3.4 collects the resonances and their parameters found in our results by fitting the eigenphase sums to the Breit-Wigner form. The Table compares the resonance parameters as obtained using the cc-pVDZ atomic basis and UKRMol suite with the results of the FC-FCI (aug-cc-pVDZ) model and UKRMol+ suite. We find a single narrow shape resonance of $^3\Pi$ symmetry close to the threshold. This is also the only resonance that can be described by the SE (Hartree-Fock) model. We have used the static exchange plus polarisation (SEP) method (not shown) to see if more shape resonances are present but no additional resonances are found. The close-coupling models reveal the formation of a number of resonances of core-excited character.

The parent state, 1 (A) $^2\Pi$, with the SCF configuration $1\sigma^2 2\sigma^2 1\pi$ might be ex-

pected to support three resonances with the configuration $1\sigma^2 2\sigma^2 1\pi^2$. Resonances with $^1\Delta$ symmetry at $\approx$ 2.6 eV, and $^1\Sigma^+$ symmetry at $\approx$ 5.2 eV can clearly be seen. However the expected, lower-lying resonance of $^3\Sigma^-$ symmetry is not observed. This is because this state lies below the 1 (A) $^2\Pi$ target parent state, and there is no allowed decay route to the GS. The $^3\Sigma^-$ state therefore forms a bound state in the continuum or a resonance with infinitesimal width (Stillinger and Herrick 1975).

The most prominent resonance from Figure 3.5, the $^3\Pi$ at $\approx$ 5.5 eV, lies about 8% lower in energy in our work from UKRMol than in the work of Celiberto et al. (2012a). There is also an uncertainty between our UKRMol and UKRMol+ models of about 2% for the position of this resonance and an average difference in the position of resonances of $\pm$ 30meV.

Table 3.4: Resonances found using the various scattering models employing UKRMol (SE, SEP, CC CAS-CI) and UKRMol+ (CC FC-FCI). Resonance positions and widths (in brackets) are in eV. Tentative resonance classifications and associated configurations are also given.

	SE	**S**EP	**C**C CAS-CI	**C**C FC-FCI	**R**esonance classification	
$^3\Pi$	0.572 [0.909]	0.235 [0.204]	0.155 [0.126]	0.090 [0.092]	$[1\sigma^2 2\sigma^2 3\sigma^1 1\pi^1]$	Shape
$^1\Delta$			2.572 [0.352]	2.55 [0.2]^a	$[1\sigma^2 2\sigma^2 1\pi^2]$	Core excited
$^1\Sigma^+$			5.63 [0.05]^a	5.195 [0.024]	$[1\sigma^2 2\sigma^2 1\pi^2]$	Core excited
$^3\Sigma^+$			5.64 [0.04]^a	5.366 [0.008]	$[1\sigma^2 2\sigma^2 4\sigma^1 5\sigma^1]$	Feshbach
$^3\Pi$			5.364 [0.142]	5.487 [0.017]	$[1\sigma^2 2\sigma^2 1\pi^1 4\sigma^1]$	Feshbach
$^3\Sigma^-$			5.810 [0.943]	5.8 [0.9]^a	$[1\sigma^2 2\sigma^1 3\sigma^1 1\pi^2]$	Core excited

^{a} Estimated, not fitted.

3.1.2 Multi Geometry

In order to produce a full vibrational resolution model of the R-matrix data we need R-matrix data for a range of geometries. So the single geometry calculation from section 3.1.1 above is repeated, varying the internuclear separation in the calculation, which is done on the input to MolPro (see figure 2.1). The target and scattering models selected in the single geometry case are used in all the multi geometry calculations. The validity of the target model was checked prior to its confirmation in the single geometry case. Evidence for this is shown in the comparison of the PECs from the chosen target model to those from literature (Pitarch-Ruiz et al. 2008) and our own fitted PECs from Duo in figure 3.7.

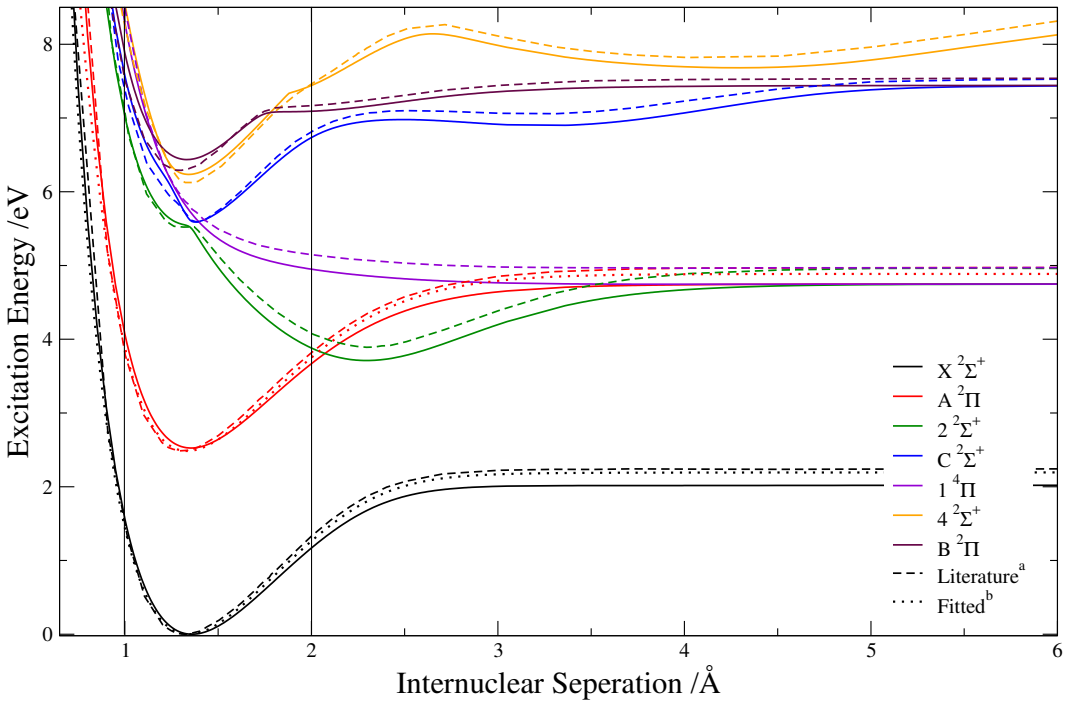

Figure 3.7: PEC comparison of the aug-ccpVDZ FC-FCI target model (solid lines) with those of Pitarch-Ruiz et al. (2008) ([a]dashed lines), and the fitted PECs of this work from Duo ([b]dotted lines). The various calculations are all zeroed at their respective GS minima as the comparisons of absolute energies is not of significance to this work. The two vertical black lines show the region in which the multi-geometry electron scattering calculations were used in the vibrational averaging model.

The main results of these multi–geometry calculations are scattering quantities, in the form of T-matrices, as a function of the internuclear separation. However as

T-matrices themselves are difficult to present in any medium, in figure 3.8 we display the GS, X $^2\Sigma^+$, to first excited state, A $^2\Pi$, electronic excitation cross section as a function of geometry and scattering energy. Cross-sections are calculated from T–matrices as given in equation 2.2.11. It can be seen in this figure that the energy position of the resonance feature, the spike, moves to a higher energy as the internuclear separation decreases, see figure 3.9 and the attached table. The position of this resonance depends on the energy of some state of the BeH^- anion formed temporarily during scattering and longer lived when a resonance is present. Due to the highly parallel nature of these two PECs, see Figure 3.7, the vertical excitation energy is almost constant over this energy range and thus the threshold, the starting scattering energy for the cross–section is almost constant.

One important observation here is that the individual calculations are separated by a broad enough gap in the internuclear separation such that the widths of the resonances do not overlap, i.e. at each geometry the resonance has moved by more than the resonance width away from its position at one geometry higher or lower. This is a potential source of complications for the vibrational averaging calculations, as it shows a non smoothly varying function in the T-matrix elements with geometry. This was unavoidable however as the computational expense of each geometry calculation limited the number of calculations that could be achieved in a reasonable time frame. This is further discussed when results from the vibrational averaging model are given below.

3.2 Vibrational Resolution

The results for vibrational resolution of the T-matrices are given in this section. However as the T-matrices themselves are difficult to represent and are not particularly physically meaningful here we present cross-sections for some of the various transitions. These vibrationally resolved cross-sections can be convoluted with Maxwell–Boltzmann energy distributions to give rates for the various transitions. The R-matrix scattering calculation was carried out up to a total scattering energy of 7.5 eV which relates to a different initial electron kinetic energy dependent on

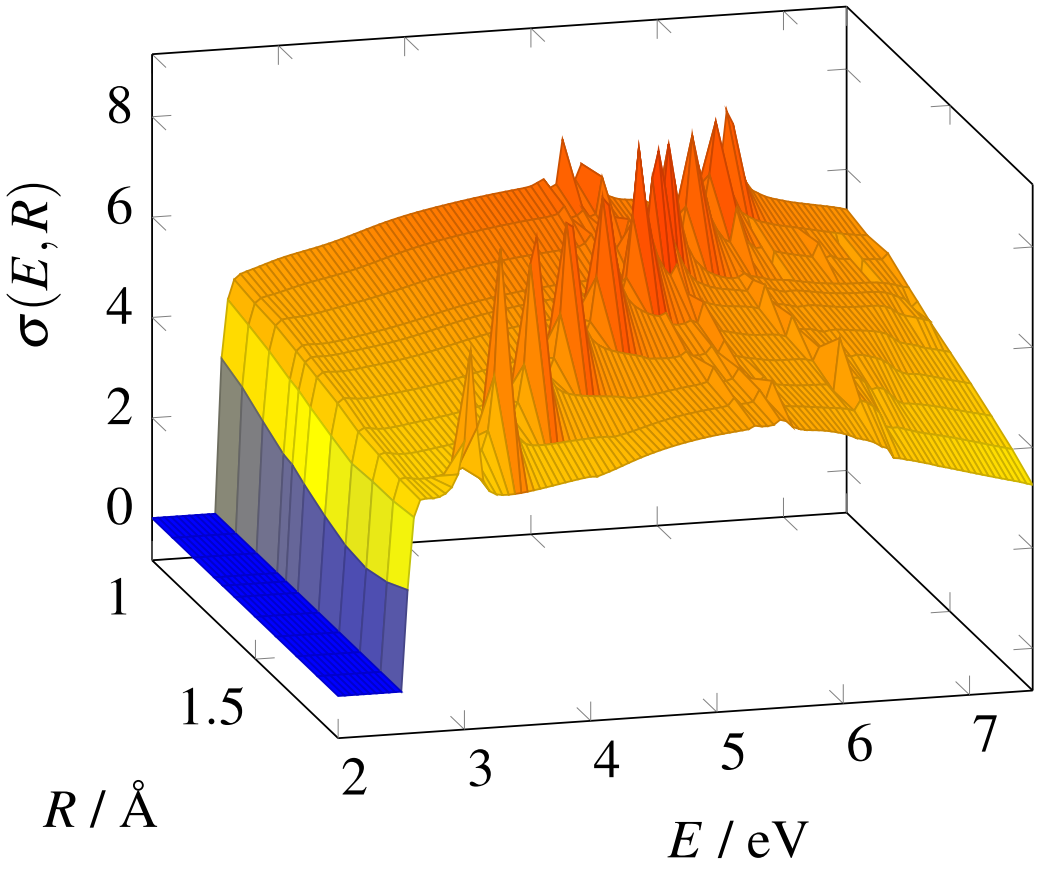

Figure 3.8: X - A cross sections, σ, as a function of the internuclear separation, R, and scattering energy, E. The main resonance can bee seen moving to lower energy with increasing internuclear separation.

the initial state of the target molecule.

The energy range of the cross-section has been extended by extrapolation using either a total Born cross-section or by the functional form of $\sigma(E_k) \propto \frac{1}{E_k}$. The extrapolated portion of the cross-section is scaled to the magnitude of the partial–Born + R-matrix cross-section just before it. The total Born extrapolation is used when the transition involves a significant dipole, otherwise the functional form extrapolation is applied. This results in a faster drop in cross-section area for the case where there is no significant dipole (see section 2.2.10) which is what would be expected. This extrapolation of the cross-section gives a more accurate evaluation of the rates as a function of the transition and electron temperature as it allows the high energy tail of the Maxwell–Boltzmann to be accounted for.

In the various cross–section figures in this section BeH, BeD, and BeT are

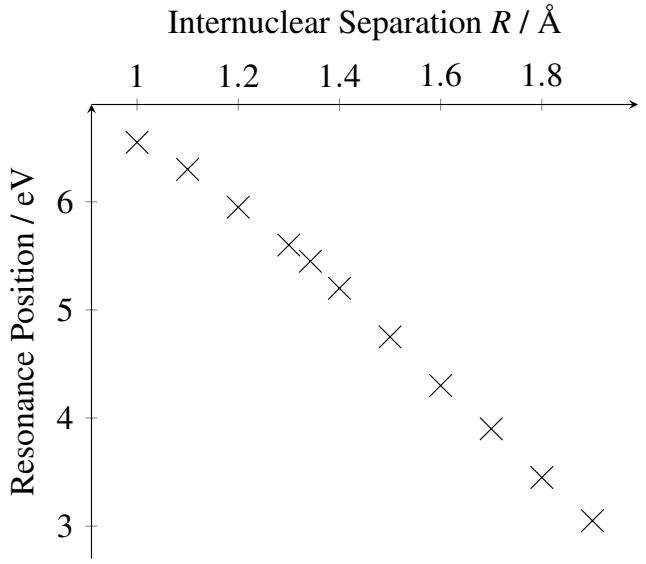

R / Å	Position / eV
1.0	6.55
1.1	6.3
1.2	5.95
1.3	5.6
1.3426	5.487[a]
1.4	5.2
1.5	4.75
1.6	4.3
1.7	3.9
1.8	3.45
1.9	3.05

Figure 3.9 & Table 3.5: The $^3\Pi$ resonance position as a function of geometry, this resonance being visible in the X–A cross-section in figure 3.8. For the equilibrium geometry, marked with ^{a}, the resonance position was fitted, for all other geometries the positions were estimated not fitted.

represented in solid, dashed and dotted lines respectively, and vibrational quanta are given in black, red, green, blue, orange, violet, cyan, magenta, indigo, maroon for $v = 0 \rightarrow 9$ respectively.

3.2.1 Quasi-Franck-Condon Factor Model

The quasi–FCF were obtained by application of the vibaver program (see section 2.2.9) to a single R-matrix calculation. This vibrationally averages T-matrices which are constant with geometry so vibrational averaging reduces to an application of $\left\langle \phi_{i'',v''}(R) \middle| \phi_{i',v'}(R) \right\rangle$ to the T-matrix channels which are squared when calculating cross-sections. This results in cross-sections with factors of $|\left\langle \phi_{i'',v''}(R) \middle| \phi_{i',v'}(R) \right\rangle|^2$ applied, which are the FCFs (see section 2.2.8.1 and equation 2.2.14).

One draw back to this method of vibrationally averaging single geometry results is that the X-X and A-A (electronically elastic) cross sections are non–zero only when $\Delta v = 0$. This is a direct result of the application +of FCFs. The resultant cross-sections are essentially just a factor times the equivalent electron cross-section, shifted to the correct threshold.

This can be seen in Figure 3.10 which shows cross-sections with the initial state X $v = 0$ to the final state X $v = 0$ or A $v = 0 - 2$. However as the FCFs are diagonal within a given electronic state there are no X $v > 0$ final states to show here. It is also noteworthy that the A $v = 1$ final state cross–section is significantly reduced in comparison to the A $v = 0$ final state cross-section which is contrasted with this result in the full geometry model below, see Figure 3.13.

As the FCFs are all equal to one within a given electronic state where $\Delta v = 0$ the various elastic X-X cross-sections with $\Delta v = 0$ are all equal to the X $v = 0$ to X $v = 0$ cross-section shown in the higher solid black line in Figure 3.10; this is also true for the various isotopologues. The various isotopologues are also degenerate on the X $v = 0$ to A $v = 0$ cross-section as these FCFs are all ≈ 1.

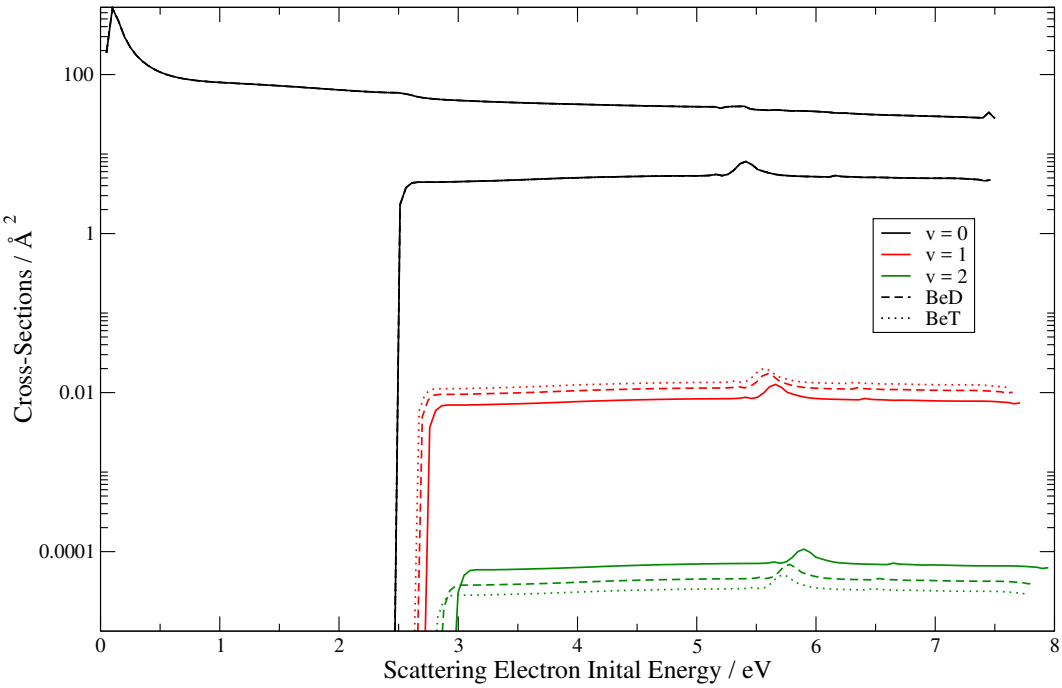

Figure 3.10: Vibronic cross–sections for the quasi–FCF, single geometry, model from initial state X $^2\Sigma^+$, $v = 0$ to the final states X $^2\Sigma^+$, $v = 0$ (higher black lines), A $^2\Pi$, $v = 0$ (lower black lines starting at ≈ 2.5 eV), and A $^2\Pi$, $v = 1 - 2$. Both sets of black lines are overlapped for the BeH, BeD and BeT results.

On the matter of comparison between our FCF results and those of Celiberto et al. (2012a) the curves given by their paper are a functional form fitted to the magnitude of the R-matrix cross-sections and as such they suffer from the same issue present in their single geometry results, a comparison for which is shown in figure

3.5. Here they have not applied the top up Born correction (see equation 2.2.20) to their R-matrix results and thus have omitted a major component of the cross–section resulting from the remaining partial waves in the expansion. This means that although their cross-sections compare well in terms of approximate magnitude when comparing to only the quasi–FCF R-matrix results, which ours are shown in figure 3.10, the comparison is unfavourable once the top up Born correction is applied. To see Born corrected results look at figures 3.14 and 3.15 below and for further comparison between the FCF model and the Born corrected results see figure 3.13 below.

3.2.2 Multi Geometry Data Model

The final set of results from this work are sets of vibronically resolved electron scattering cross-sections produced from vibrationally averaged multi-geometry T-matrices calculated using the R-matrix method. These may be used to calculate a complete set of rates for a collisional radiative model for a plasma environment and are available for BeH, BeD and BeT.

The assumption stated in the section 2.2.9 equation 2.2.19 that the PECs must be approximately parallel satisfactorily holds true for the X and A states of interest here. This can be seen in figure 3.7, where the shapes of the X (in black) and A (in red) curves can be seen to be largely the same with the A state being shifted up by ≈ 2.5 eV, at least within the region of interest (and in fact especially at higher geometries).

One major difference between these results and the results from the Quasi–FCF method is that this approach offers a complete set of cross-sections, including those between differing vibrational sates within a given electronic state, i.e. elastic scattering. This is shown in Figure 3.11 where the cross–sections for the transitions from the initial vibronic GS X $^2\Sigma^+$, $v = 0$ to states X $^2\Sigma^+$, $v = 1 - 3$ are given; in the FCF model these are all zero.

The vibrational averaging process also does not necessarily follow the same pattern as the FCFs, as shown in Figure 3.12. In this figure it can be seen that the largest cross-section is actually the $\Delta v = 1$ component (X, $v = 0$ to A, $v = 1$)

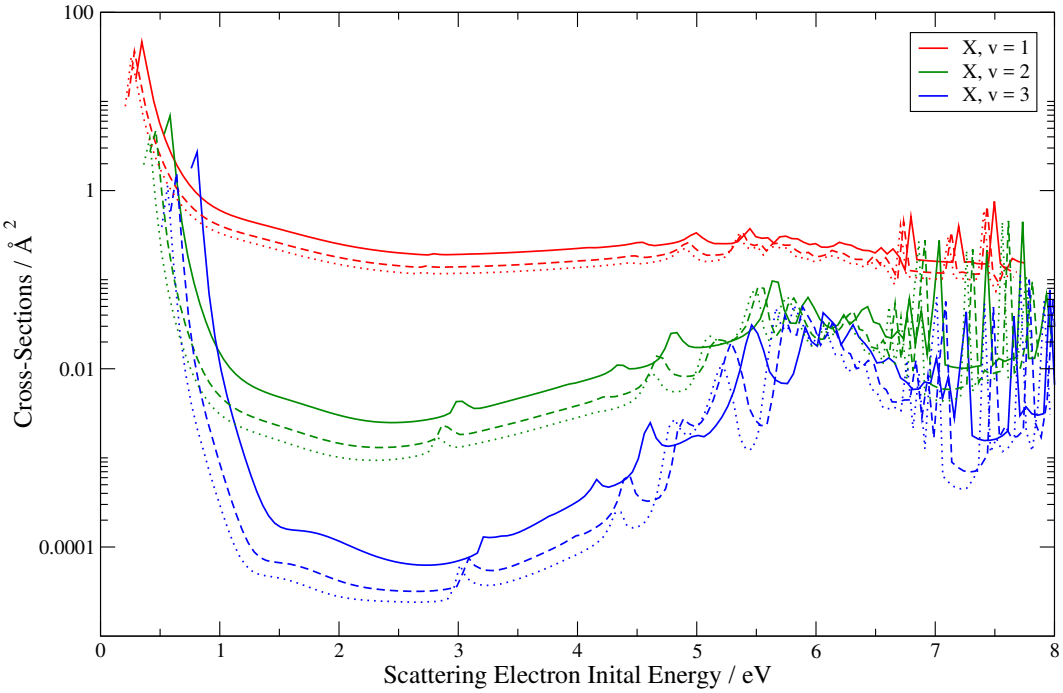

Figure 3.11: Vibronic transition cross–sections for the full vibrational averaging, multi–geometry, model from initial state X $^2\Sigma^+, v = 0$ to states X $^2\Sigma^+$, $v = 1 \rightarrow 3$. With BeH in solid, BeD in dashed, and BeT in dotted lines as shown in the legend.

and not the $\Delta v = 0$ component as the FCFs would suggest. This pattern is similar for other initial vibrational quanta of the X state to the A state where the $\Delta v = 1$ transition is actually the largest component. This is due to how to components of the T-matrix vary with geometry and how that matches up with the shape of the vibrational wavefunctions.

This marked difference between the FCF method and the vibrational averaging method in the off diagonal transitions where there is a change in electronic state and vibrational quanta, e.g. X, $v = 0$ to A, $v \neq 0$ is further demonstrated in Figure 3.13. The non–Born corrected versions for some these cross–sections are shown in figures 3.10 and 3.13, contrasting them shows the Born correction in these off diagonal components only makes a significant contribution to the much lower quasi-FCF cross-sections. This figure shows a direct comparison of some of these cross-sections from the FCF calculation and the vibaver calculation. The cross-sections in this figure are the Born corrected vibronic cross-sections with the extrapolation as applied by the borncros program and described in section 2.2.10.

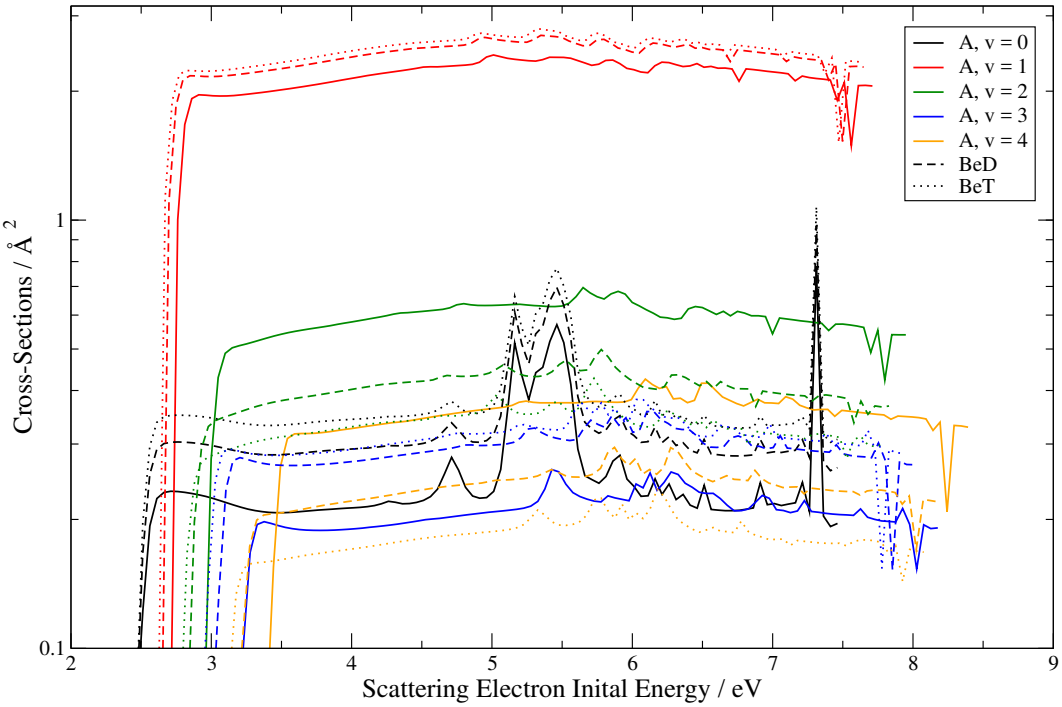

Figure 3.12: Vibronic cross–sections for the full vibrational averaging, multi geometry, model for the initial state X $^2\Sigma^+$, $v = 0$ and final states X $^2\Pi$, $v = 0 \rightarrow 4$ with BeH (solid lines), BeD(dashed lines), and BeT (dotted lines)as shown in the legend.

For the cross-sections shown, X, $v = 0$ to A, $v = 1 \rightarrow 3$, all of the vibrationally averaged results are significantly greater then the FCF results. The FCF results appear to show greater variation between the isotopologues. However this is mostly due to the Born correction being applied and the fact that it makes a more significant contribution to the smaller cross–sections. Also the Born correction being applied is almost the same in the FCF and the vibrational averaging models as it depends mostly on the dipoles from the Duo calculation.

This similarity between the quasi–FCF and multi–geometry vibrationally averaged results after application of the Born correction is shown most strongly in the vibronically elastic components where there are large dipoles. This makes the Born correction in these cases more significant to the cross–sections than the R-matrix results themselves. Vibronically elastic Born corrected results for BeH, and the full multi–geometry model (though there is insignificant difference in these elastic components for the single–geometry model) are shown in figure 3.14. The equiv-

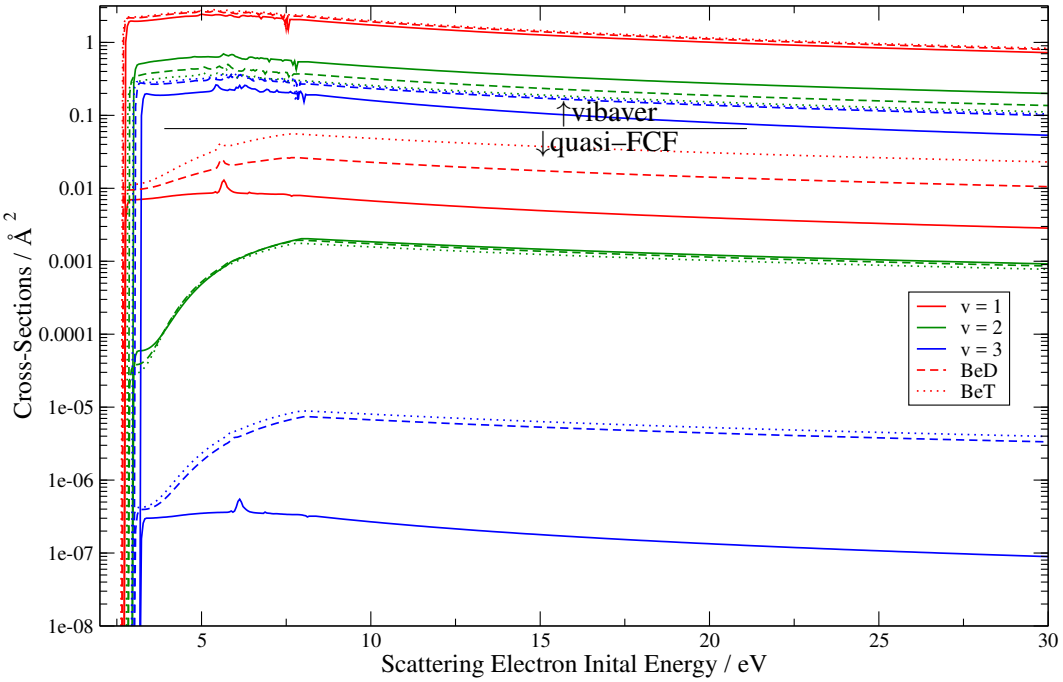

Figure 3.13: Born corrected vibronic cross–sections comparison with initial state X $^2\Sigma^+$, $v = 0$ and final states A $^2\Pi$, $v = 1 \rightarrow 3$ for BeH/D/T as shown in the legend. All the cross-sections which reach above the black dividing line labelled vibaver are from the vibrational averaging model and those below it are the quasi-FCF calculation results.

alent results for BeT are given in figure 3.15 to show in contrast the two extremes of the elastic cross–sections, with the BeD results falling predictably in between these two sets. The first thing to point out in these results is that the cross-section of the elastic X $^2\Sigma^+$ vibrational state curves increases with increasing vibrational quanta, the scattering is more likely for the higher vibrational states. In contrast, in the A $^2\Pi$ vibrational states this situation is reversed and the scattering is more likely for lower vibrational quanta. The second thing to point out here is the difference between BeT and BeH, where though the X states intensities do not change significantly the A states show an larger increases for higher vibrational quanta. As these cross–sections are dominated by the Born correction these effects are mostly the result of the vibrational dipoles from the Duo calculations. The cross-sections here are orders of magnitude greater than in the equilibrium geometry case due to the fact that the vibrational dipoles are much greater than the equilibrium geometry dipoles.

This is due to a similar effect that causes the features mentioned above where the $\Delta v = 1$ cross-sections are greater than the $\Delta v = 0$ cross-sections. Which is that the shape of the function and how it conforms with the vibrational functions effects the vibrational results. Here the electronic transition dipole crosses through zero close to equilibrium making the equilibrium dipole relatively weak in comparison to the vibrationally averaged dipole.

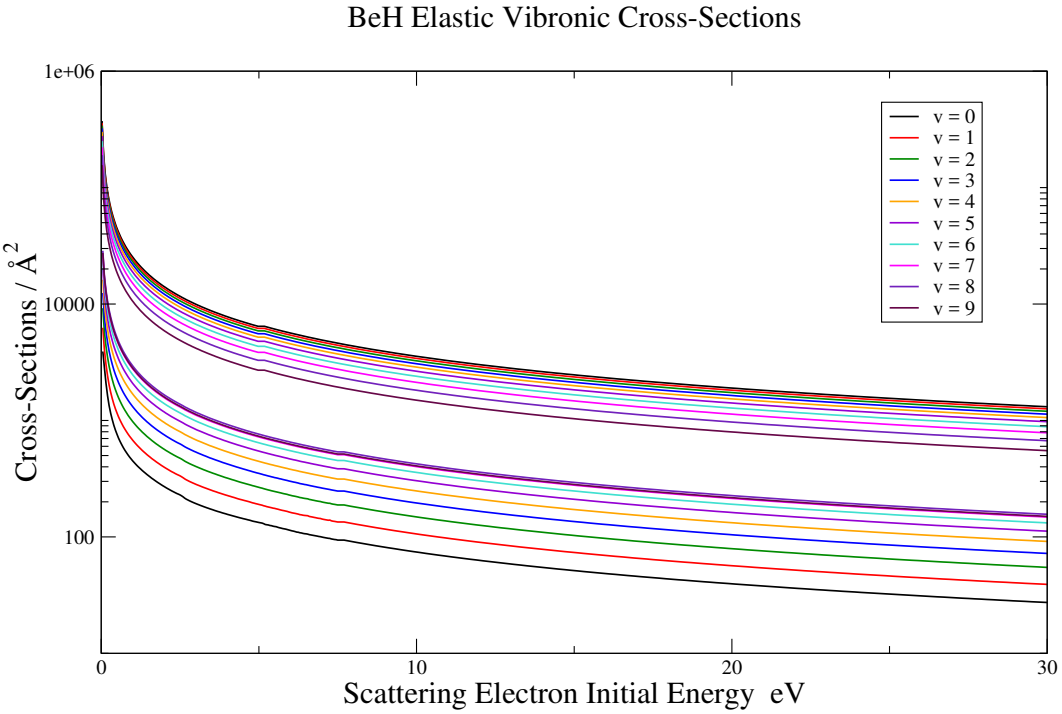

Figure 3.14: Elastic cross–section BeH states X $^2\Sigma^+$, $v = 0 \rightarrow 9$ (lower set of curves) and states A $^2\Pi$, $v = 0 \rightarrow 9$ (upper set of curves).

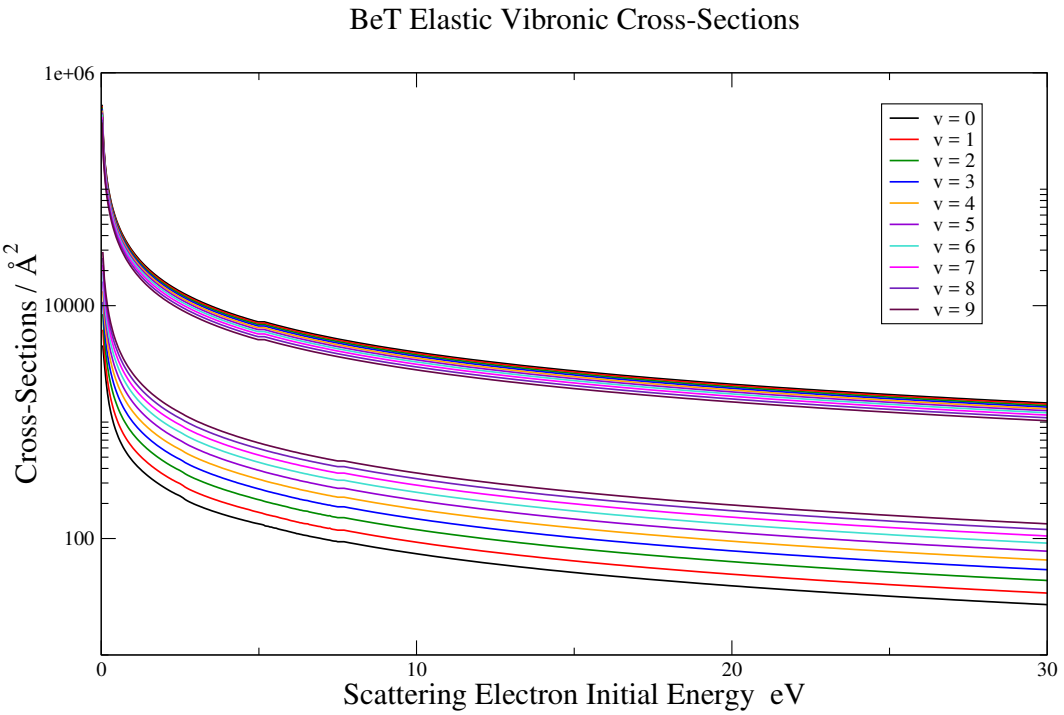

Figure 3.15: Elastic cross–section BeT states X $^2\Sigma^+$, $v = 0 \rightarrow 9$ (lower set of curves) and states A $^2\Pi$, $v = 0 \rightarrow 9$ (upper set of curves).

3.3 Spectral Modelling

3.3.1 MARVEL

My MARVEL analysis of BeH, BeD and BeT used transitions involving X $^2\Sigma^+$, A $^2\Pi$ and C $^2\Sigma^+$ states, with assigned quantum numbers taken from the literature (Le Roy et al. 2006, Shayesteh et al. 2003). In particular Le Roy et al. (2006) give transition data compiled from many sources including Shayesteh et al. (2003), Colin et al. (1983), Focsa et al. (1998) and De Greef and Colin (1974).

Table 3.6: Input transitions for MARVEL Online, in column A/V are the number of transitions all/validated. *See text for discussion on the comments

Isotope	Tag	Range (cm^{-1})	States	A/V	Largest Network	Comments
BeH						
	LeRoy.	15132-20822	A – X, C – X	1894/1886	1264	*H1
	Shay.	1802-2239	X – X	160/160		*H2
BeD						
	LeRoy.	15164-20619	A – X, C – X	2335/2276	1495	*D1
	Shay.	1240-1680	X – X	167/167		*D2
BeT						
	LeRoy.	19824-20424	A – X, $\Delta v = 0$ only.	534/524	215	*T1

Table 3.6 shows the transition data sources used for input to MARVEL. Comments on individual sources are as follows:

*H1 Le Roy et al. (2006) contains A – X transitions $\Delta v = 0$ up to $v'' = 6$, $\Delta v = +1$ up to $v'' = 6$ and some transitions for C – X with $v'' = 0 – 2$ and $v' = 6 – 10$.

*H2 Shayesteh et al. (2003) infrared, rovibrational transitions, were duplicated for $\Sigma = \pm 0.5$ giving 314 valid transitions.

*D1 Le Roy et al. (2006) contains A – X transitions $\Delta v = 0$ up to $v'' = 6$, $\Delta v = +1$ up to $v'' = 5$ and some transitions for C – X with $v'' = 0$ and $v' = 8 – 12$.

*D2 Shayesteh et al. (2003) infrared, rovibrational transitions, were duplicated for $\Sigma = \pm 0.5$ giving 328 valid transitions.

*T1 Le Roy et al. (2006) contains only A – X transitions $\Delta v = 0$.

Table 3.7: Table of MARVEL input transitions for BeH with column labels and explanations.

1	2	3	4	5	6	7	8	9	10	11	12	13
$\tilde{\nu}$	$\Delta\tilde{\nu}$	State$'$	v'	$(J'+\frac{1}{2})$	P'	Σ'	State$''$	v'	$(J''+\frac{1}{2})$	P''	Σ''	ID
20.3282	0.001	1	0	1	-	-0.5	1	0	1	+	0.5	MAGIC.001
15132.42	0.1	3	0	13	+	0.5	1	9	14	-	0.5	LeRoy.00001
15204.53	0.1	3	0	12	-	0.5	1	9	13	+	0.5	LeRoy.00002
15224.66	0.1	3	0	22	-	0.5	1	8	23	+	0.5	LeRoy.00003
15273.77	0.2	3	0	11	+	0.5	1	9	12	-	0.5	LeRoy.00004
15335.3	0.1	3	0	21	+	0.5	1	8	22	-	0.5	LeRoy.00005
15339.62	0.1	3	0	10	-	0.5	1	9	11	+	0.5	LeRoy.00006
15401.44	0.1	3	0	9	+	0.5	1	9	10	-	0.5	LeRoy.00007
15433.71	0.1	3	0	13	+	0.5	1	9	12	-	0.5	LeRoy.00008
15458.91	0.1	3	0	8	-	0.5	1	9	9	+	0.5	LeRoy.00009
15485.93	0.1	3	0	12	-	0.5	1	9	11	+	0.5	LeRoy.00010

Column	Notation	
1	$\tilde{\nu}$	Transition frequency (cm^{-1}).
2	$\Delta\tilde{\nu}$	Estimated uncertainty in transition frequency (cm^{-1}).
3	State$'$	Initial electronic state, 1 = X $^2\Sigma^+$, 2 = A $^2\Pi$, 3 = C $^2\Sigma^+$.
4	v'	Initial vibrational quantum number.
5	$(J'+\frac{1}{2})$	Initial total angular momentum quantum number plus 0.5.
6	P'	Initial parity quantum number.
7	Σ'	Initial electron angular momentum quantum number.
8	State$''$	Final electronic state, 1 = X $^2\Sigma^+$, 2 = A $^2\Pi$, 3 = C $^2\Sigma^+$.
9	v''	Final vibrational quantum number.
10	$(J''+\frac{1}{2})$	Final total angular momentum quantum number plus 0.5.
11	P''	Final parity quantum number.
12	Σ''	Final electron angular momentum quantum number.
13	ID	Unique ID for transition with source label and counting number.

A small portion of the MARVEL input file for BeH is shown in Table 3.7 where the column format is explained. The number of quantum numbers used for assignment here is 5. The thresholds for changing uncertainties and for deletion were both set to 3. The full files are given in the supplementary data for our paper (Darby-Lewis et al. 2018).

For BeH and BeD the infrared data of Shayesteh et al. (2003) brings together separate vibrational networks found in other data. This results in two large networks separated along the quantum number Σ, where Σ = -0.5 for one network and Σ = 0.5 for the other. These two networks are joined via a linking transition with a "magic" wavenumber, between states with opposing spin, as shown for BeH by the transition labelled MAGIC.001 in Table 3.7. This magic transition is an artificial transition calculated from empirical, effective Hamiltonian energy levels belonging

to separate networks (Furtenbacher et al. 2007). The frequency of the magic transition is calculated to produce degeneracy between the states with differing spin at low J.

Figure 3.16 shows the rovibrational energy levels of the largest component network for BeH, BeD and BeT. The almost straight lines with isotopologue-dependent gradients are vibrational bands and the gradients depend on the rotational constants ($\propto$ 1/reduced mass). Since the electronic states being represented here are doublets each point for an energy level shown in this figure actually corresponds to two spin degenerate states.

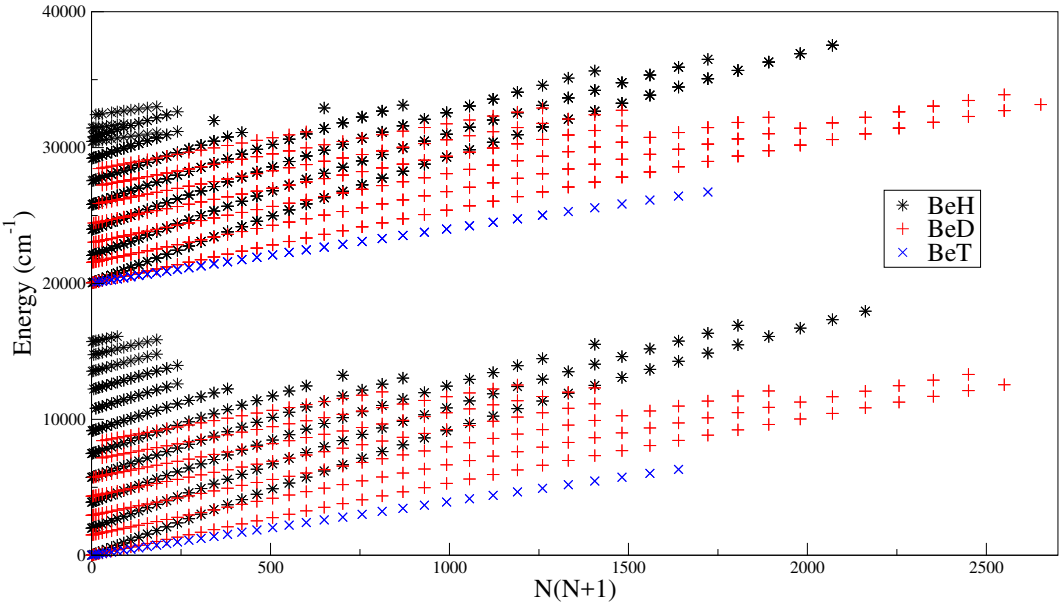

Figure 3.16: Output rovibronic energy levels from MARVEL for the largest spectroscopic networks of BeH, BeD, and BeT, against nuclear rotational quantum number, N, times nuclear rotational quantum number plus one. The rovibrational states of X $^2\Sigma^+$ are the lower set and the A $^2\Pi$ rovibrational states start at 20000 cm^{-1}. Each of the states represented here actually corresponds to two spin degenerate states as both the X and the A states are doublets.

3.3.2 Duo

Previous work has been done for BeH, BeD and BeT using both *ab initio* quantum chemistry (Yadin et al. 2012) and empirical fitting methods (Špirko 2016) to produce PECs (Dattani 2015). The iterative fitting procedure of the Duo code was used to refit the potential form of the GS PEC, a Morse long range (MLR) type potential

(Le Roy et al. 2011) as given by Pitarch-Ruiz et al. (2008), using energy levels output from MARVEL. A new PEC, of the extended Morse oscillator (EMO) type (Lee et al. 1999), is fitted to the A $^2\Pi$ excited state using energy levels output from MARVEL. The A $^2\Pi$ PEC is modified by the addition of a spin-orbit (LS) coupling curve and an X to A state L^+ (Λ–doubling) coupling curve. Both the ground and excited state PECs are modified by the fitting of adiabatic and non–adiabatic BOB curves (Le Roy 2017) using the BeD and BeT isotopologue energy level data from MARVEL. Using BOB correction terms makes these data applicable to all isotopologues of BeH. This allows data from all three isotopologues to improve the fit from the same set of PECs and coupling terms. The fitting of BOB terms is achieved using an iterative process in Duo. The non-adiabatic BOB term is an additive correction to the PEC which has an increasing effect with increasing isotope mass (from zero effect on H, to $\frac{1}{2}$ on D, to $\frac{2}{3}$ on T). However due to the limited data for BeT it is initially fitted to the BeD data and adjusted iteratively for BeT. The adiabatic BOB term is a multiplicative factor applied to the centrifugal potential and has greatest effect on the lighter isotope; it is therefore initially fitted to BeH and adjusted to model BeD and BeT. When a suitable fit is produced for both states using the available energy levels from MARVEL, Duo allows fittings to be performed using the transitions. This allows a larger set of data to be used in the fitting routine, as some of the energy levels output by MARVEL cannot be connected to the main spectroscopic network.

Tables 3.8 and 3.9 show some of the energy levels generated by Duo for BeH, BeD and BeT for both the X and A states, they are each followed by the energies from MARVEL used in the fitting for those levels. As shown earlier, in Table 3.6, only the $v = 0$ component of BeT joins the main network of transitions, as there are no measured $\Delta v \neq 0$ transitions for BeT. Overall the root mean square (RMS) of the fit for each isotopologue is: BeH, 0.542 cm^{-1}; BeD, 0.614 cm^{-1}; BeT, 0.384 cm^{-1}. PECs modified and fit by Duo for the X and A states of BeH, BeD and BeT are shown in figure 3.17. The Zero Point Energy (ZPE) of these curves are: 1022.0292 cm^{-1} for BeH; 742.7911 cm^{-1} for BeD; 626.2844 cm^{-1} for BeT. The Duo input

containing the PECs, couplings and BOB terms is given for BeH, BeD and BeT in the supplementary data for our paper Darby-Lewis et al. (2018). Predissociation is not included in this model.

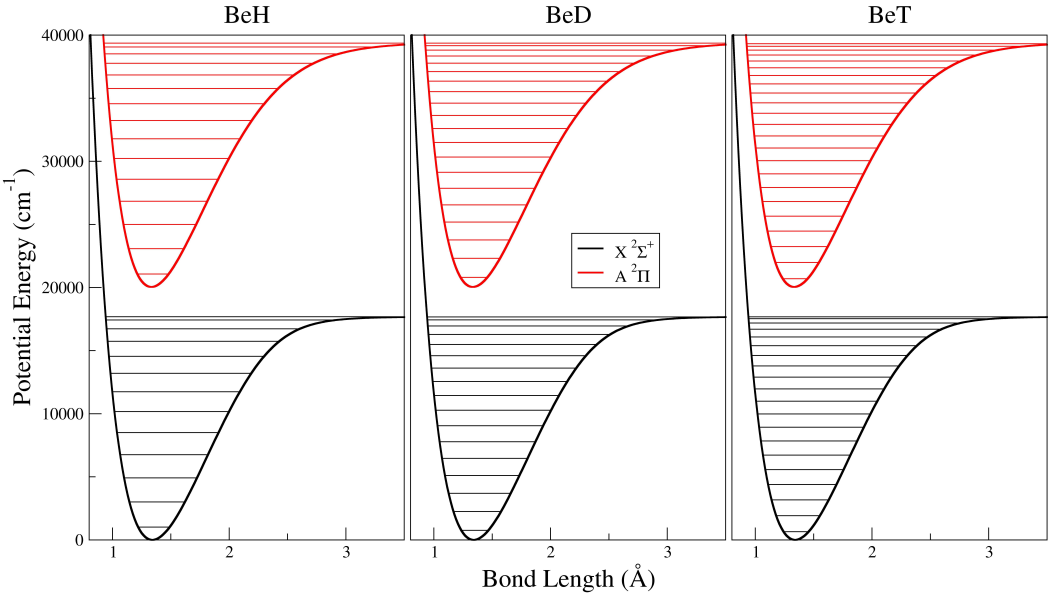

Figure 3.17: Fitted PECs for the X $^2\Sigma^+$ state and the A $^2\Pi$ state with vibrational energies at $J = 0.5$ for BeH, BeD, and BeT.

Fully fitted PECs, couplings and BOB terms are used in conjunction with an *ab initio* transition dipole curve (Pitarch-Ruiz et al. 2008) for the A to X state to generate Einstein A-coefficients for the rovibronic transitions. Duo outputs two files for the linelist of each isotopologue, one containing the list of the states involved in the transitions and the other being a list of the transitions between states and their A-values; this corresponds to the format of the ExoMol database (Tennyson et al. 2013, 2016). The start of the states file and the start of the trans file for BeH are shown respectively in Tables 3.10 and 3.11 followed by an explanation of their column formats. The entirety of the linelist in ExoMol format, states and trans files, for each isotopologue can be found in the supplementary data for our paper Darby-Lewis et al. (2018) and on the ExoMol website (www.exomol.com).

Table 3.8: Comparison of excitation energies as a function of vibrational quanta, v, computed with Duo and obtained by MARVEL for: BeH and BeD X $^2\Sigma^+$ at J=0.5, Ω = 0.5, parity = +; BeT X $^2\Sigma^+$ at J=2.5, Ω = 0.5, parity = -.

v	X $^2\Sigma$					
	BeH		BeD		BeT	
	Duo	MARVEL	Duo	MARVEL	Duo	MARVEL
0	0	0	0	0	49.2756	50.3
1	1986.3054	1986.4169	1488.4401	1488.8472	1323.9046	
2	3896.8004	3896.8707	2935.6045	2936.1953	2568.5846	
3	5729.2711	5729.2613	4340.7423	4341.3802	3782.8768	
4	7480.4545	7480.4219	5702.8860		4966.2478	
5	9145.4221		7020.7372		6118.0189	
6	10716.6777		8292.5346		7237.3131	
7	12182.7098		9515.8791		8322.9914	
8	13525.5493		10687.4899		9373.5704	
9	14716.2767		11802.8549		10387.1133	
10	15705.6510		12855.7188		11361.0802	
11	16402.4285		13837.299		12292.1239	
12	16664.9980		14735.0110		13175.8010	
13			15530.2285		14006.1479	
14			16194.0499		14775.0274	
15			16679.3277		15471.0599	
16			16918.4202		16077.7733	
17			16956.8145		16570.2919	
18					16910.3608	
19					17056.2519	
20					17076.5405	

3.4 Experimental Comparison

There were two original experimental spectra used in this work to show the agreement of the theoretical spectral model to experiment. The BeH spectrum was provided by co-authors on the paper Darby-Lewis et al. (2018), further details below, and the BeD spectrum was recorded by myself during time spent at JET. This comparison shows the ability of our spectral model not only in dealing with differing isotopologues but also in the accurate reproduction of spectra from very different plasma conditions; one, the BeD spectrum, is in a LTE like environment; two, the BeH spectrum, is very much in a non–LTE environment.

3.4.1 BeH Hollow Cathode Discharge Spectrum

Experimental BeH spectrum was supplied by a collaborator Sebastijan Brezinsek at Institut für Energie und Klimaforschung Plasmaphysik Forschungszentrum Jülich

Table 3.9: Comparison of excitation energies as a function of vibrational quanta, v, computed with Duo and obtained by MARVEL for: BeH and BeD A $^2\Pi^+$ at J=1.5, Ω = 0.5, parity = +; BeT A Π^+ at J=2.5, Ω = 0.5, parity = -.

v	A $^2\Pi$					
	BeH		BeD		BeT	
	Duo	MARVEL	Duo	MARVEL	Duo	MARVEL
0	20050.8587	20092.2658	20048.3803	20071.3872	20089.3230	20090.7
1	22056.7376	22097.0590	21552.7700	21575.8314	21378.1542	
2	23978.5785	24017.3355	23011.6534	23034.2030	22634.0613	
3	25813.4908	25850.6970	24423.8044	24445.6549	23856.2579	
4	27558.2734	27594.5151	25788.0151		25043.9940	
5	29208.9935	29243.2969	27102.9758		26196.4966	
6	30760.6586	30793.4022	28367.1779		27312.9196	
7	32206.9278		29578.8347		28392.3027	
8	33539.8057		30735.8129		29433.5357	
9	34749.2511		31835.5682		30435.3273	
10	35822.6125		32875.0780		31396.1765	
11	36743.7529		33850.7620		32314.3426	
12	37491.6119		34758.3833		33187.8099	
13	38037.6829		35592.9147		34014.2541	
14	38341.2611		36348.3556		34790.9884	
15			37017.4704		35514.9038	
16			37591.4032		36182.3870	
17			38059.0891		36789.2084	
18			38406.3136		37330.3688	
19			38614.1568		37799.8866	
20					38190.4670	
21					38493.0018	
22					38695.7499	
23					38779.4876	

GmbH Wilhelm-Johnen-Straße. This spectrum was recorded using a high resolution visible spectrometer, in cross-dispersion arrangement (grating and prism) covering the spectral range between 373 nm and 680 nm simultaneously in more than 50 orders with an almost constant resolving power of l/DL $\approx$ 20000, as show by Brezinsek et al. (2008). In the spectral range of interest the spectrometer's instrument function is $w \approx 1.5$ Å (≈ 0.6 cm^{-1}). The spectral source was a beryllium hollow-cathode discharge lamp with a neon/hydrogen mixture as a working gas. Inside the lamp, the metallic Be target plate is biased, resulting in it being bombarded by the impurity ions with Be being sputtered, either as Be or BeH$_X$. The current and voltage can be varied changing the plasma characteristics as well as the impact energy of the impinging ions. The released Be or BeH is then excited by

Table 3.10: Section of the states file produced by Duo for BeH with column format explanation.

1	2	3	4	5	6	7	8	9	10	11
n	E	m	J	$P_{+/-}$	$P_{e/f}$	State	v	Λ	Σ	Ω
1	0	16	0.5	+	e	X2Sigma+	0	0	0.5	0.5
2	1986.305446	16	0.5	+	e	X2Sigma+	1	0	0.5	0.5
3	3896.800417	16	0.5	+	e	X2Sigma+	2	0	0.5	0.5
4	5729.271094	16	0.5	+	e	X2Sigma+	3	0	0.5	0.5
5	7480.45445	16	0.5	+	e	X2Sigma+	4	0	0.5	0.5
6	9145.422113	16	0.5	+	e	X2Sigma+	5	0	0.5	0.5
7	10716.677675	16	0.5	+	e	X2Sigma+	6	0	0.5	0.5
8	12182.709789	16	0.5	+	e	X2Sigma+	7	0	0.5	0.5
9	13525.549349	16	0.5	+	e	X2Sigma+	8	0	0.5	0.5
10	14716.276652	16	0.5	+	e	X2Sigma+	9	0	0.5	0.5

Column	Notation	
1	n	Rovibronic counting number.
2	E	Energy of rovibronic state relative to ground state (cm^{-1}).
3	m	multiplicity, including nuclear spin degeneracy.
4	J	Total angular momentum quantum number.
5	$P_{+/-}$	Parity in +/- notation.
6	$P_{e/f}$	Parity in e/f notation.
7	State	Electronic state.
8	v	Vibrational quantum number.
9	Λ	Projection of electronic orbital angular momentum quantum number.
10	Σ	Projection of electron spin angular momentum quantum number.
11	Ω	Projection of total electronic angular momentum quantum number

Table 3.11: Section of the trans file produced by Duo for BeH with column format explanation.

1	2	3	4
n''	n'	A	$\tilde{\nu}$
71	1	4.58E-10	16933.174781
89	1	5.63E-02	38037.68383
65	1	8.17E-11	16699.528089
58	1	2.58E-07	12198.141744
95	1	6.48E-03	38492.659618
83	1	1.95E-01	32206.945906
51	1	1.12E-09	20.326390

Column	Notation	
1	n'	Initial rovibronic state number, see table 3.10
2	n''	Final rovibronic state number, see table 3.10
3	A	Eisenstein A-coefficient (s^{-1}).
4	$\tilde{\nu}$	Transition wavenumber (cm^{-1}).

electron impact leading to the emission of Be I, Be II as well as BeH light. Figure 3.18 shows the experimental spectrum of the BeH A – X transition as well as the best-fitting simulated spectrum. After fitting the experimental spectrum with an assigned synthetic spectrum we can rescale the whole thing to the absolute intensity of the cross-section from the theoretical calculation, allowing estimations of further parameters and inferences about the plasma conditions to be made.

3.4.2 BeD JET edge emission spectra

An experimental BeD A – X spectrum was measured in four consecutive (92493 - 92496) JET 2.4 T, 2.0 MA D discharges, figure 3.20a, with comparable conditions during the limiter phase (Fundamenski 2008) of the pulse at 4.7 – 5.1 s. During this time, the plasma was limited by the inner poloidal Be limiter and the interaction of the D plasma with the limiter led to the release of BeD molecules with the subsequent emission of BeD radiation from this region. This can be seen in the bottom trace of figure 3.20a which is very low around the time our spectra was being recorded, and goes to zero around ≈ 46 s. The four consecutive pulses were used to step through the spectral range of interest while maintaining similar plasma conditions and was necessary as the range of the high resolution spectrometer was approximately one quarter the range of the whole emission region of interest. The spectrum was recorded with a high resolution visible spectrometer (known locally as KS3), a 1 m Czerny-Turner configuration with a grating ruled with 1800 lines/mm (Czerny and Turner 1930), which directly observed the low density edge plasma close to the inner poloidal limiter along the LOS shown in figure 3.20b. In the spectral range of interest the spectrometer's instrument function is $w \approx 1.5$ Å (≈ 0.6 cm^{-1}). The four consecutive discharges were chosen to form a joined image, see figure 3.21, with comparable plasma conditions as well as assumed comparable rovibrational populations. After fitting the experimental spectrum with an assigned synthetic spectrum we can apply the same re-scaling, back to the absolute intensity of the theoretical spectrum, can be applied.

3.5 Spectral Analysis

The final step in generating an assigned synthetic spectra is performed using a program called ExoCross (Yurchenko et al. 2018). ExoCross produces cross-sections for the absorption or emission of photons by molecules. It uses rotational, vibrational and electronic temperatures to produce a statistical (Boltzmann) population model as given in equation 2.3.1

In taking different rotational, vibrational and electronic temperatures ExoCross allows us to more accurately fit non-LTE spectra. This procedure is useful in the case where LTE has not been reached by the molecule producing the spectra. In such an instance the different spacing between electronic, vibrational, and rotational energy levels means that they adapt to changing temperatures and plasma conditions at different rates. In the cases discussed here the necessary time to reach equilibrium is too long and the plasma density too low for LTE conditions.

The ExoCross calculation is repeated for rotational and vibrational temperatures varying independently from 500 K to 10000 K.

3.5.1 BeH Analysis

Figures 3.18 and 3.19 compare experimental BeH spectra with the theoretical spectra generated by the computational methods described in section 2.3. An invasive H-atom line, H_β, is marked in Figure 3.18; this region was excluded from the temperature fitting procedure in diffspec as described above. The best fit temperature for this spectra has $T_{\rm rot} = (540 \pm 70)$ K and $T_{\rm vib} = (3300 \pm 300)$ K meaning that the emission is from a non– LTE plasma. The fitting metric for this combination of rotational and vibrational temperatures = 0.208. Uncertainties were obtained from the greatest variation in temperature within 10% increase of the metric. The extreme difference between the vibrational and rotational temperatures is a product of the method by which the spectrum was produced. The need for a much higher vibrational temperature is illustrated by the presence of the 1 – 1 vibrational band head around 20050 cm^{-1} in Figure 3.18 which is absent for $T_{\rm vib}$ = $T_{\rm rot}$ = 540 K. This would be the spectrum of BeH in LTE at 540 K and it clearly shows all of the primary peaks, that is all the transitions from fundamental vibrational quanta $v' = 0$

to $v'' = 0$. What is missing are all the lower intensity peaks which are produced by transitions from higher vibrational states. When the vibrational temperature is brought up to the best fit temperature of 3300 K the lower intensity, higher vibrational, components of the spectrum are brought sharply into alignment with the experimentally observed spectrum.

The degree of matching to the experimental spectra is highlighted by the close–up view of the R-branch shown in Figure 3.19. The transition assignment labels here show how the vibrational quanta $v' = 0$ – $v'' = 0$ transitions are more intense and those of higher vibrational quanta are lower in intensity. The assignments show in order left to right: v' = upper state vibrational quantum number, N' = upper state nuclear rotational quantum number, v'' = lower state vibrational quantum number, N'' = lower state nuclear rotational quantum number. The heights of the transition lines in this figure are proportional to the A-values of the transitions not to the transition intensities. Hence, these lines do not necessarily correspond one to one to the height of the peaks in the synthetic spectrum which are dependent on temperature based populations, see equation (2.3.1), as well as A-values.

3.5.2 BeD Analysis

A match was made between the experimental BeD spectrum from JET and a theoretical spectrum by varying the vibrational and rotational temperatures. Figure 3.21 shows an assigned synthetic spectrum generated at $T_{\text{rot}} = (3800 \pm 700)$ K and $T_{\text{vib}} = (4700 \pm 800)$ K using our BeD line list. The fitting metric for this combination of rotational and vibrational temperatures = 0.254. Uncertainties were obtained from the greatest variation in temperature within 10% increase of the metric. This combination of experimental BeD spectra has also been fitted assuming LTE ($T_{\text{rot}} = T_{\text{vib}}$). This gave a result of $T_{\text{rot}} = T_{\text{vib}} = (4300 \pm 600)$ K with the fitting metric = 0.274. This temperature fitting was also repeated while excluding the vibrational 0 – 0 band head for both non– LTE and LTE assumptions. This gave a result of $T_{\text{rot}} = (4100 \pm 700)$ K and $T_{\text{vib}} = (4700 \pm 800)$ K for non–LTE with the fitting metric = 0.236 and $T_{\text{rot}} = T_{\text{vib}} = (4400 \pm 600)$ K for LTE with the fitting metric = 0.252.

The vibrational and rotational temperatures fitted to the joined spectrum for BeD are much closer than in the BeH spectrum above, meaning that, after allowing for uncertainties, the plasma conditions were in fact consistent with LTE conditions. There are four features, around ≈ 20000 cm^{-1} in the JET spectra which are not reproduced in the synthetic spectrum. These are invasive features from other species, two being impurity lines of remaining nitrogen in the plasma.

Figure 3.22 shows a close up section of the Q–branch with black drop lines at every transition energy in the region. This figure demonstrates the high degree of accuracy present across the range of these calculations.

Duxbury et al. (1998) showed fits for several molecular features in JET spectra including a BeD spectrum of the A to X transition. They fit a synthetic spectrum to an observed spectrum, which is generated using molecular constants. These constants are only valid for each isotopologue individually. By visual comparison, our work shows an improvement in both line positions and intensities.

3.5.3 BeT Predictions

Figure 3.23 shows a predicted synthetic spectrum of the A – X transition of BeT. The rotational and vibrational temperatures used to generate this spectrum are those found for BeD in the JET discharges discussed before. This is the BeT rovibronic spectrum expected to be observed in JET during a pure tritium campaign in discharges similar to those in which the BeD spectra were observed. The degree of accuracy in the results for BeT, and any isotopologue of BeH, is expected to be as seen in Figure 3.19 for BeD. This will be compared with future JET and ITER spectra with their D/T fuel mix.

[h]

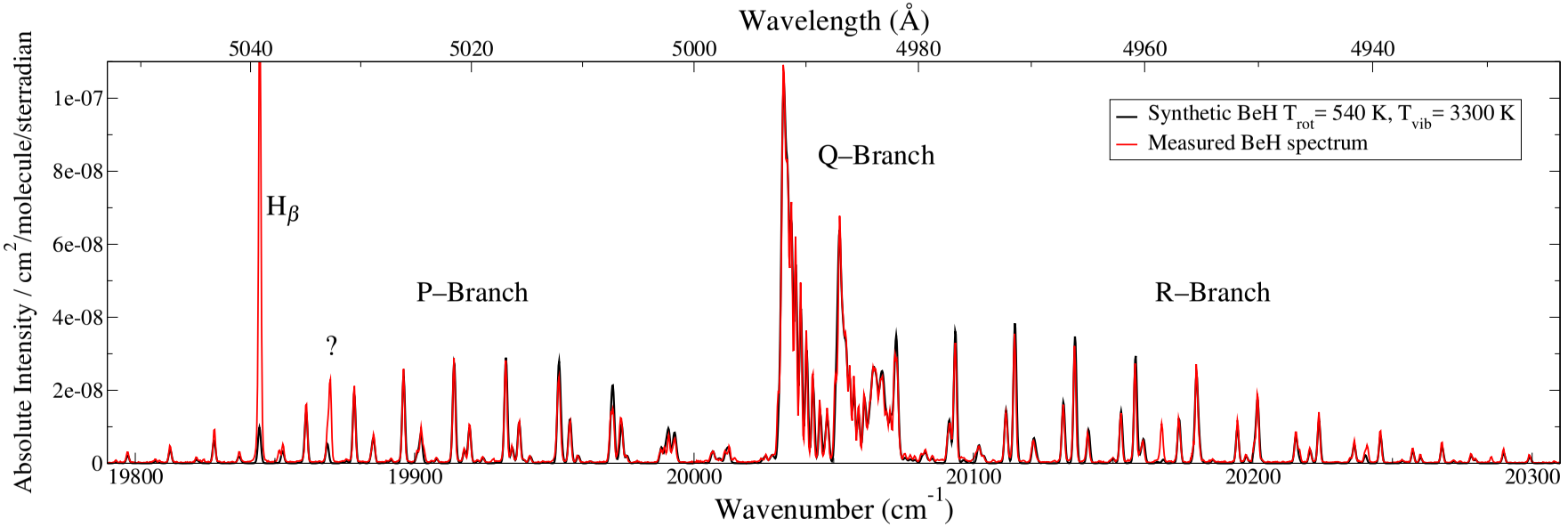

Figure 3.18: Measured BeH spectrum, shown in red, was recorded with a high resolution visible spectrometer from a hydrogen doped lamp with a beryllium target. Assigned synthetic spectrum of BeH, in black, is generated with T_{rot} = 540 K and T_{vib} = 3300 K using our BeH line list. H_β marks an invasive hydrogen line and "?" marks an unidentified invasive line.

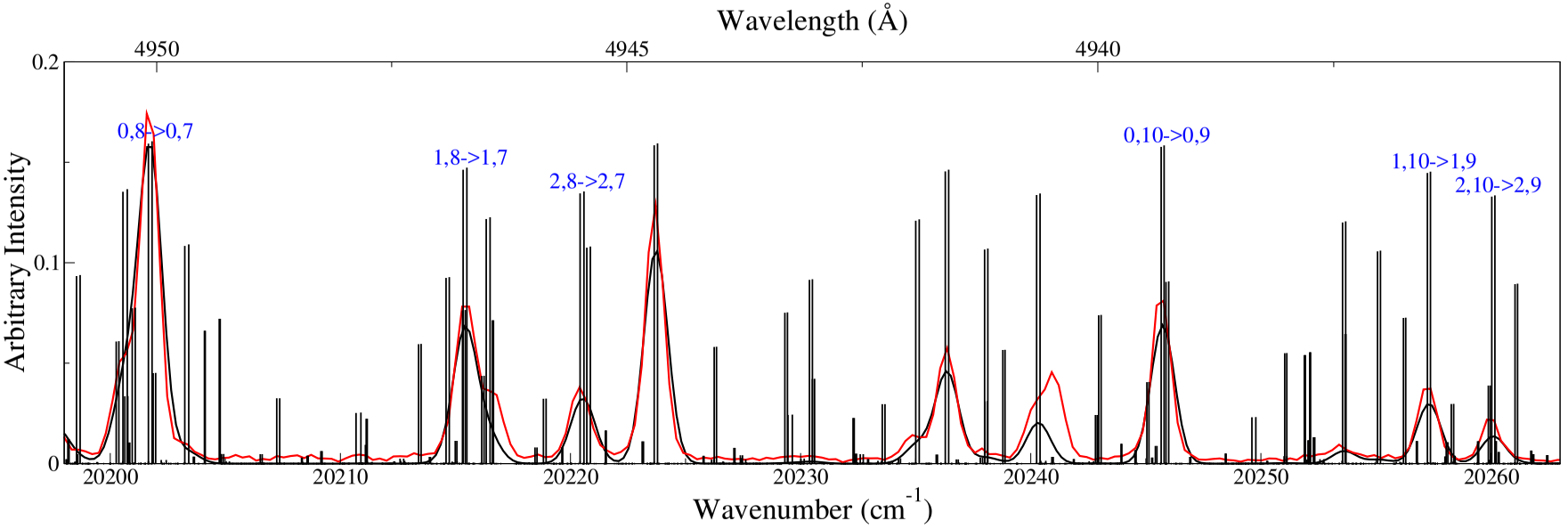

Figure 3.19: Magnified R-branch synthetic BeH A – X spectrum as in Figure 3.18, generated at T_{rot} = 540 K and T_{vib} = 3300 K. Measured BeH spectrum is shown in red and transition assignments with drop lines in black. Assignments show the upper state vibrational quantum number, upper state nuclear rotational quantum number –> lower state vibrational quantum number, lower state nuclear rotational quantum number.

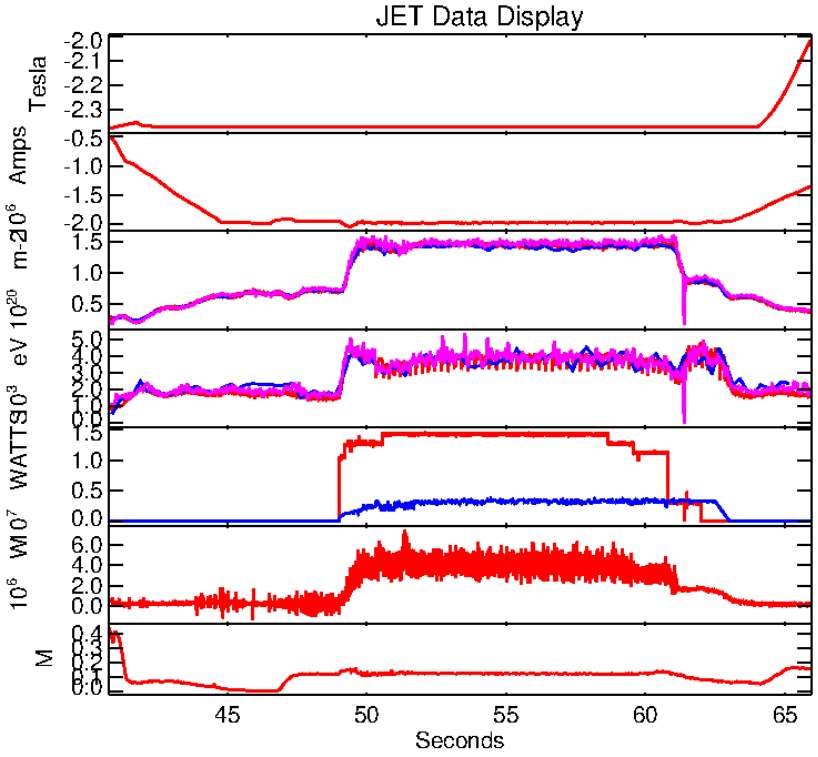

(a) Graphs showing various plasma discharge recordings during pulse number 92488. From top down, they show: toroidal magnetic field in Tesla; the plasma current in 10^6 Amps; the line integrated electron density measured by the interferometer (red), LIDAR (blue) and the high resolution Thompson scattering diagnostic (magenta) in 10^{20} m^2 which all agree; the maximum electron temperature measured by ECE (red), LIDAR (blue) and high resolution Thompson scattering (magenta) in 10^3 eV which all agree; additional heating power, NBI (red) and ICRH (blue) in 10^7 watts; the power radiated from the bulk plasma in 10^6 watts; finally plasma - inner wall gap (at a position major radius, R=1.8866, and height above the midplane, z=0.8693) in meters.

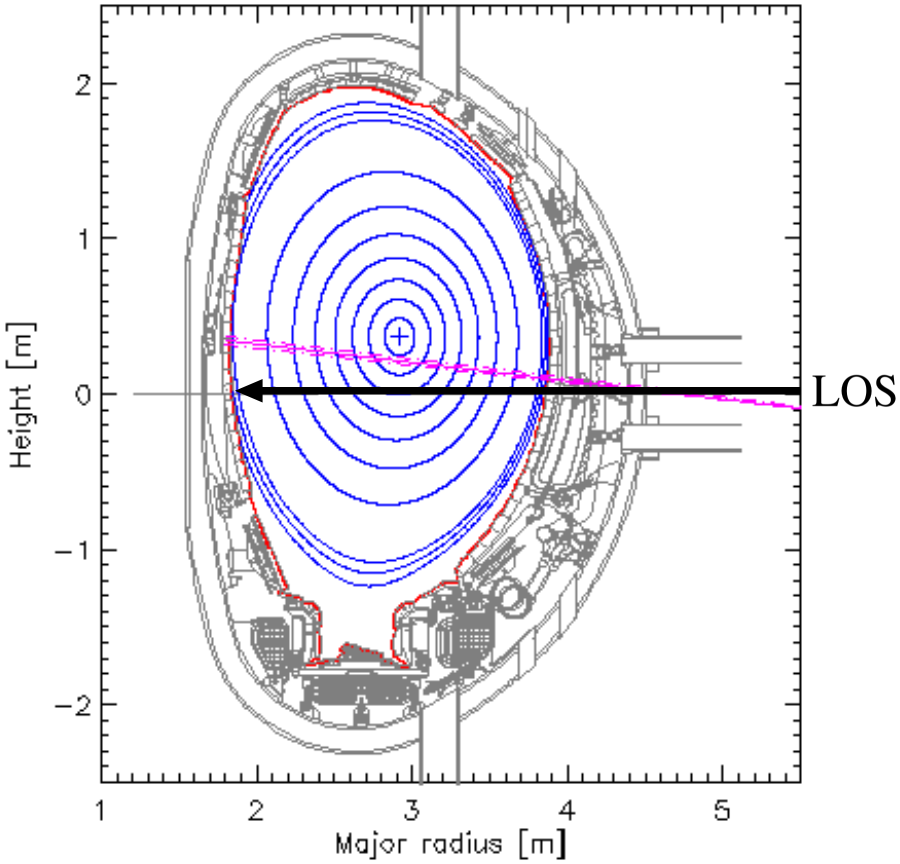

(b) Diagram showing magnetic field lines (blue) and line of sight of the spectrometer (black arrow) in the JET reactor at the time of recording the BeD spectra. Pulse number 92488 at time 45.300800 s.

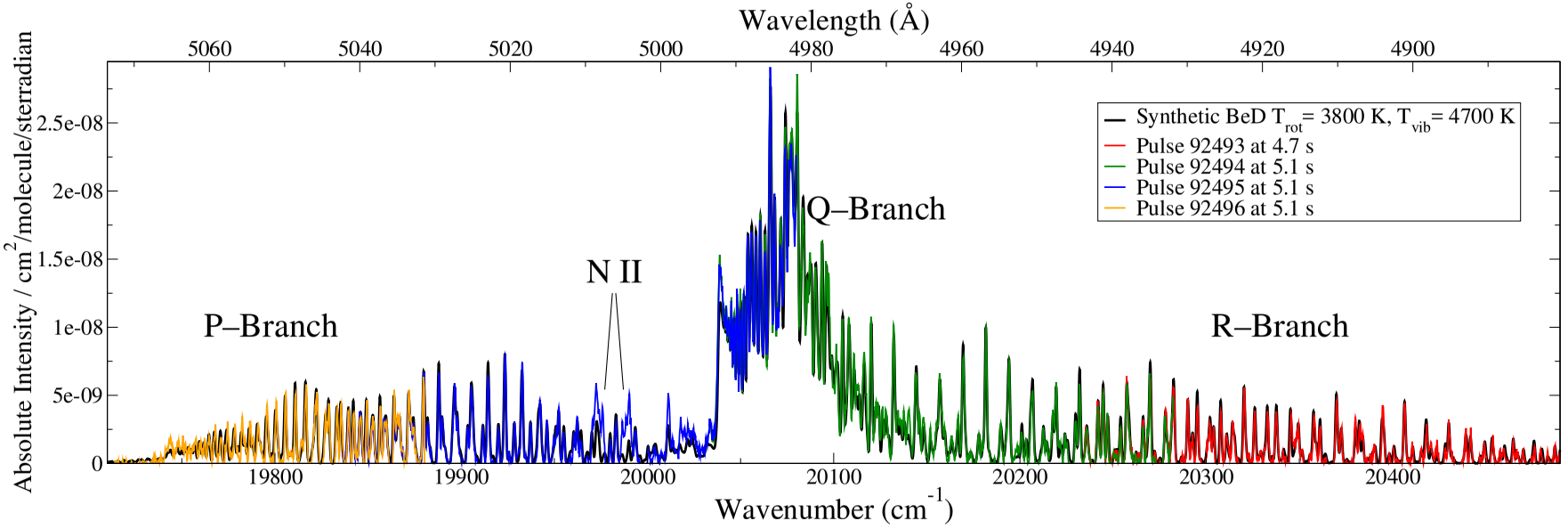

Figure 3.21: Measured BeD spectra, in red, green, blue and orange lines with pulse numbers and times in the legend, were recorded with a high resolution spectrometer, $T_e \approx 30$ eV and $n_e \approx 10^{-18}$ m^{-3}. Assigned synthetic spectrum, in black, is generated with T_{rot} = 3800 K and T_{vib} = 4700 K using our BeD line list.

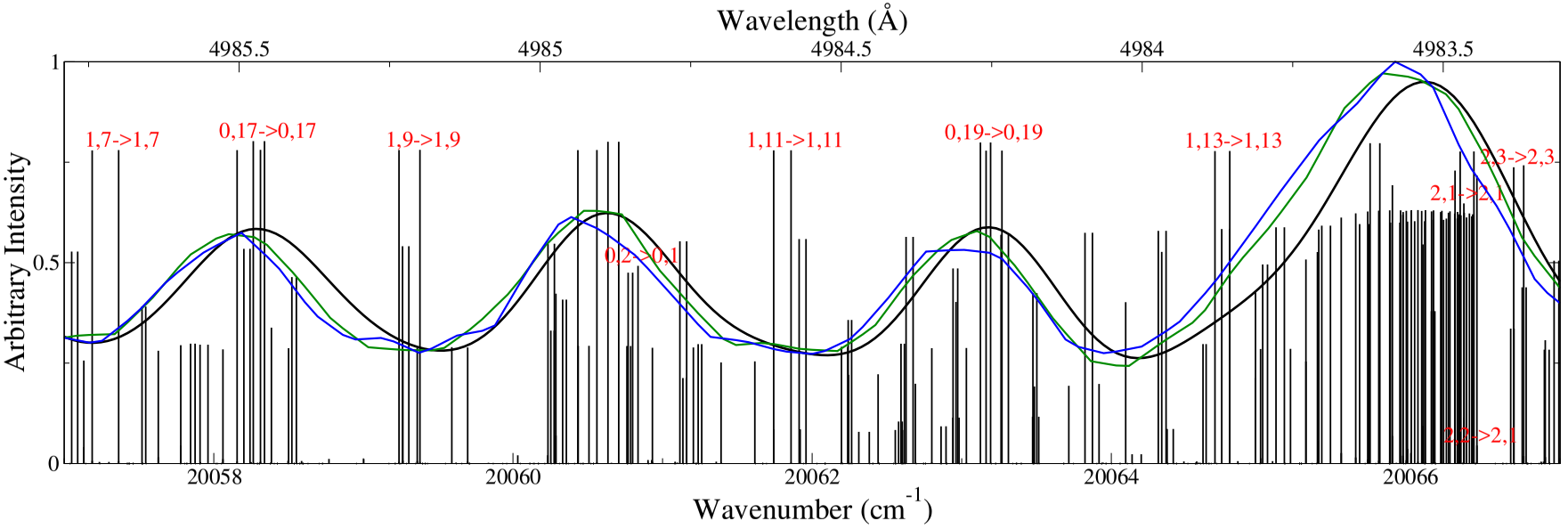

Figure 3.22: Magnified Q-Branch synthetic BeD A – X spectra as in Figure 3.21, generated at T_{rot} = 3800 K and Transition assignments with drop lines in black and high resolution JET measured spectra in green and blue. Assignments show in order left to right: v'' = upper vibrational quantum number, N'' = upper nuclear rotational quantum number, v' = lower vibrational quantum number, N' = lower nuclear rotational quantum number.

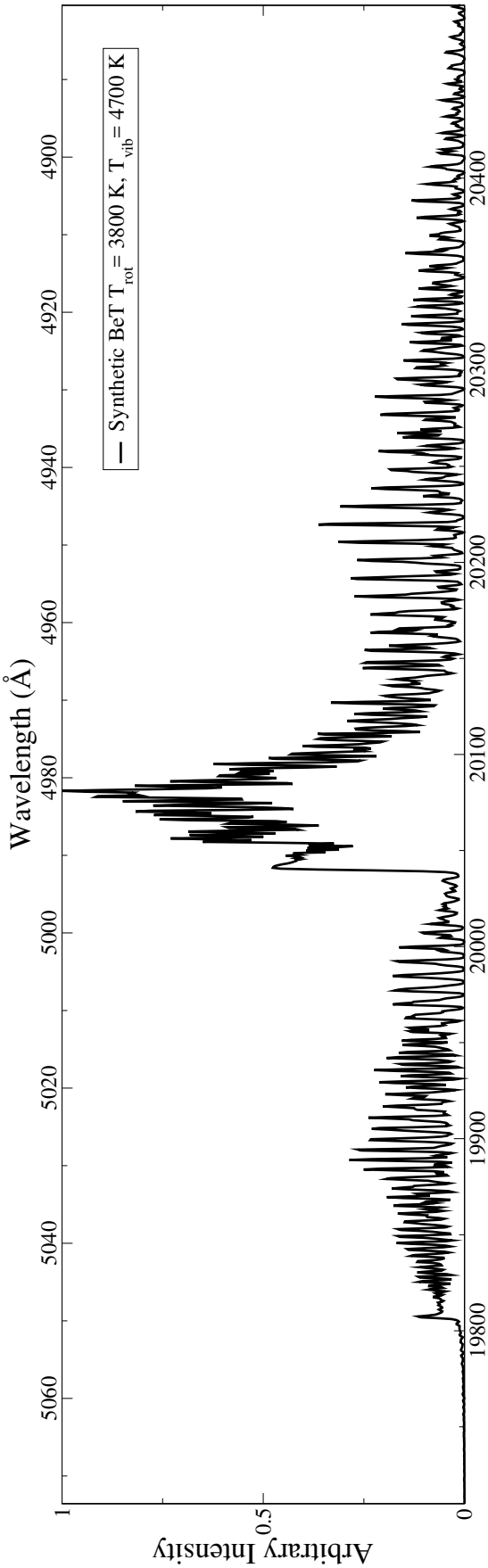

Figure 3.23: Predicted synthetic spectrum of BeT A – X calculated at T_{rot} = 3800 K and T_{vib} = 4700 K.

3.6 Other Molecules

This section briefly discusses the results from the auxiliary parts of this project performed either as outreach or in which I played an assisting role.

3.6.1 R-matrix electron collision calculations with He_2^+

The first work to mention in brief is that performed by Michel Epée Epée during his time at UCL, visiting from the University of Douala in Cameroon. While he was at UCL I assisted Michel in the use of the UKRMol suite of R-matrix codes to obtain results for electron scattering with He_2^+.

The aim of these calculations was an investigation of the resonant and bound states of He_2 and these findings were subsequently published (Epée Epée et al. 2017). The result of these calculations show an improvement over the previous work in the area by Royal and Orel (2005). These results will be used as input for dissociate recombination calculations.

3.6.2 MARVEL analysis of ^{14}NH

This work, now published, was carried out mostly as part of an outreach program called ORBYTS (Sousa-Silva et al. 2018) which is linked to the upcoming TWINKLE satellite mission (Tessenyi et al. 2015). This program is utilised at secondary schools in which a PhD student takes the role of tutor and along with a team of junior scientists from among the scientifically gifted students at the school embark on a research project.

Here I was the tutor, the school was Preston Manor High School and the five students are all named authors on the paper labelled as submitted to the Journal of Molecular Spectroscopy on the publications list (page 3) at the beginning of this thesis; student authors are from the second to sixth authors listed. The project was to conduct a literature survey of the experimental transition data for the molecule ^{14}NH, to extract this data and uniformly format it into a spreadsheet and finally to run this data through the MARVEL program.

There was a significant quantity of data for this molecule and the students did a good job extracting most of it from the literature. After the student side of

the program there was still a significant amount of work necessary to make a final collation of all the data gathered, in which the main work was done by myself and my supervisor, Jonathan Tennyson. There was also additional data provided by collaborators on the paper, Peter Bernath and Roland Tóbiás, and also contributions from the authors of the MARVEL code, Tibor Furtenbacher and Atilla G. Császár.

Chapter 4

Conclusions

4.1 R-Matrix Electron Collision Calculations

I have performed R-matrix calculations of elastic and inelastic electron collisions with BeH using scattering models ranging from static-exchange to full configuration interaction. This work is the first application of the new set of UKRMol+ R-matrix codes which use a mixed B-spline/Gaussian basis for the continuum. The new suite has allowed us to use a large R-matrix radius of 35 Bohr without compromising the quality of the continuum description thus enabling the use of a diffuse atomic basis to represent accurately electronic states of the target molecule. The vertical excitation energies and the properties of the low-lying electronic states (up to 6.5 eV) are in excellent agreement with experiment and high-level electronic structure calculations. A careful comparison of the scattering results obtained with the new UKRMol+ and the old UKRMol codes has been done to verify the validity and accuracy of the new code.

Full configuration interaction models have been used to calculate elastic and electron impact electronic excitation cross sections using more accurate models than in the previous studies. This includes a correct treatment of the Born correction for the inelastic cross section. We demonstrate the importance of the Born correction for this system and in particular for the cross section for electron impact excitation of the lowest-lying excited state A $^2\Pi$. It is radiative emissions from this state that have been observed in fusion plasmas and we find that this cross section was

significantly underestimated in the only previous R-matrix study. I also found and characterised several electron resonances which appear below 8 eV and enhance both the elastic and inelastic cross sections.

4.1.1 Multi–Geometry Calculations and Vibrational Averaging

These R-matrix calculations have been completed over a range of geometries and the resultant calculations have given a very robust test of the new UKRMol+ suite of codes including the MPI implementation of scatci (Al-Refaie and Tennyson 2017). This involved thousands of hours in wall clock time to compute and approximately 30,000 hours of CPU time to complete. The multi geometry results show smoothly varying cross–sections with geometry, see figure 3.8, attesting to the reliability of these calculations.

Though the multi-geometry data is of interest by itself, and has been requested by colleagues working on scattering problems involving BeH^-, to us it is mostly of interest in forming the vibrationally resolved results.

The vibronic results from this work have given some interesting, and even surprising results. Initially the quasi–FCF results are not unexpected, just providing cross-sections varying with the FCFs. The novel part of the quasi–FCF model is the application of Born corrections, which, considering the significant values of the vibrational dipoles, makes a significant impact. The surprising results really come form the full multi–geometry vibrationally averaged model in which it can be seen that the largest vibronic components of the cross-sections are not as the FCFs predicted to be the $\Delta v = 0$ components but rather seem to be the $\Delta v = 1$ components in many cases as seen in figure 3.12.

4.2 Spectra Modelling

I have constructed line lists for the species BeH, BeD and BeT by using a mixture of fits to empirical energy levels to obtain PECs, coupling terms and BOB corrections. It was concluded from a comparison of a synthetic spectrum fitted to experimental BeH and BeD spectra that our line lists reproduce the spectra of BeH, BeD and BeT to good accuracy. This accuracy is shown in Figures 3.19 and 3.22 and is assured

for BeT by the isotopologue consistency of our model. The comparisons show discrepancies in the intensities, for example, in the case of the BeD spectrum mostly seen in the Q-branch $v = 0 - 0$ band head. In the synthetic spectrum, the rotational temperature is too high to match this band head, which increases in relative intensity with decreasing rotational temperature.

There are two possible explanations for this issue: firstly the theoretical model uses a statistical population model, which assumes a thermal equilibrium; the second possibility is that the line of sight for the experimental spectrum passes through different temperature regions, all radiating and giving a cumulative result. The first of these issues will be addressed in a future publication (Darby-Lewis et al. 2019) by introducing a full collisional–radiative population model utilising vibrationally averaged R-Matrix results from the calculations of Darby-Lewis et al. (2017) extended over bond lengths. The issue with the line of sight can be solved with a line of sight integration calculation applied to the results of the full population model. A possible third explanation is self absorption but given the very thin (less than 1 cm) layer of plasma containing BeD in the limiter region observed this is not thought to be able to significantly contribute to the effect seen on the $0 - 0$ vibrational band head. This assumption will be tested in future work when we include a full collisional–radiative population model.

Finally in a comparison with the previous work on BeD spectra modelling at JET by Duxbury et al. (1998) we conclude that a more accurate and more comprehensive model has been achieved for two reasons. Firstly, the accuracy of the transition frequency fitting is much increased in our work. Secondly, our model is built using a single dataset derived from all the experimental transition data to model the three isotopologues. Not only does this improve the accuracy of the model, but it also enables accurate predictions to be made for the sparsely observed BeT isotopologue.

This work is an important step forward in providing high accuracy theoretical data necessary in fusion applications, especially that required by modellers at JET. Further work will focus on scattering calculations for a range of bond lengths which

will be used to produce vibrationally-resolved excitation cross sections.

4.3 Future Work

Most of the future work resulting from this project is expected to be computational, involving the programs developed and data calculated. The data provided will be used in a future publication to build an electron collisional radiative model (see below). The code for vibrational averaging is available from the UK-AMOR repository (UKA) and can be used as a method for obtaining vibronic electron collisional data in conjunction with the UKRMol/UKRMol+ suites.

However there is also a portion of work planned being carried at JET with the start of a new campaign which is experimental. The observation of BeD_2 is planned using a small survey spectrometer, through a quartz port window and a UV optimised fibre. This new spectrometer is now in place and has begun recording data. Preliminary calculations were done predicting the position of the GS to first excited state transition spectrum and the observational region in the UV was planned based on these predictions. What is still needed here is a spectral model of BeD_2, and its isotopologue, in the UV as this is still unknown.

4.3.1 Electron Collisional Radiative Model

The most important follow up to the work presented in this thesis is the final application of the multi-geometry vibrationally averaged R-matrix cross–sections to a full electron collisional radiative model. This work is planned for a future publication which will include: (1) the multi-geometry R-matrix results; (2) the vibronically resolved R-matrix results with (2.a) the vibrationally averaged R-matrix results in comparison to (2.b) the quasi–FCF single geometry results; (3) the transition rates as calculated from the convolution of the cross-sections with a Maxwell–Boltzmann distribution of electron energies as a function of electron temperature; (4) the combination of these rates with the Einstein A-value rates from the spectral modelling phase of this work into a total radiative collisional model; (5) the comparison of the spectral predictions of these calculation in contrast to the previous theoretical spectra produced using vibrational and rotational temperature fitting.

Most of the work planned for this future publication is already completed and what remains is the calculation of rates, the production of a collisional radiative model and the generation and fitting of theoretical to experimental spectra. This final phase represents the combination of the two main branches of work in this project, the vibrationally averaged R-matrix calculations feeding into a spectral model through collisional radiative modelling providing, hopefully, better synthetic spectra fittings with more useful information to JET plasma modellers.

Bibliography

UKAMOR. https://gitlab.com/Uk-amor.

A. F. Al-Refaie and J. Tennyson. A parallel algorithm for Hamiltonian matrix construction in electron-molecule collision calculations: MPI-SCATCI. *Computer Phys. Comm.*, 214:216–224, 2017. doi: 10.1016/j.cpc.2017.07.023.

P. Atkins and R. Friedman. *Molecular Quantum Mechanics*. Oxford University Press, 4th edition, 2011.

H. Bachau, E. Cormier, P. Decleva, J. E. Hansen, and F. Martin. Applications of b-splines in atomic and molecular physics. *Rep. Prog. Phys.*, 64:1815–1943, 2001.

P. F. Bernath. *Spectra of Atoms and Molecules*. Oxford University Press, 2nd edition, 2005.

M. Bessenrodt-Weberpals, J. Hackmann, and J. Uhlenbusch. Beryllium release and beryllium transport in the tokamak unitor. *J. Nucl. Materials*, 145:849–853, 1987.

C. Björkas, D. Borodin, A. Kirschner, R. Janev, D. Nishijima, R. Doerner, and K. Nordlund. Multiscale modeling of bed release and transport in pisces-b. *Journal of Nuclear Materials*, 438:S276–S279, 2013.

F. Bloch. Nuclear induction. *Physical review*, 70(7-8):460, 1946.

M. Born and R. Oppenheimer. Zur quantentheorie der molekeln. *Annalen der physik*, 389(20):457–484, 1927.

D. Borodin, A. Kirschner, S. Carpentier-Chouchana, R. Pitts, S. Lisgo, C. Björkas, P. Stangeby, J. Elder, A. Galonska, D. Matveev, et al. Ero code benchmarking

of iter first wall beryllium erosion/re-deposition against lim predictions. *Physica scripta*, 2011(T145):014008, 2011.

G. Breit and E. Wigner. Capture of slow neutrons. *Physical review*, 49(7):519, 1936.

S. Brezinsek, A. Pospieszczyk, G. Sergienko, P. Mertens, and U. Samm. Use of a high-resolution overview spectrometer for the visible range in the textor boundary plasma. *Plasma and Fusion Research*, 3:S1041–S1041, 2008.

S. Brezinsek, M. F. Stamp, D. Nishijima, D. Borodin, S. Devaux, K. Krieger, S. Marsen, M. O'Mullane, C. Bjoerkas, and A. a. Kirschner. Study of physical and chemical assisted physical sputtering of beryllium in the JET ITER-like wall. *Nuclear fusion*, 54:103001, 2014.

S. Brezinsek, A. Widdowson, M. Mayer, V. Philipps, P. Baron-Wiechec, J. W. Coenen, K. Heinola, A. Huber, J. Likonen, P. Petersson, M. Rubel, M. F. Stamp, D. Borodin, J. P. Coad, A. G. Carrasco, A. Kirschner, S. Krat, K. Krieger, B. Lipschultz, C. Linsmeier, G. F. Matthews, K. Schmid, and J. Contributors. Beryllium migration in JET ITER-like wall plasmas. *Nuc. Fusion*, 55:063021, 2015. doi: {10.1088/0029-5515/55/6/063021}.

P. G. Burke. *R-Matrix Theory of Atomic Collisions: Application to Atomic, Molecular and Optical Processes*. Springer, 2011.

J. M. Carr, P. G. Galiatsatos, J. D. Gorfinkiel, A. G. Harvey, M. A. Lysaght, D. Madden, Z. Mašín, M. Plummer, and J. Tennyson. The ukrmol program suite. *Eur. Phys. J. D*, 66:58, 2012.

R. Celiberto, K. L. Baluja, and R. K. Janev. Electron-impact state-to-state resolved cross sections and rate coefficients for the x (v) $\rightarrow$ a (v$'$) excitation in BeH molecules. *Plasma Sources Science and Technology*, 22:015008, 2012a.

R. Celiberto, R. Janev, and D. Reiter. State-to-state electron impact cross sec-

tions for BeH+ molecular ions in ITER-like fusion edge plasmas with Be walls. *Plasma Phys. Contr. Fusion*, 54:035012, 2012b.

K. Chakrabarti and J. Tennyson. Electron collisions with the BeH^+ molecular ion in the R-matrix approach. *Eur. Phys. J. D*, 66:31, 2012.

K. Chakrabarti and J. Tennyson. R-matrix calculation of bound and resonant states of BeH. *J. Phys. B: At. Mol. Opt. Phys.*, 48:235202, 2015. doi: 10.1088/0953-4075/48/23/235202.

R. Colin, C. Dreze, and M. Steinhauer. Rotational analysis and deperturbation of the c 2σ+–x 2σ+ band systems of beh and bed. *Can. J. Phys.*, 61:641–655, 1983.

E. Condon. A theory of intensity distribution in band systems. *Physical Review*, 28 (6):1182, 1926.

A. G. Császár and T. Furtenbacher. Spectroscopic networks. *J. Mol. Struct. (Theochem)*, 266:99 – 103, 2011. doi: 10.1016/j.jms.2011.03.031.

M. Czerny and A. F. Turner. Über den astigmatismus bei spiegelspektrometern. *Zeitschrift für Physik*, 61(11):792–797, Nov 1930. ISSN 0044-3328. doi: 10.1007/BF01340206. URL https://doi.org/10.1007/BF01340206.

G. Danby and J. Tennyson. R-matrix calculations of vibrationally resolved positron – N_2 scattering cross sections. *J. Phys. B: At. Mol. Opt. Phys.*, 24:3517–3529, 1991.

D. Darby-Lewis, Z. Masin, and J. Tennyson. R-Matrix Calculations of electron-impact electronic excitation of BeH. *J. Phys. B: At. Mol. Opt. Phys.*, 50:175201, 2017. doi: 10.1088/1361-6455/aa8161.

D. Darby-Lewis, J. Tennyson, K. D. Lawson, S. N. Yurchenko, M. F. Stamp, A. Shaw, S. Brezinsek, and JET Contributor. Synthetic spectra of BeH, BeD and BeT for emission modelling in JET plasmas. *J. Phys. B: At. Mol. Opt. Phys.*, 51:185701, 2018. doi: 10.1088/1361-6455/aad6d0.

D. Darby-Lewis, K. D. Lawson, and J. Tennyson. Vibrationally Resolving R-Matrix electron-impact calculations for BeH, BeD and BeT. *J. Phys. B: At. Mol. Opt. Phys.*, 2019.

N. S. Dattani. Beryllium monohydride (BeH): Where we are now, after 86 years of spectroscopy. *J. Mol. Spectrosc.*, 311:76–83, 2015. doi: {10.1016/j.jms.2014.09.005}.

D. De Greef and R. Colin. The electronic isotope shift in the a2π-x2σ+ bands of beh, bed and bet. *J. Mol. Struct. (Theochem)*, 53:455–465, 1974.

R. Doerner, M. Baldwin, J. Hanna, C. Linsmeier, D. Nishijima, R. Pugno, J. Roth, K. Schmid, and A. Wiltner. Interaction of beryllium containing plasma with iter materials. *Phys. Scr.*, T128:115, 2007.

R. P. Doerner, M. J. Baldwin, D. Buchenauer, G. De Temmerman, and D. Nishijima. The role of beryllium deuteride in plasma-beryllium interactions. *J. Nuc. Materials*, 390-91:681–684, 2009. doi: {10.1016/j.jnucmat.2009.01.187}.

G. Duxbury, M. F. Stamp, and H. P. Summers. Observations and modelling of diatomic molecular spectra from JET. *Plasma physics and controlled fusion*, 40: 361, 1998.

G. Duxbury, M. F. Stamp, and H. P. Summers. Observations and modelling of diatomic molecular spectra from JET. *Plasma Phys. Controlled Fusion*, 40:361–370, 1998. doi: {10.1088/0741-3335/40/3/002}.

M. D. Epée Epée, O. Motapon, D. Darby-Lewis, and J. Tennyson. Electron-He_2^+ scattering calculation using the R-matrix method: resonant and bound states of He_2. *J. Phys. B: At. Mol. Opt. Phys.*, 50:115203, 2017. doi: 10.1088/1361-6455/aa6a34.

A. Faure, J. D. Gorfinkiel, L. A. Morgan, and J. Tennyson. GTOBAS for fitting Gaussian Type Orbitals to Bessel and Coulomb functions. *Computer Phys. Comm.*, 144:224–241, 2002.

A. Faure, P. Halvick, T. Stoecklin, P. Honvault, M. D. Epée Epée, J. Z. Mezei, O. Motapon, I. F. Schneider, J. Tennyson, O. Roncero, N. Bulut, and A. Zanche. State-to-state chemistry and rotational excitation of CH^+ in photon-dominated regions. *Mon. Not. R. Astr. Soc.*, 469:612–620, 2017.

G. Federici. Plasma wall interactions in ITER. *Phys. Scr.*, T124:1, 2006. doi: {10.1088/0031-8949/2006/T124/001}.

C. Focsa, P. F. Bernath, R. Mitzner, and R. Colin. Fourier transform emission spectroscopy of thea 2 π–x 2 σ+ transition of bed. *J. Mol. Struct. (Theochem)*, 192: 348–358, 1998.

J. Franck and E. G. Dymond. Elementary processes of photochemical reactions. *Trans. Faraday Soc.*, 21:536–542, 1926. doi: 10.1039/TF9262100536. URL http://dx.doi.org/10.1039/TF9262100536.

W. Fundamenski. Chapter 6: Scrape-off layer transport on jet. *Fusion Science and Technology*, 53(4):1023–1063, 2008. doi: 10.13182/FST08-A1746. URL ttps://doi.org/10.13182/FST08-A1746.

T. Furtenbacher and A. G. Császár. MARVEL: measured active rotational-vibrational energy levels. II. Algorithmic improvements. *J. Quant. Spectrosc. Radiat. Transf.*, 113:929–935, 2012.

T. Furtenbacher, A. G. Császár, and J. Tennyson. MARVEL: measured active rotational-vibrational energy levels. *J. Mol. Struct. (Theochem)*, 245:115–125, 2007. doi: 10.1016/j.jms.2007.07.005.

M. Gailitis. *J. Phys. B: At. Mol. Opt. Phys.*, 9:843, 1976.

A. Gibson. The jet project. *Naturwissenschaften*, 66:481–488, 1979. doi: 10.1007/BF00404857.

C. J. Gillan, J. Tennyson, and P. G. Burke. The UK molecular R-matrix scattering package: a computational perspective. In W. Huo and F. A. Gianturco, editors,

Computational methods for Electron-molecule collisions, pages 239–254, New York, 1995. Plenum.

J. D. Gorfinkiel, L. A. Morgan, and J. Tennyson. Electron impact dissociative excitation of water within the adiabatic nuclei approximation. *J. Phys. B: At. Mol. Opt. Phys.*, 35:543–555, 2002.

D. Gupta, M.-Y. Song, H. Choi, D.-C. Kwon, K. L. Baluja, and J. Tennyson. R-matrix study for electron scattering of beryllium dihydride for fusion plasma. *J. Phys. B: At. Mol. Opt. Phys.*, 2019. doi: 10.1088/1361-6455/aafdc4.

A. G. Harvey, D. S. Brambila, F. Morales, and O. Smirnova. Cdenprop: Transition matrix elements involving continuum states. *arXiv preprint arXiv:1401.0229*, 2013.

J. O. Hornkohl, C. Parigger, and J. Lewis. Temperature measurements from cn spectra in a laser-induced plasma. *Journal of Quantitative Spectroscopy and Radiative Transfer*, 46(5):405 – 411, 1991. ISSN 0022-4073. doi: https://doi.org/10.1016/0022-4073(91)90042-O. URL http://www.sciencedirect.com/science/article/pii/002240739190042O.

K. P. Huber and G. Herzberg. *Molecular Spectra and Molecular Structure IV. Constants of Diatomic Molecules*. Van Nostrand Reinhold Company, New York, 1979.

Z. J. Z. Hui. *Theory and application of quantum molecular dynamics*. World Scientific, 1998.

S. Kaur, K. L. Baluja, and J. Tennyson. Electron–impact study of NeF using the R-matrix method. *Phys. Rev. A*, 77:032718, 2008.

M. Keilhacker, A. Gibson, C. Gormezano, and P. Rebut. The scientific success of jet. *Nucl. Fusion*, 41:1925, 2001.

J. Koput. The ab initio ground-state potential energy function of beryllium monohydride, BeH. *J. Chem. Phys.*, 135:244308, 2011.

I. B. Kupriyanov, G. N. Nikolaev, L. A. Kurbatova, N. P. Porezanov, V. L. Podkovyrov, A. D. Muzichenko, A. M. Zhitlukhin, A. A. Gervash, and V. M. Safronov. Erosion of beryllium under ITER - Relevant transient plasma loads. *J. Nuc. Materials*, 463:781–786, 2015. doi: {10.1016/j.jnucmat.2015.01.050}.

V. Laporta, K. Chakrabarti, R. Celiberto, R. K. Janev, J. Z. Mezei, S. Niyonzima, J. Tennyson, and I. Schneider. Theoretical resonant electron-impact vibrational excitation, dissociative recombination and dissociative excitation cross sections of ro-vibrationally excited excited BeH^+ ion. *Plasma Sources Sci. Technol.*, 59: 045008, 2017. doi: 10.1088/1361-6587/aa5c56.

A. Lasa, D. Borodin, J. M. Canik, C. C. Klepper, M. Groth, A. Kirschner, M. Airila, I. Borodkina, and R. Ding. Ero modeling and sensitivity analysis of locally enhanced beryllium erosion by magnetically connected antennas. *Nuclear Fusion*, 2017.

R. J. Le Roy. Level: A computer program for solving the radial schrödinger equation for bound and quasibound levels. *J. Quant. Spectrosc. Radiat. Transf.*, 186: 167 – 178, 2017. doi: 10.1016/j.jqsrt.2016.05.028.

R. J. Le Roy, D. R. T. Appadoo, R. Colin, and P. F. Bernath. On the x 2 σ+, a 2 π, and c 2 σ+ states of beh, bed, and bet. *J. Mol. Struct. (Theochem)*, 236:178–188, 2006.

R. J. Le Roy, C. C. Haugen, J. Tao, and H. Li. Long-range damping functions improve the short-range behaviour of 'mlr'potential energy functions. *Molecular Physics*, 109:435–446, 2011.

E. G. Lee, J. Y. Seto, T. Hirao, P. F. Bernath, and R. J. Le Roy. Ftir emission spectra, molecular constants, and potential curve of ground state geo. *Journal of molecular spectroscopy*, 194(2):197–202, 1999.

J. Lister. *Fusion: The Energy of the Universe*. IOP Publishing, 2006.

D. A. Little and J. Tennyson. Singlet and triplet *ab initio* Rydberg states of N_2. *J. Phys. B: At. Mol. Opt. Phys.*, 46:145102, 2013.

D. A. Little and J. Tennyson. An R-matrix study of singlet and triplet continuum states of N_2. *J. Phys. B: At. Mol. Opt. Phys.*, 47:105204, 2014.

Z. Mašín and J. D. Gorfinkiel. Elastic and inelastic low-energy electron collisions with pyrazine. *The Journal of Chemical Physics*, 135(14):144308, 2011. doi: 10.1063/1.3650236.

S. McGuire, A. Tibère-Inglesse, and C. Laux. Infrared spectroscopic measurements of carbon monoxide within a high temperature ablative boundary layer. *Journal of Physics D: Applied Physics*, 49(48):485502, 2016.

L. A. Morgan, C. J. Gillan, J. Tennyson, and X. Chen. R-matrix calculations for polyatomic molecules: electron scattering by N_2O. *J. Phys. B: At. Mol. Opt. Phys.*, 30:4087–4096, 1997.

L. A. Morgan, J. Tennyson, and C. J. Gillan. The UK molecular R-matrix codes. *Computer Phys. Comm.*, 114:120–128, 1998.

D. Nishijima, R. P. Doerner, M. J. Baldwin, G. De Temmerman, and E. M. Hollmann. Properties of BeD molecules in edge plasma relevant conditions. *Plasma Phys. Controlled Fusion*, 50:125007, 2008. doi: {10.1088/0741-3335/50/12/125007}.

S. Niyonzima, S. Ilie, N. Pop, J. Z. Mezei, K. Chakrabarti, V. Morel, B. Peres, D. Little, K. Hassouni, A. Larson, A. Orel, D. Benredjem, A. Bultel, J. Tennyson, D. Reiter, and I. F. Schneider. Low-energy collisions between electrons and beh^+: cross sections and rate coefficients for all the vibrational states of the ion. *At. Data Nucl. Data Tables*, 115–116:287 – 308, 2017. doi: 10.1016/j.adt.2016.09.002.

S. Niyonzima, N. Pop, F. Iacob, Å. Larson, A. E. Orel, J. Z. Mezei, K. Chakrabarti, V. K. Hassouni, D. Benredjem, A. Bultel, J. Tennyson, D. Reiter, and I. F. Schnei-

der. Low-energy collisions between electrons and BeD^+. *Plasma Sources Sci. Technol.*, 27:025015, 2018. doi: 10.1088/1361-6595/aaabef.

C. J. Noble and R. K. Nesbet. Cfasym, a program for the calculation of the asymptotic solutions of the coupled equations of electron collision-theory. *Computer Phys. Comm.*, 33:399, 1984.

D. W. Norcross and N. T. Padial. The multipole-extracted adiabatic-nuclei approximation for electron-molecule collisions. *Phys. Rev. A*, 25:226–338, 1982.

C. G. Parigger, A. C. Woods, D. M. Surmick, G. Gautam, M. J. Witte, and J. O. Hornkohl. Computation of diatomic molecular spectra for selected transitions of aluminum monoxide, cyanide, diatomic carbon, and titanium monoxide. *Spectrochimica Acta Part B: Atomic Spectroscopy*, 107:132–138, 2015.

J. Pitarch-Ruiz, J. Sánchez-Marin, and A. M. Velasco. Full configuration interaction calculation of the low lying valence and rydberg states of beh. *J. Comput. Chem.*, 29:523–532, 2007. doi: 10.1002/jcc.20811.

J. Pitarch-Ruiz, J. Sanchez-Marin, A. M. Velasco, and I. Martin. Full configuration interaction calculation of beh adiabatic states. *J. Chem. Phys.*, 129:054310, 2008. doi: 10.1063/1.2953584.

I. Rabadán and J. Tennyson. An *ab initio* calculation of the electron impact vibrational excitation of NO^+. *J. Phys. B: At. Mol. Opt. Phys.*, 32:4753–4762, 1999.

I. Rabadán, B. K. Sarpal, and J. Tennyson. Calculated rotational and vibrational excitation rates for electron – HeH^+ collisions. *Mon. Not. R. Astr. Soc.*, 299: 171–175, 1998.

J. B. Roos, M. Larsson, A. Larson, and A. E. Orel. Dissociative recombination of BeH+. *Phys. Rev. A*, 80:012501, 2009. doi: {10.1103/PhysRevA.80.012501}.

R. J. L. Roy and R. D. Henderson. A new potential function form incorporating extended long-range behaviour: application to ground-state ca2. *Molecular Physics*, 105(5-7):663–677, 2007.

J. Royal and A. E. Orel. Dissociative recombination of He_2^+. *Phys. Rev. A*, 72:022719, Aug 2005. doi: 10.1103/PhysRevA.72.022719. URL https://link.aps.org/doi/10.1103/PhysRevA.72.022719.

U. Samm. Plasma—wall interaction: Status and data needs. In *Nuclear Fusion Research*, pages 3–28. Springer, 2005.

I. Sanchez and F. Martin. Representation of the electronic continuum of with b-spline basis. *J. Phys. B: At. Mol. Opt. Phys.*, 30:679–692, 1997.

N. Sanna and F. A. Gianturco. Differential cross sections for electron/positron scattering for polyatomic molecules. *Computer Phys. Comm.*, 114:142–167, 1998.

G. Schaftenaar and J. H. Noordik. *Molden: a pre- and post-processing program for molecular and electronic structures*, 2000.

U. Schumacher. Jet, the european nuclear fusion experiment. *Atw. Atomwirtschaft, Atomtechnik*, 28:500–504, 1983.

A. Shayesteh, K. Tereszchuk, P. F. Bernath, and R. Colin. Infrared emission spectra of beh and bed. *J. Chem. Phys.*, 118:1158–1161, 2003. doi: 10.1063/1.1528606.

J. C. Slater. Atomic shielding constants. *Physical Review*, 36(1):57, 1930.

C. Sousa-Silva, L. K. McKemmish, K. L. Chubb, J. Baker, E. J. Barton, M. N. Gorman, T. Rivlin, and J. Tennyson. Original Research By Young Twinkle Students (ORBYTS): When can students start performing original research? *Phys. Educ.*, 53:015020, 2018. doi: 10.1088/1361-6552/aa8f2a.

V. Špirko. Morphing ab initio potential energy curve of beryllium monohydride. *Journal of Molecular Spectroscopy*, 330:89–95, 2016.

D. T. Stibbe and J. Tennyson. Ab initio calculations of vibrationally resolved resonances in electron collisions with H_2, HD and D_2. *Phys. Rev. Lett.*, 79:4116–4119, 1997.

F. H. Stillinger and D. R. Herrick. Bound states in the continuum. *Phys. Rev. A*, 11: 446–454, 1975. doi: 10.1103/PhysRevA.11.446.

H. Summers and M. O'Mullane. Atomic data and modelling for fusion: the adas project. In *AIP Conference Proceedings*, volume 1344, pages 179–187. AIP, 2011.

A. Šurkus, R. Rakauskas, and A. Bolotin. The generalized potential energy function for diatomic molecules. *Chemical physics letters*, 105(3):291–294, 1984.

A. Szabo and N. S. Ostlund. *Modern quantum chemistry: introduction to advanced electronic structure theory*. Courier Corporation, 2012.

M. Tarana and J. Tennyson. Polarisation effects in electron collisions with Li_2: application of the molecular R-matrix with pseudostates method. *J. Phys. B: At. Mol. Opt. Phys.*, 41:205204, 2008.

M. Tarana, B. M. Nestmann, and J. Horáček. *r*. *Physical Review A*, 79:012716, Jan 2009. doi: 10.1103/PhysRevA.79.012716.

D. Teillet-Billy, D. T. Stibbe, J. Tennyson, and J. P. Gauyacq. Vibrational excitation in low energy electron scattering by H_2 molecules physisorbed on a metal surface. *Surface Science*, 443:57–68, 1999.

J. Tennyson. A new algorithm for Hamiltonian matrix construction in electron-molecule collision calculations. *J. Phys. B: At. Mol. Opt. Phys.*, 29:1817–1828, 1996.

J. Tennyson. Electron - molecule collision calculations using the R-matrix method. *Phys. Rep.*, 491:29–76, 2010.

J. Tennyson and C. J. Noble. RESON: for the automatic detection and fitting of breit-wigner resonances. *Computer Phys. Comm.*, 33:421–424, 1984.

J. Tennyson and S. N. Yurchenko. ExoMol: molecular line lists for exoplanet and other atmospheres. *Mon. Not. R. Astr. Soc.*, 425:21–33, 2012. doi: 10.1111/j.1365-2966.2012.21440.x.

J. Tennyson, C. Hill, and S. N. Yurchenko. Data structures for ExoMol: Molecular line lists for exoplanet and other atmospheres. In *6^{th} international conference on atomic and molecular data and their applications ICAMDATA-2012*, volume 1545 of *AIP Conference Proceedings*, pages 186–195. AIP, New York, 2013. doi: 10.1063/1.4815853.

J. Tennyson, S. N. Yurchenko, A. F. Al-Refaie, E. J. Barton, K. L. Chubb, P. A. Coles, S. Diamantopoulou, M. N. Gorman, C. Hill, A. Z. Lam, L. Lodi, L. K. McKemmish, Y. Na, A. Owens, O. L. Polyansky, T. Rivlin, C. Sousa-Silva, D. S. Underwood, A. Yachmenev, and E. Zak. The ExoMol database: molecular line lists for exoplanet and other hot atmospheres. *J. Mol. Struct. (Theochem)*, 327: 73–94, 2016. doi: 10.1016/j.jms.2016.05.002.

M. Tessenyi, G. Tinetti, J. Tennyson, G. Savini, E. Pascale, S. Jason, D. Liddle, J. Williams, A. Vora, and C. Saunders. Twinkle – a British space mission to explore faraway worlds. In *Proceedings of the International Astronautical Congress, IAC*, volume 6, pages 4311–4313. International Astronautical Federation, 2015.

R. C. Tolman. *The principles of statistical mechanics*. Courier Corporation, 1979.

C. S. Trevisan and J. Tennyson. Calculated rates for the electron impact dissociation of molecular hydrogen: mixed isotopomers and scaling laws. *Plasma Phys. Controlled Fusion*, 44:2217–2230, 2002.

E. W. Weisstein. Spherical harmonic. 2004.

H.-J. Werner, P. J. Knowles, G. Knizia, F. R. Manby, and M. Schütz. Molpro: a general-purpose quantum chemistry program package. *WIREs Comput. Mol. Sci.*, 2:242–253, 2012. doi: 10.1002/wcms.82.

H. Winter. The present state of controlled nuclear fusion research. *Vacuum*, 25: 497–511, 1975.

B. Yadin, T. Vaness, P. Conti, C. Hill, S. N. Yurchenko, and J. Tennyson. ExoMol Molecular linelists: I The rovibrational spectrum of BeH, MgH and CaH the $X\,^2\Sigma^+$ state. *Mon. Not. R. Astr. Soc.*, 425:34–43, 2012.

F. L. Yip, C. W. McCurdy, and T. N. Rescigno. Hybrid Gaussian-discrete-variable representation for one- and two-active-electron continuum calculations in molecules. *Physical Review A*, 90(6), DEC 18 2014. ISSN 1050-2947. doi: {10.1103/PhysRevA.90.063421}.

S. N. Yurchenko, L. Lodi, J. Tennyson, and A. V. Stolyarov. Duo: a general program for calculating spectra of diatomic molecules. *Computer Phys. Comm.*, 202:262–275, 2016. doi: 10.1016/j.cpc.2015.12.021.

S. N. Yurchenko, A. F. Al-Refaie, and J. Tennyson. ExoCross: A general program for generating spectra from molecular line lists. *Astron. Astrophys.*, 614:A131, 2018. doi: 10.1051/0004-6361/201732531.

O. Zatsarinny. BSR: B-spline atomic R-matrix codes. *Computer Phys. Comm.*, 174: 273–356, 2006.

O. Zatsarinny and K. Bartschat. B-spline Breit-Pauli R-matrix calculations for electron collisions with neon atoms. *J. Phys. B: At. Mol. Opt. Phys.*, 37:2173–2189, 2004.

Zdenek Mašín. *The UKRMol+ codes*, 2017.